Magnetic Resonance Imaging of the Myocardium, Coronary Arteries, and Anomalous Origin of Coronary Arteries

13

Benjamin Y.C. Cheong and Paolo Angelini

Abstract

Over the past decade, cardiovascular magnetic resonance imaging (CMRI) has emerged as an important, non-invasive imaging modality. In certain aspects, CMRI has become the gold standard in the assessment of ischemic and nonischemic cardiomyopathy. It has relatively high spatial and temporal resolution, and it is also reproducible and does not involve ionizing radiation. Therefore, it is an ideal modality for long-term imaging follow-up. Cardiovascular magnetic resonance imaging can assess ventricular function, myocardial ischemia, and viability in a single setting. There is also a growing interest in tissue T_1 and T_2 imaging, which can be used to characterize tissues with various disease pathologies.

Although coronary multi-detector computed tomographic angiography is now widely used to assess the coronary arteries, magnetic resonance imaging coronary angiography still has an important role in the evaluation of suspected anomalous coronary artery origin, especially in the younger population.

Keywords

Myocardial viability • Myocardial ischemia • Non-ischemic cardiomyopathy • Ischemic cardiomopathy • Coronary magnetic resonance angiography

Magnetic Resonance Imaging of the Myocardium

Over the past two decades, significant progress has been made in magnetic resonance imaging (MRI). Because of advances in hardware and software, MRI has become an important diagnostic tool in everyday clinical practice. This modality is unique because it generates native, pathology-specific images that reflect the composition of tissues. Compared to other imaging modalities, MRI has important advantages: it is noninvasive, requires no ionizing radiation, relies on no geometric assumptions, and can depict any part of the human body in any plane. In addition, MRI has high spatial and temporal resolution, high contrast, and a high signal-to-noise ratio. Under certain conditions, it can detect disease even without use of a contrast agent.

Magnetic resonance imaging can be used to diagnose diseases in almost any organ. For example, MRI can evaluate anatomy and locate tumors in different tissue systems and can

B.Y.C. Cheong, MD, FRCP(Edin) (✉)
Advanced Cardiovascular Imaging (MR/CT), Department of Radiology, St. Luke's Hospital/Texas Heart Institute, Houston, TX, USA

Departments of Medicine, Cardiology, and Radiology, Baylor College of Medicine, Houston, TX, USA
e-mail: bcheong@sleh.com

P. Angelini, MD, FSCAI
Department of Medicine, Baylor College of Medicine, Houston, TX, USA

Department of Cardiology, St. Luke's Hospital, Houston, TX, USA

Center for Coronary Artery Anomalies, Texas Heart Institute, Houston, TX, USA

J.T. Willerson, D.R. Holmes, Jr. (eds.), *Coronary Artery Disease*, Cardiovascular Medicine,
DOI 10.1007/978-1-4471-2828-1_13,

also assess organ function (i.e., left ventricular [LV] systolic and diastolic function [1–3]). In evaluating brain function [4], MRI can determine which segment of the human brain is responsible for thought, speech, movement, and sensation. Moreover, MRI angiography can show an artery's course, size, and acute pathologic characteristics and can determine whether a stenosis is present with or without contrast [5–7]. By assessing perfusion, MRI can determine the significance of an underlying stenosis in coronary artery [8] and neurovascular diseases and can provide absolute quantification of blood flow [9]. Diffusion-weighted MRI can show whether a tumor is benign versus malignant and can monitor the progress of treatment [10]. In addition, magnetic resonance spectroscopy [11] can evaluate myocardial metabolism.

A number of clinicians use MRI not only as a diagnostic modality but also to provide treatment. For instance, interventional MRI enables physicians to localize a tissue site for targeted treatment and to evaluate the treatment result in the same session, as in closure of atrial septal defects [12]. In the same manner, a recently introduced method—MRI-guided, high-intensity focused ultrasound—facilitates noninvasive tumor embolization therapy of uterine fibroids [13].

Historical Perspective

The Fourier transform, named after the nineteenth-century French mathematician Jean Baptiste Joseph Fourier, is a mathematical function that was initially applied to heat transfer and vibrations [14]. In MRI, the Fourier transform allows an image to be reconstructed from a set of encoded MRI signals; it changes these signals from a frequency/time domain to a frequency/amplitude domain. In the early twentieth century, the Larmor equation, derived by Sir Joseph Larmor, stated that the precession frequency (ω) is equal to the gyromagnetic ratio (γ) multiplied by the magnetic field strength (B_0). In 1946, Edward Purcell and Felix Bloch independently described an interesting phenomenon: when certain nuclei are placed in a magnetic field, they absorb energy in the radiofrequency (RF) range of the electromagnetic spectrum, and that energy is re-emitted when the nuclei relax back into their baseline state. Both of these scientists were awarded the Nobel Prize in Physics in 1952, and the phenomenon was termed nuclear magnetic resonance (NMR). In the early 1970s, Dr. Raymond Damadian noted that the relaxation times of tumor tissues were longer than those of normal tissues. In 1973, Professor Paul Lauterbur published the first magnetic resonance image; it showed a 4.2-mm-diameter test tube that contained two water-filled capillary tubes. The image was produced by joining a weak gradient magnetic field with a stronger main magnetic field for spatial localization of the capillary tubes. That same year, Sir Peter Mansfield also described how NMR signals could be mathematically analyzed and, subsequently, how MR gradients could be used to acquire spatial information. The name NMR was subsequently changed to MRI to avoid the word "nuclear" [14]. In 2003, the Nobel Prize in Physiology or Medicine was awarded to both Paul Lauterbur and Peter Mansfield.

During the brief history of MRI, substantial progress has been made in this field. In 1981, it took 150 s to obtain a single cardiac image measuring $4 \times 4 \times 10$ mm. In contrast, as of 2013, 25-phase cine MRI using steady-state free precession (SSFP) with parallel imaging can be performed in only three to four heartbeats (approximately 3–4 s in a patient with a heart rate of 60 beats/min), with an average temporal resolution of 40 ms and a spatial resolution of $1.8 \times 1.8 \times 8$ mm in any commercially available 1.5 Tesla (T) scanner.

Basic Principles

The following is a brief description of how an MRI image is formed. For a comprehensive review of MR physics, readers are referred to the many excellent available review articles [15–19]. A large proportion of the human body consists of fat and water. In fact, 2/3rds of the human body's weight is due to water. Therefore, hydrogen is the most abundant atom in the human body. Unlike the other elements, hydrogen has only a single proton in its nucleus. The hydrogen proton behaves like a tiny magnet, spinning on its axis, with a north–south pole. Magnetic resonance imaging makes use of this unique property of hydrogen. When placed in a steady magnetic field, these protons will become magnetized, align with the main magnetic field (either parallel or anti-parallel), and precess along the axis of the field according to the Larmor frequency. When energy is added, in the form of a RF pulse oriented perpendicularly to the main magnetic field, the magnetic vector will be deflected, tipping the net magnetization to the transverse plane. When the RF pulse is switched off, magnetization will return to its initial direction via a process called relaxation, and this will cause a signal or current to be induced in the MRI receiver coil per Faraday's Law. Images can then be created from these signals. After the RF pulse is switched off, magnetization will return to the longitudinal orientation; this phenomenon is known as T_1 or spin–lattice relaxation. The rate of relaxation is different for each tissue, and the T_1 time constant is defined as the time required for longitudinal relaxation to return to 63 % of its original value. When the RF pulse is switched off, transverse magnetization is at its maximum, and the protons are all in phase. However, immediately after the RF pulse is switched off, proton dephasing will begin; this is known as T_2 relaxation or spin-spin relaxation. The T_2 time constant is defined as the time it takes for transverse magnetization to decay to 37 % of its original value.

Because each tissue type has its own inherent T_1 and T_2 relaxation properties, each tissue has a different appearance on MRI. To generate MRI images, protons in the body must be localized to specific parts of an image by means of magnetic field gradients. The resulting signal intensity is subsequently plotted on a gray scale, and the cross-sectional images are reconstructed to allow clinician interpretation.

Indications

With improvements in coil design, magnetic gradients, and software, as well as the increased use of high-field MRI scanners, cardiovascular MRI (CMRI) has emerged as the gold standard for evaluating ischemic and nonischemic cardiomyopathy [1]. Surface echocardiography is noninvasive, relatively inexpensive, portable, and patient friendly, so it remains the first-line imaging modality for assessing cardiac function. However, by using different imaging sequences, CMRI can provide a comprehensive evaluation of the cardiovascular system. Cardiovascular MRI can be used to assess systolic and diastolic function, detect valvular stenosis and quantitate regurgitation, and measure myocardial iron levels. In addition, it can evaluate underlying coronary artery disease (CAD) by means of a vasodilator stress perfusion study or a dobutamine wall-motion assessment to determine any underlying ischemic burden or visualize the coronary arteries to reveal stenosis. Furthermore, nonischemic and infiltrative cardiomyopathies, such as arrhythmogenic right ventricular (RV) dysplasia/cardiomyopathy (ARVD/C), myocardial sarcoidosis, and amyloidosis, can be detected by CMRI. Myocardial viability can be determined by using either delayed-enhancement (DE) MRI or low-dose (LD) dobutamine CMRI to measure the recovery of myocardial contractility. Moreover, in appropriately selected patients, CMRI can provide high-quality imaging of structures outside the heart, including the entire thoracoabdominal aorta, the cerebral circulation, the pulmonary veins, and the peripheral vascular tree. Cardiovascular MRI can be performed with or without gadolinium (Gd) contrast agents, thereby avoiding the radiation and potential nephrotoxicity caused by the iodinated contrast agents used in computed tomography (CT) [20, 21]. To help guide clinicians in the use of CMRI, appropriateness criteria and expert consensus reports have been published by several professional societies [2, 3]. Table 13.1 lists the appropriate indications for CMRI [2, 3].

Table 13.1 Appropriate indications for cardiovascular magnetic resonance imaging

Disease	Indications
Ischemic heart disease	Diagnosis of patients with intermediate pretest probability who have an uninterpretable ECG or who are unable to exercise. Vasodilator perfusion CMRI or dobutamine CMRI should be used.
	Assessment of myocardial viability after myocardial infarction and before revascularization to determine likelihood of functional recovery. DE-MRI should be used.
Cardiac failure	Accurate quantification of left ventricular function.
	Assessment of specific causes of cardiac failure (e.g., infiltrative cardiomyopathy, dilated cardiomyopathy, or myocarditis).
Arrhythmogenic right ventricular dysplasia/ cardiomyopathy	Quantification of right ventricular function, chamber size, and regional wall-motion abnormalities.
	Detection of fatty or fibrosis infiltration/replacement.
Coronary artery disease	Evaluation of coronary anomalies.
	Possible assessment of coronary artery stenosis in expert centers.
Valvular heart disease	Quantification of valvular and paravalvular regurgitation and stenosis when echocardiography images are limited.
Cardiac mass	Tissue characterization of cardiac mass and anatomical evaluation of mass in relation to surrounding cardiac structures for surgical planning.
Pericardial disease	Evaluation of pericardial pathology and underlying constrictive physiology.
Congenital heart disease	Initial diagnosis and follow-up after repair.
	Ventricular function assessment and shunt quantification.
	Evaluation of extracardiac conduits.
	Surgical or percutaneous interventional planning.
Aortic disease	Comprehensive evaluation of the entire thoracoabdominal region. May be performed with or without gadolinium contrast agents.
Other vascular diseases	Comprehensive evaluation of peripheral vascular disease or mesenteric and renal arterial disease. May be performed with or without gadolinium contrast agents.
Miscellaneous	Pulmonary venous mapping for atrial fibrillation ablation.
	Quantification of myocardial iron content. T_2* imaging should be used.

Adapted with permission from Hendel et al. [2] and from Hundley et al. [3]
ECG electrocardiogram, *CMRI* cardiovascular magnetic resonance imaging, *DE-MRI* delayed-enhancement magnetic resonance imaging

Cardiomyopathies

Cardiomyopathies are defined as diseases of the myocardium associated with cardiac dysfunction. This family of diseases can be subdivided into ischemic cardiomyopathy (due to CAD) and nonischemic cardiomyopathy (not due to CAD). Cardiomyopathies were originally classified by the World Health Organization in 1980; this classification system was then updated in 1996 [22]. A newer classification scheme has also been recently introduced by the European Society of Cardiology [23]. When CAD, hypertension, congenital heart disease, and significant underlying valvular disease are not the cause of ventricular dysfunction, the remaining subtypes include hypertrophic cardiomyopathy (HCM), dilated cardiomyopathy, ARVD/C, restrictive cardiomyopathy, and unclassified cardiomyopathy.

Ischemic Cardiomyopathy (Coronary Artery Disease)

Coronary artery disease is the leading cause of death worldwide [24]. Coronary angiography is traditionally regarded as the gold standard for the evaluation of significant CAD. Nevertheless, coronary angiography is an invasive procedure that involves radiation and can have uncommon, but potentially serious, complications [25]. Computed tomographic angiography (CTA) is also being increasingly used in the evaluation of CAD. Although highly sensitive and specific, CTA still requires iodinated contrast agents and radiation exposure. Therefore, careful patient selection and preparation is needed to ensure that CTA yields high-quality diagnostic data while minimizing radiation exposure [2]. Other established methods for the assessment of CAD include stress echocardiography [26] and single-photon emission CT (SPECT) [27].

In a single session, CMRI can accurately evaluate LV systolic function, myocardial perfusion, and myocardial viability, therefore offering a "1-stop shop" for the comprehensive evaluation of underlying CAD. In addition, CMRI can also provide prognostic information, and a negative CMRI result predicts low short- to medium-term event rates [28–30].

Myocardial Perfusion

Since the early 1990s, investigators have used CMRI for the evaluation of myocardial perfusion [31]. Positron emission tomography (PET) and SPECT are currently considered the standards for myocardial perfusion imaging in the evaluation of patients with suspected CAD, as both of these methods have a high sensitivity (89 and 88 %, respectively) and specificity (86 and 74 %, respectively) for detecting such disease [32]. However, nuclear examinations have certain limitations, including attenuation artifacts in SPECT, the use of ionizing radiation, and relatively limited resolution. In a vasodilator CMRI perfusion study, the in-plane resolution is at least 3×3 mm, allowing visualization of perfusion defects in both the endocardium and epicardium. In a canine model, Lee and colleagues [33] detected a linear relationship between the relative regional flows derived from CMRI and those derived from microspheres; the correlation between both ^{99m}Tc-sestamibi and ^{201}Tl relative regional flows and microsphere relative regional flows plateaued with increasing flow. Most CMRI centers now assess myocardial viability by performing DE-MRI after the stress-rest myocardial perfusion study. This enables the clinician to distinguish perfusion defects that occur during stress and rest, suggesting critical ischemia (where the same area is viable), versus the fixed-perfusion defects during stress and rest that represent myocardial scarring (coincide with the presence of DE-MRI) [34].

According to the "ischemic cascade" theory, when a significant coronary artery stenosis is present, a perfusion abnormality will occur before diastolic dysfunction and regional wall-motion abnormalities arise; these developments are followed by electrographic ST-segment changes and, finally, the onset of chest pain [35]. Vasodilators such as adenosine and regadenoson act on the A_{2A} receptor. They increase myocardial blood flow (MBF) in normal coronary arteries by causing smooth muscle relaxation and vascular dilation; however, coronary arteries that have a significant stenosis show little or no increase in blood flow on exposure to these vasodilators. The resulting flow heterogeneity produces a steal phenomenon [36], which manifests as a reversible perfusion defect that occurs during stress perfusion and resolves during rest perfusion if critical coronary stenosis is not present.

When thallium or sestamibi is used in SPECT, signal intensity in the myocardium depends on both myocardial tissue perfusion and cell viability, as cells must be viable to extract the agent into the intracellular space. Therefore, in necrotic myocardium, the signal intensity will remain low regardless of whether or not blood flow has been restored to the region. Most of the Gd-chelates used in the United States are extracellular agents [37]; therefore, they rapidly diffuse from the intravascular space to the interstitial space. When these standard extracellular contrast agents are used, about half of the compound leaks out into the interstitial space during the first pass. Consequently, the myocardial signal intensity depends on the tissue blood volume, perfusion, the extravascular compartment, and the degree of capillary permeability. Despite these limitations, MRI measurements of myocardial perfusion correlate well with microsphere measurements, which are currently the gold standard in perfusion assessment [38].

Figure 13.1 shows the perfusion protocol used at the St. Luke's Hospital/Texas Heart Institute. During peak stress (approximately 1 min after administration of a 400-mcg intravenous bolus of regadenoson or 3 min after administration of a 140 mcg/kg/min intravenous infusion of adenosine)

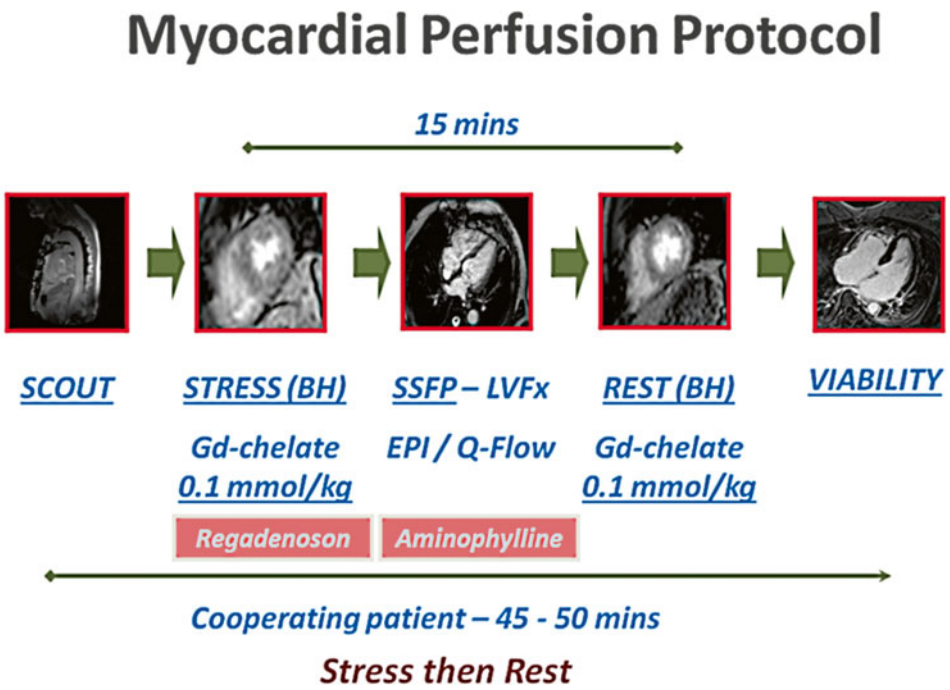

Fig. 13.1 Vasodilator myocardial perfusion protocol used at the Texas Heart Institute. This scheme illustrates the steps used to perform a myocardial perfusion study using regadenoson as the vasodilator. The study acquires functional, perfusion, and delayed-enhancement data in a single session and usually takes about 50 min to complete. *BH* breath-hold, *EPI* echo-planar imaging, *Gd-chelate* gadolinium-chelate, *LVFx* left ventricular function, *Q-flow* flow quantification, *SSFP* steady-state free precession

[36], Gd is injected through a peripheral vein at a rate of 4–6 mL/s; the dosage commonly ranges from 0.05 to 0.1 mmol/kg [39–41]. The dose of Gd should be kept low to maintain a linear relationship between image intensity and contrast concentration [42]. Furthermore, if the Gd dose is too high, T_2* effects could predominate, interfering with perfusion analysis. Figure 13.2 shows a CMRI perfusion study in which adenosine was used as the vasodilator, along with the corresponding angiographic image.

Because Gd is a T_1-shortening agent, the T_1-weighted gradient-recalled echo (GRE) sequence is the one most commonly used in clinical practice and described in the literature. With this technique, an inversion recovery or a saturation recovery pre-pulse is applied first to provide T_1 weighting. Other sequences, including the hybrid GRE-echo planar imaging and balanced SSFP sequences, have also been investigated. Although the latter 2 sequences have fast imaging speeds and high signal-to-noise and contrast-to-noise ratios [43–45], they are more prone to motion artifacts than is the GRE sequence. In the short-axis orientation, at least three slices covering the basal, mid, and apical thirds of the left ventricle are acquired during stress and rest perfusion. Despite the fact that the 3 LV slices are acquired in different cardiac phases, there appear to be no variations in coronary and MBF over the cardiac cycle. More slices can be covered if a faster imaging sequence is used or if 2 R-R intervals are used instead of 1 R-R interval.

Typically, the in-plane spatial resolution with a 1.5 T MRI scanner is approximately 2–3 × 2–3 mm, allowing detection of subendocardial hypoperfusion. Recently, though, the 3 T MRI scanner has been gaining popularity, primarily because it has a higher signal-to-noise ratio than the 1.5 T device. In addition, use of the 3 T MRI scanner in conjunction with new acceleration techniques, such as the broad-use linear acquisition speed-up technique (k-t BLAST) and sensitivity encoding (k-t SENSE), can reduce imaging time, improve LV coverage, and/or further improve spatial resolution [46–48].

Evaluation of CMRI perfusion data is commonly performed qualitatively. A perfusion abnormality is characterized by a black or dark gray area of myocardium at the peak bolus; the signal reduction should also persist longer than the first pass of Gd through the LV cavity [41]. In a recent meta-analysis of the diagnostic performance of vasodilator perfusion MR in detecting CAD, this method was determined to have a sensitivity of 89 % (95 % confidence interval [CI], 88–91 %) and a specificity of 80 % (95 % CI, 78–83 %) [49]. The reference standard was a ≥50 % diameter stenosis on coronary angiography, and all data were analyzed at the patient level. Limitations of this meta-analysis included the use of coronary angiography as the standard—so that the functional significance of the stenosis was not evaluated—and the variability in the Gd dose used in different studies.

The Magnetic Resonance Imaging for Myocardial Perfusion Assessment in Coronary artery disease Trial (MR-IMPACT), published in 2008, was a multicenter, multivendor trial that compared the diagnostic performance of perfusion CMRI with that of SPECT and coronary angiography (≥50 % stenosis) [40]. The study cohort comprised 234 patients, divided into five groups; each group received a different Gd dose. In the group that received the optimal Gd

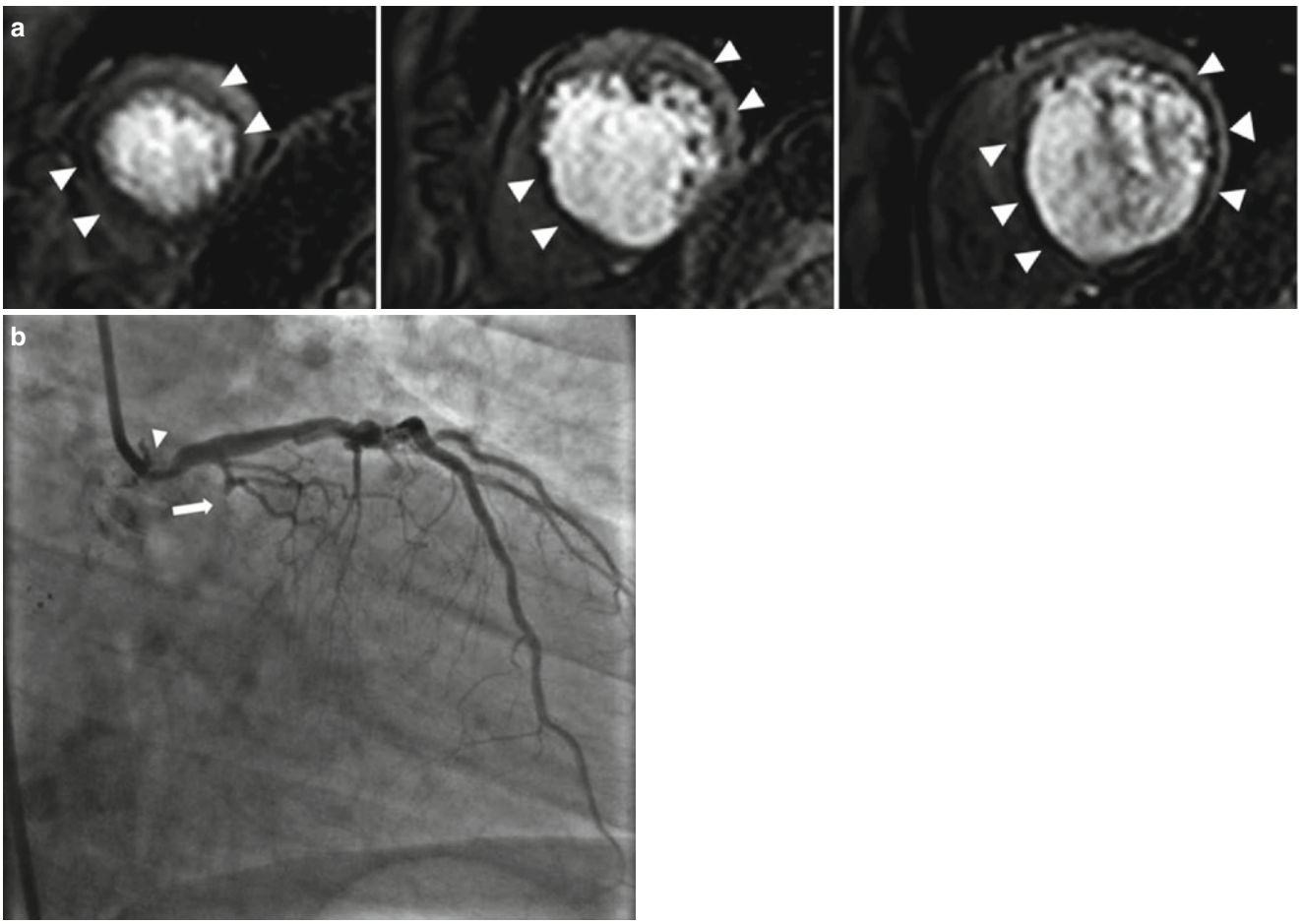

Fig. 13.2 Vasodilator stress perfusion cardiac magnetic resonance image and the corresponding invasive angiogram. Images are from a 68-year-old man who presented with chest pain. (**a**) Stress perfusion study using adenosine revealed reversible hypoperfusion involving the left anterior descending (*arrowheads*) and left circumflex territories (*arrowheads*) (rest perfusion not shown). From *left to right*: the apical-, mid- and basal-third of the left ventricle. (**b**) Invasive angiography revealed a significant left main lesion (*arrow*) and an occluded left circumflex artery (*arrowhead*)

dose, 0.1 mmol/kg, the diagnostic performance of perfusion CMRI was similar to that of SPECT, as evaluated by receiver-operating characteristic (ROC) analysis. However, when the entire SPECT study population was considered, the diagnostic performance of perfusion CMRI at the 0.1 mmol/kg Gd dose was better than that of SPECT for the evaluation of 1- to 3-vessel disease. No difference in diagnostic performance was noted, though, if the comparison was made between perfusion CMRI and electrocardiography (ECG)-gated SPECT only. The MR-IMPACT II study, a similar but larger study with 515 patients, compared both the sensitivity and the specificity of perfusion CMRI versus SPECT in CAD detection [41]. Perfusion CMRI had a higher sensitivity than SPECT (0.67 vs 0.59, respectively) but a lower specificity (0.61 vs 0.72, respectively). The results of these two studies suggest that perfusion CMRI is a safe alternative to SPECT.

In a recently reported study, more than 600 patients with suspected angina underwent both vasodilator perfusion CMRI and ECG-gated SPECT, followed by invasive angiography [50]. The sensitivity, specificity, positive predictive value, and negative predictive values were 86.5, 83.4, 77.2 and 90.5 %, respectively, for CMRI and 66.5, 82.6, 71.4, and 79.1 % for ECG-gated SPECT. The sensitivity and negative predictive values were significantly better for CMRI than for SPECT ($P<0.0001$). As Fig. 13.3 shows, CMRI also performed better than SPECT in various other categories, as indicated by ROC analysis.

The use of semi-quantitative analysis, rather than qualitative analysis, could make the assessment of perfusion abnormalities a more objective process [8, 51]. Indices that could be measured for this purpose include the peak signal intensity, up-slope, time to peak signal, mean transit time, and area under the curve. Of these, the up-slope is the most commonly used parameter. Furthermore, the stress and rest up-slope values can be normalized with the blood pool during stress and rest (Fig. 13.4). In animal studies, these

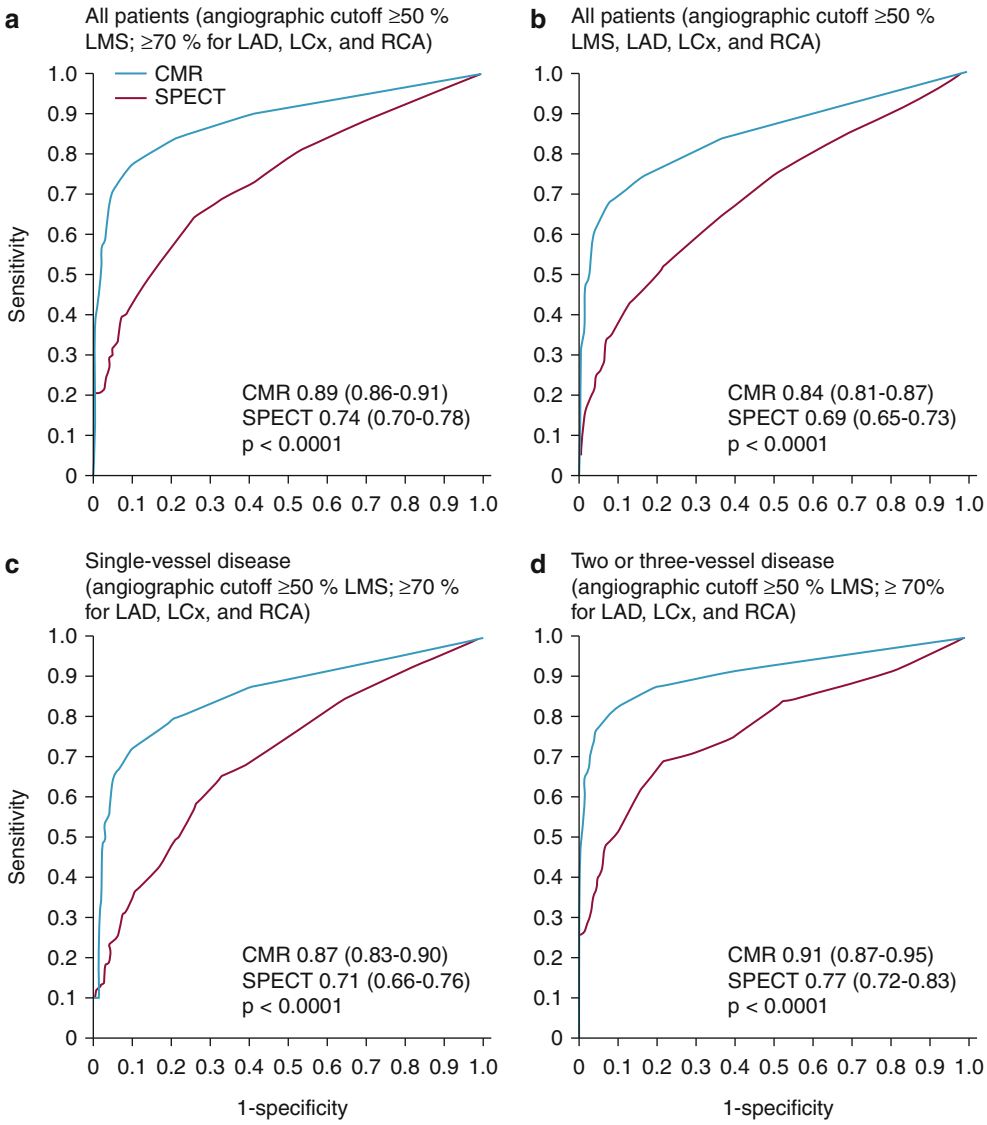

Fig. 13.3 Receiver operating characteristic (ROC) curves for cardiovascular magnetic resonance (*CMR*) and single-photon emission computed tomography (*SPECT*) by population and coronary heart disease definition. ROC curves shown for (**a**) all patients, using an angiographic cutoff of ≥50 % for the left main stem (*LMS*) and ≥70 % for the left anterior descending (*LAD*), left circumflex (*LCx*), and right coronary arteries (*RCA*); (**b**) all patients, using an angiographic cutoff of ≥50 % for the LMS, LAD, LCx, and RCA; (**c**) patients with single-vessel disease, using an angiographic cutoff of ≥50 % for the LMS and ≥70 % for the LAD, LCx, and RCA; and (**d**) patients with multivessel (2- or 3-vessel) disease, using an angiographic cutoff of ≥50 % for the LMS and ≥70 % for the LAD, LCx, and RCA (From Greenwood et al. [50]. Reprinted with permission from Elsevier Limited)

semi-quantitative indices have correlated well with flow measured by microspheres [52].

Furthermore, MBF can be quantified in mL/min/g in perfusion CMRI. For background information regarding the absolute quantification of MBF, readers are referred to several excellent previously published review articles [8, 11, 43, 53]. Models have been developed that use the myocardial and LV blood pool time-intensity curve to estimate absolute MBF. One method for MBF quantification is the Fermi function deconvolution (Fig. 13.5), in which the maximum amplitude of the transfer function reflects the absolute MBF. Therefore, perfusion can be calculated by "deconvoluting" the arterial input function from the transfer function. The arterial input function may be obtained by using the dual-bolus technique [54]. In a recent study in which a 3 T scanner was used to assess healthy volunteers during CMRI, the MBFs at rest and during stress on CMRI were 1.0 ± 0.8 and 3.0 ± 1.6 mL/min/g, respectively; these values correlated well with those obtained by ^{13}N-ammonia PET, which were 0.8 ± 0.2 for the MBF at rest and 3.0 ± 1.1 mL/min/g during stress [55].

Myocardial Viability

Left ventricular function is among the most important prognosticators in patients with CAD. Therefore, assessment of myocardial viability before revascularization is a conceptually sound and logical approach for evaluating myocardial dysfunction, because ventricular function should improve after revascularization in patients with viable myocardium [56, 57]. In the setting of ischemic cardiomyopathy with significant CAD and LV systolic dysfunction, data suggest that revascularization for patients with myocardial viability confers a survival benefit [58–60]. In a meta-analysis of >3,000 patients, ^{201}thallium SPECT, dobutamine echocardiography, and F-18 fluorodeoxyglucose PET were used to assess myocardial viability; patients with viable myocardium

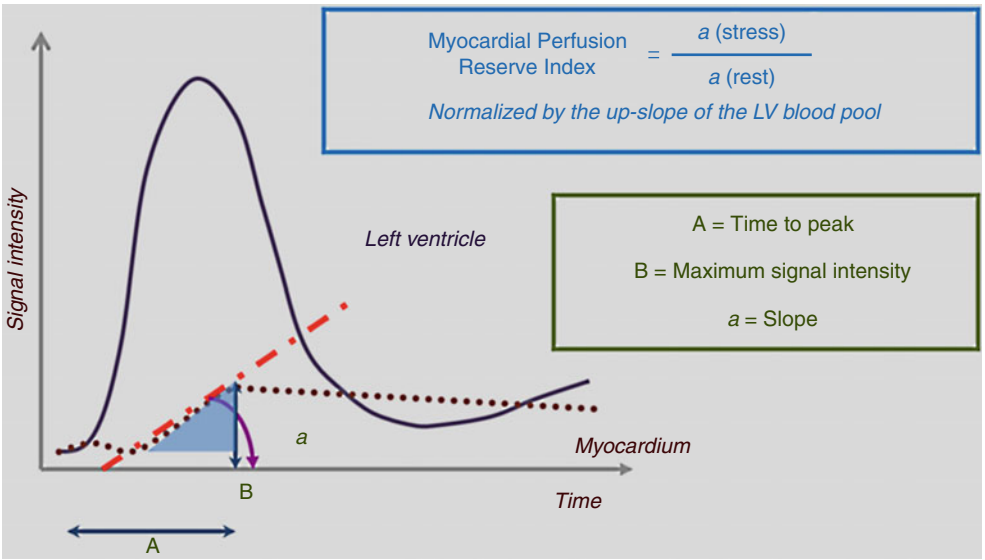

Fig. 13.4 Semiquantitative cardiac magnetic resonance imaging (MRI) myocardial perfusion analysis. The indices used for semiquantitative analysis of cardiac MRI myocardial perfusion data include time to peak (*A*), maximum signal intensity (*B*), and up-slope (*a*) (calculated as B/A). The myocardial perfusion reserve index is obtained by dividing the up-slope during stress by the up-slope at rest, using values normalized by the left ventricular (LV) blood pool up-slope

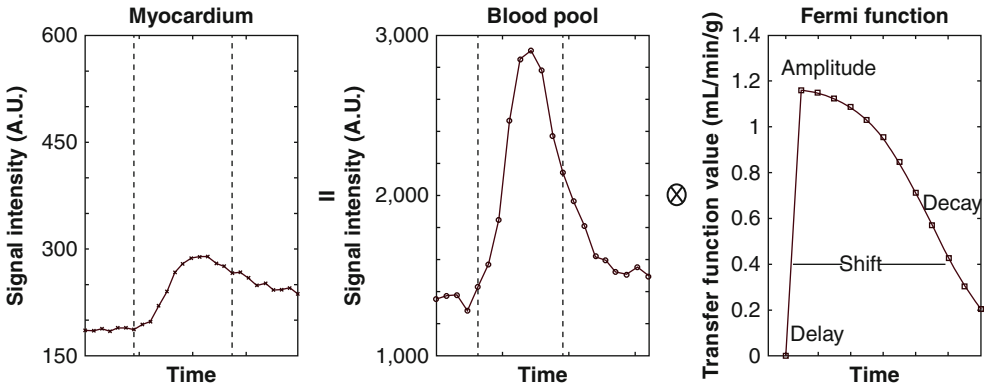

Fig. 13.5 Calculation of absolute myocardial blood flow by using Fermi function deconvolution. Briefly, f * g = h, where (f) represents the arterial input function (*middle figure*), (*) represents convolution, (g) represents the transfer function (*right figure*), and (h) represents the output signal measured from myocardial enhancement (*left figure*). The maximum amplitude of the transfer function reflects the absolute myocardial blood flow. In this example, the arterial input function was obtained by using the dual-bolus technique. *A.U.* arbitrary units (From Lee and Johnson [302]. Reprinted with permission from Elsevier Limited)

who underwent revascularization had a significant survival advantage when compared to similar patients who underwent medical therapy (annual mortality rate, 3.2 and 16 %, respectively; $P<0.0001$), but in patients with no evidence of myocardial viability, no difference in mortality was observed in those who underwent revascularization versus medical therapy (although there was a trend toward increased mortality in the revascularization group) [58]. A more recent meta-analysis of myocardial viability assessment, as determined by dobutamine stress echocardiography, SPECT, and PET, also showed that revascularization in patients with viable myocardium consistently provided a survival advantage when compared to medical therapy alone [61]. In addition, successful revascularization has been shown to improve global and regional systolic function [62] and LV remodeling [62], and it has also been shown to reduce the occurrence of adverse outcomes such as myocardial infarction (MI), heart failure, and unstable angina [63].

A variety of CMRI methods can be used to assess myocardial viability. The DE-MRI technique is relatively easy to perform, is reproducible, and provides high spatial resolution. Myocardial viability can also be evaluated by using CMRI spectroscopy, an ion transport agent (e.g., manganese), necrosis-specific agents (e.g., gadophorins), or a low dose of dobutamine, which determines contractile reserve.

In healthy myocardium, cell membranes are intact, so extracellular Gd agents cannot enter the intracellular space, which forms approximately 80–85 % of the imaging voxel. In irreversible myocardial injury, myocardial cell membranes become disrupted, allowing Gd to enter the intracellular space. As a result, the Gd concentration and the volume of distribution increase (Fig. 13.6) [64]. When the DE-MRI

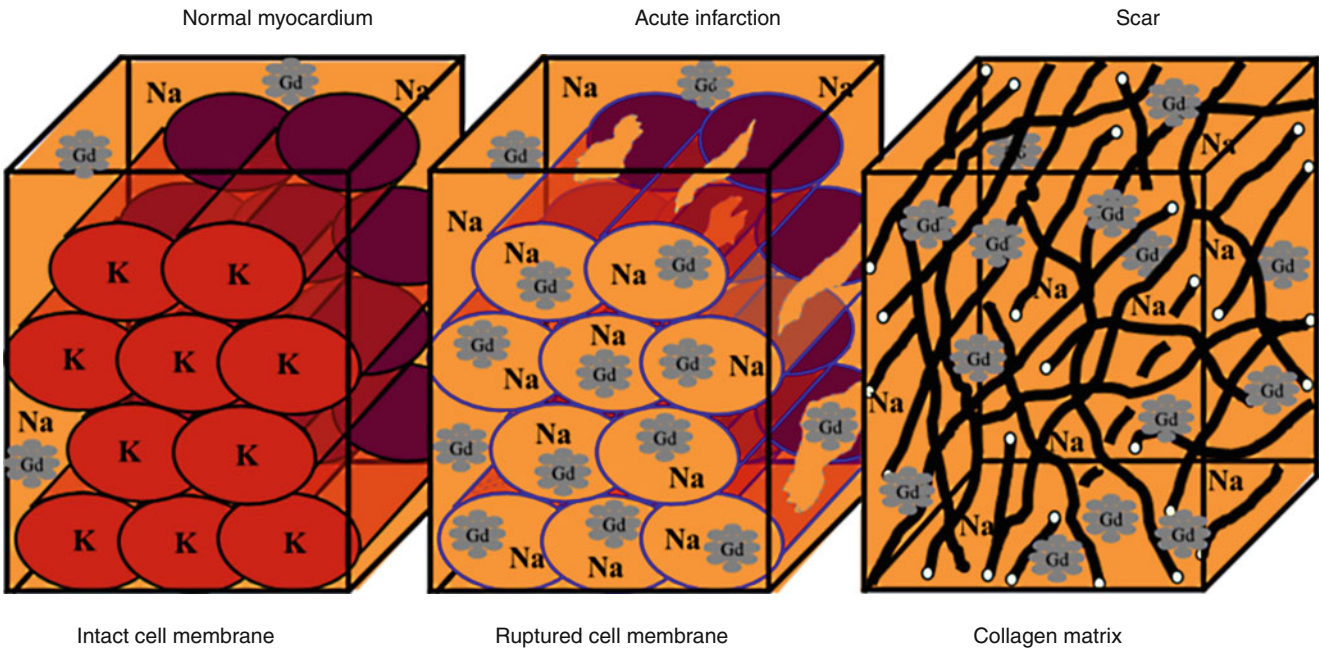

Fig. 13.6 Mechanism of delayed-enhancement magnetic resonance imaging. Gadolinium-chelates are extracellular agents; they do not cross intact cell membranes. Thus, the volume of distribution in normal myocardium is small (*left panel*). During acute myocardial infarction with cell membrane rupture, gadolinium molecules are able to diffuse into what was previously intracellular space (*middle panel*). Consequently, the volume of distribution increases, and when an appropriate imaging sequence is used, hyperenhancement is seen. In chronic myocardial infarction (*right panel*), the collagen matrix increases, resulting in an increase in the gadolinium concentration. *Gd* gadolinium, *Na* sodium, *K* potassium (From Mahrholdt et al. [64]. Reprinted with permission from Oxford University Press)

sequence is performed, a certain amount of time is allowed to pass after the R wave of the electrocardiogram before an 180° inversion pulse is applied. T_1 relaxation will then occur. The MRI operator will input the inversion time (i.e., the time required for normal myocardium to reach the "null" point), after which data acquisition is begun. Areas with irreversible injury (i.e., myocardial scar) will appear bright with high signal intensity; this is referred to as hyperenhancement. In contrast, normal, viable myocardium will have low signal intensity and will appear dark [64, 65]. The typical in-plane resolution of DE-MRI is 1.5–2×1.5–2×6–8 mm on a 1.5 T MRI scanner; this resolution is easily 20× higher than that of SPECT. When used to determine infarct size in an animal model, DE-MRI showed excellent agreement with tetrazolium chloride staining, the gold standard [66] (Fig. 13.7). In a seminal study by Kim and colleagues [67], DE-MRI was able to identify dysfunctional but viable myocardium and predict functional recovery after coronary revascularization. In that study, approximately 80 % of the dysfunctional segments with fully viable myocardium showed improvement in functionality after revascularization, whereas only 10 % of the segments with 51–75 % hyperenhancement/scar showed functional recovery (Fig. 13.8). The above-mentioned findings have been confirmed by other studies [68, 69].

Typically, 0.1–0.2 mmol/kg of Gd is administered as a contrast agent for DE-MRI. Data are usually acquired after 10–15 min of Gd administration, allowing adequate wash-in and wash-out of the contrast agent from the extracellular space of the myocardium. The input of the inversion time is critical to achieve adequate "nulling" of the myocardium. The correct inversion time can be found by using the inversion-time scout sequence, available from all major MRI vendors. Because of the introduction of the phase-sensitive inversion sequence for DE-MRI, choosing the exact nulling time has become less important [70]. The grading of DE-MRI is usually qualitative and is determined by the transmural extent of DE: 0 = fully viable, thin subendocardial = 1 to 25 %, dense subendocardial = 26 to 50 %, near-transmural = 51 to 75 %, and transmural = 76 to 100 % [67].

Regarding the study by Kim and colleagues [67], it is important to note that even in dysfunctional myocardium with no scarring, contractility improved in only approximately 78 % of segments. Some of the limitations of viability assessment have been elegantly summarized in a recent article by Schinkel and colleagues [61]. The usefulness of viability assessment may be limited for the following reasons: (1) a large amount of scar tissue adjacent to viable myocardium could limit functional recovery [71]; (2) in a severely dilated heart that has undergone significant remodeling, improvement may not be possible, despite the presence of viable myocardium [72]; (3) hibernating myocardium, in which metabolism has been significantly downregulated,

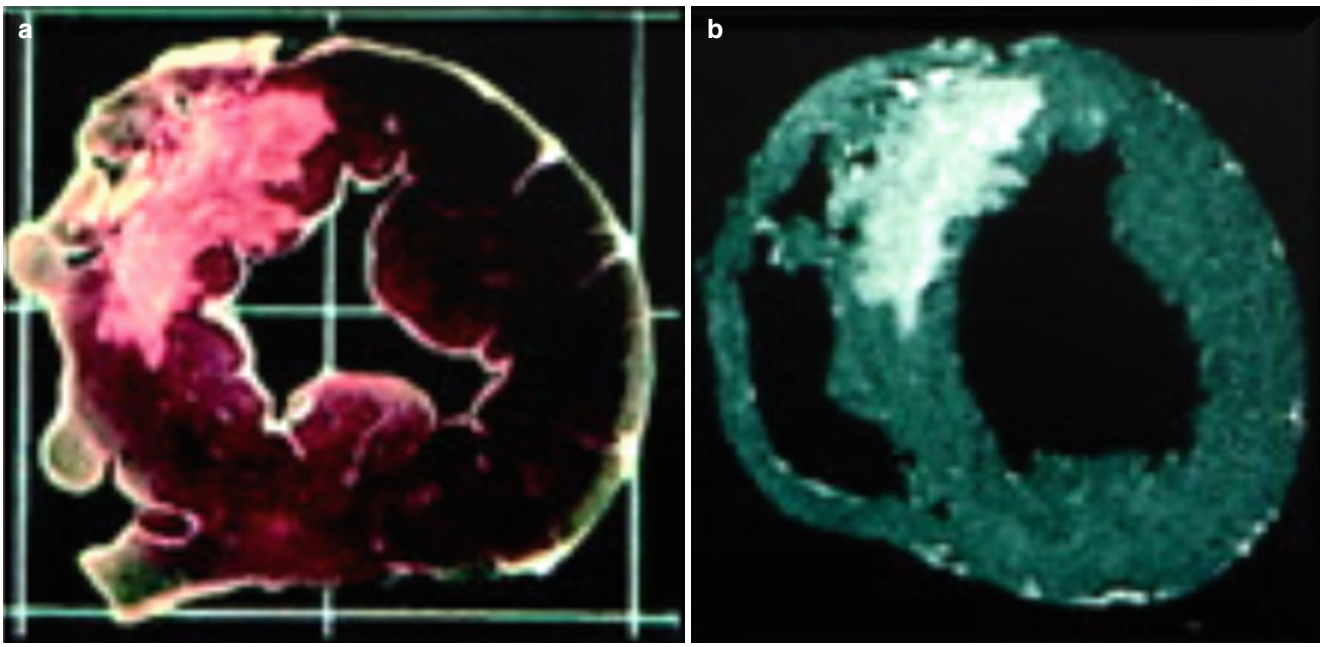

Fig. 13.7 Comparison of tetrazolium chloride (TTC) staining and ex vivo delayed-enhancement magnetic resonance imaging (DE-MRI) for determining myocardial infarct size. Images obtained by TTC staining (*left figure*) and ex vivo DE-MRI (*right figure*; acquired with a spatial resolution of 0.5×0.5×0.5 mm) show that these methods correlate extremely well when used to assess the size of a myocardial infarct. The infarct is located in the anteroseptum (From Kim et al. [66]. Modified with permission from Wolters Kluwer Health)

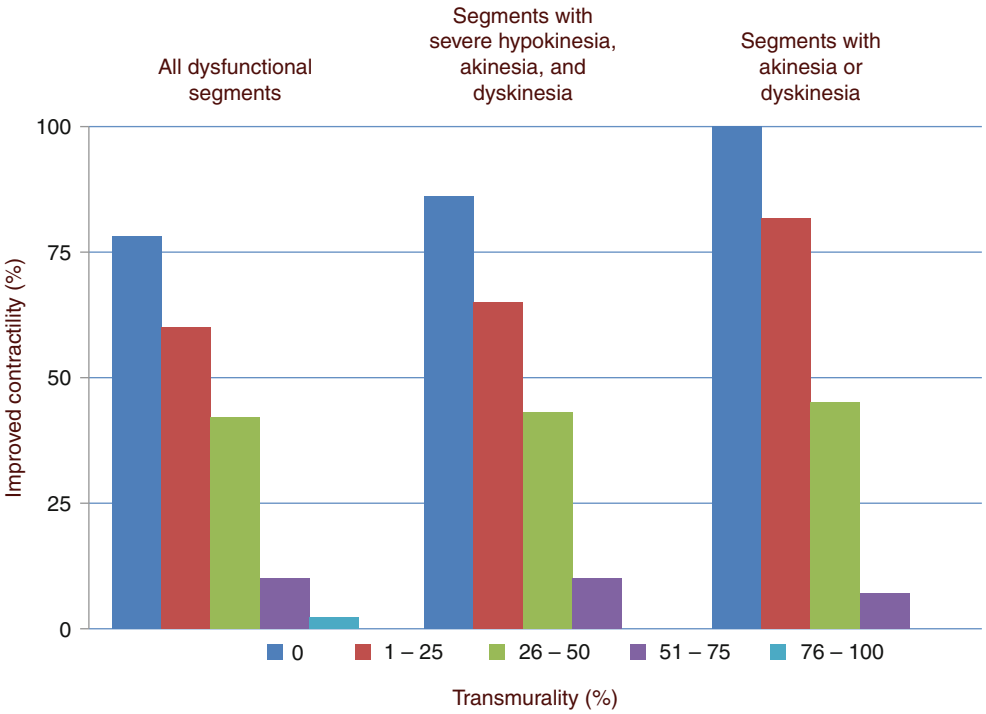

Fig. 13.8 Relationship between the degree of delayed enhancement (DE) and myocardial functional improvement after revascularization. In segments with no DE, the probability of functional recovery is high, even when akinesia or dyskinesia is present. However, in segments with substantial scarring (≥51 %), the chance of functional recovery progressively decreases (From Kim et al. [67]. Reproduced with permission from Massachusetts Medical Society)

may no longer respond to revascularization; (4) revascularization may have been incomplete or may have failed, or new myocardial injury may have occurred during revascularization; and (5) imaging must be performed at the correct time, because it could be as long as 1 year before functional recovery is seen [73].

Follow-up CMRI studies performed after revascularization consistently show only moderate functional recovery of segments that had 25–76 % DE [67, 69, 74]. In these segments, LD dobutamine CMRI is better able to predict functional recovery [74, 75]. In a recent study by Glaveckaite and colleagues [74], LD dobutamine performed better than

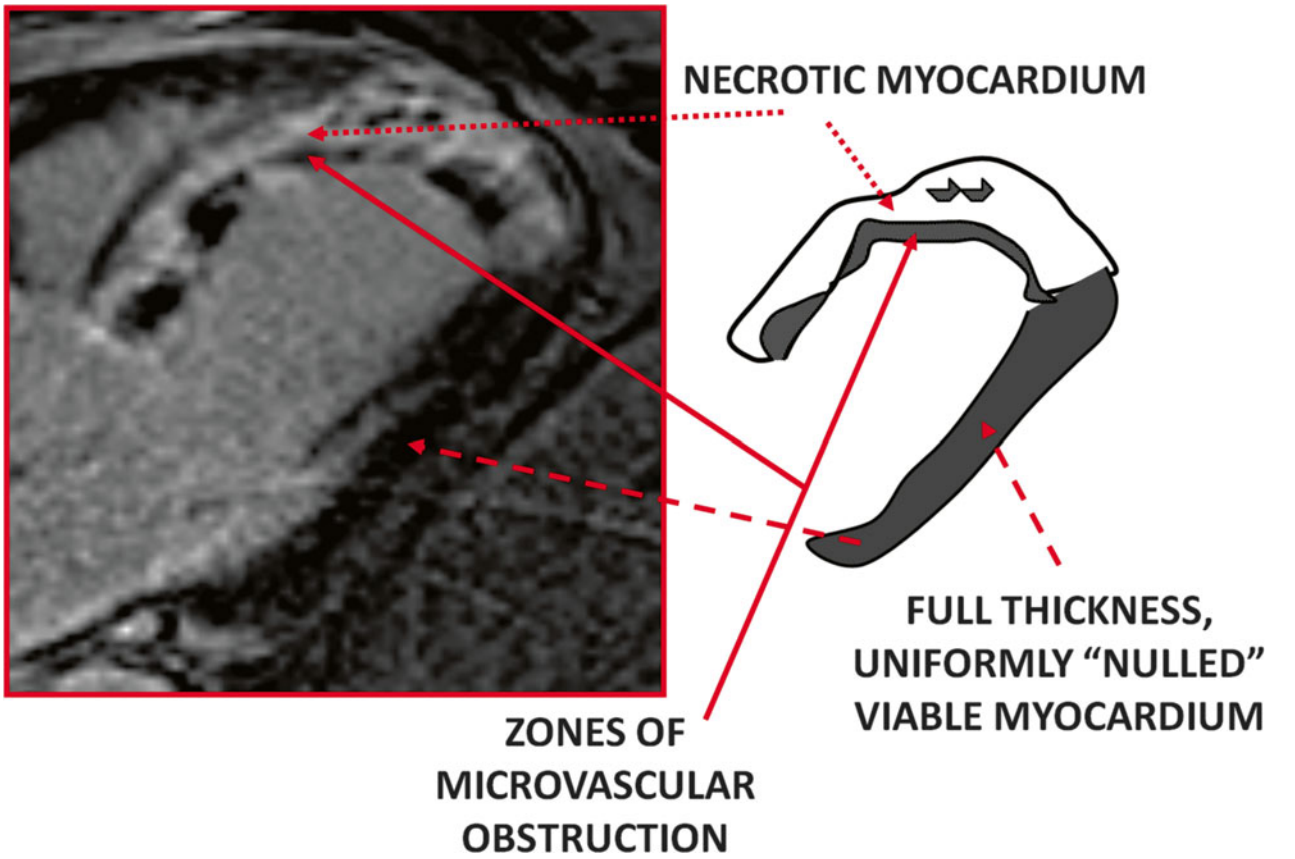

Fig. 13.9 Delayed-enhancement magnetic resonance imaging (DE-MRI) of microvascular obstruction. This image is from a patient who presented with acute myocardial infarction of the left anterior descending artery 10 h after onset. Percutaneous intervention was performed immediately; however, DE-MRI performed on the third hospital day revealed near-transmural to transmural myocardial infarction. The image, taken in the left ventricular outflow tract orientation 15 min after gadolinium-chelate administration, shows myocardial infarction in the entire anteroseptum and extending into the apex

DE-MRI at predicting functional recovery in segments with 26–75 % DE ($P = 0.043$), as shown by ROC analysis. However, the combination of DE-MRI and LD dobutamine was not found to provide more information than LD dobutamine alone. In general, DE-MRI offered similar, if not better, sensitivity than LD dobutamine MRI did in predicting functional recovery; however, LD dobutamine MRI offered better specificity than DE-MRI did. Finally, the investigators also found that the predictive value of DE-MRI did not increase when the thickness of the viable myocardium in each segment was also considered [74].

During an acute MI, the "no-reflow" phenomenon may be visualized with coronary angiography. This phenomenon results from obstructions in the microcirculatory system, which includes vessels <200 μm in diameter [76]. This microvascular obstruction (MO) can be imaged by DE-MRI after Gd administration (Fig. 13.9) and can be detected during an acute MI, especially an ST-segment–elevation MI (STEMI), with or without percutaneous intervention. Such obstruction is especially common when the patient is elderly, the thrombus burden is large, the baseline coronary flow is poor, or reperfusion is delayed. When visualized with DE-MRI, MO is seen as regions of low signal intensity surrounded by hyperenhancement. Although DE-MRI is used for this purpose, there is no consensus regarding the optimal imaging sequence to use for MO or the appropriate timing of imaging after Gd administration. For example, some studies suggest that images should be acquired a few minutes after Gd administration (early) [77, 78], whereas others suggest the use of a standard imaging time of 10–15 min after Gd administration (late) [77–81]. Other imaging methods include a first-pass perfusion sequence [78, 80–82] and cine SSFP imaging [83]. In 1 study, the median mass of MO was found to be greatest on first-pass perfusion, followed by early and late DE-MRI (4.7, 2.3, and 0.2 g, respectively) [78].

Microvascular obstruction is common after an acute MI, even after successful reperfusion, and patients with MO have a larger infarct size than those without MO [79, 80, 82, 84]. In addition, Kaplan-Meier analysis has indicated that survival is worse in patients with MO [79, 80, 84]. The presence of late/persistent MO is a significant prognosticator for major adverse cardiovascular events [79, 80], indicating that more

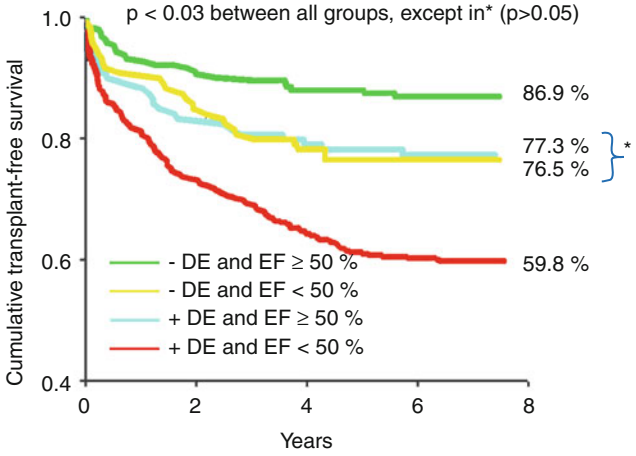

Fig. 13.10 Transplant-free survival, stratified by delayed enhancement (*DE*) status (+/−) and ejection fraction (*EF*). Kaplan-Meier transplant-free survival analysis was performed for four patient groups: (1) DE absent and EF ≥50 %, (2) DE absent and EF <50 %, (3) DE present and EF ≥50 %, and (4) DE absent and EF <50 %. Traditionally, patients with a preserved ejection fraction were regarded as having a good prognosis. In this analysis, however, patients who had DE and preserved left ventricular systolic function (i.e., EF ≥50 %) had similar outcomes to those who had no DE and a left ventricular ejection fraction of <50 % (blue and yellow lines, respectively). Patients with DE and a left ventricular ejection fraction <50 % had the worst prognosis (From Cheong et al. [28]. Modified with permission from Wolters Kluwer Health)

aggressive therapy and vigilant clinical follow-up are needed for patients who have MO.

Data from multiple studies suggest that besides playing a major role in the assessment of myocardial viability, DE indicates a worse prognosis in patients with ischemic or non-ischemic cardiomyopathy. In a study of 857 patients, the presence of DE was an independent predictor of death/cardiac transplantation in the patients with and without CAD (Fig. 13.10) [28]. Similarly, in a cohort of patients with suspected CAD who underwent DE-MRI, significant survival differences were found between the patients with DE and those without DE [85]. In addition, the presence of DE had the highest hazard ratio (HR) when compared to other traditional clinical factors in predicting cardiac mortality and major adverse cardiac events; patients whose percentage of DE was in the lowest tertile had a 7-fold increase in major adverse cardiac events. In a recent multicenter observational study, more than 1,500 patients underwent routine CMRI, which included DE-MRI and LV ejection fraction (LVEF) measurements. In this study, significant predictors of all-cause mortality included older age, the presence of CAD, and a greater number of DE segments [86]. In addition, patients with preserved LV systolic function (LVEF ≥50 %) who had >4 segments with DE had significantly poorer survival than patients who had ≤4 DE segments. The authors of the above-mentioned studies have provided two possible explanations as to why DE is associated with poorer outcomes in patients with CAD: first, myocardial scarring could act as a substrate for ventricular tachyarrhythmia [87, 88], and second, the presence of DE could be a marker of significant underlying atherosclerosis [85].

Two recent articles described the use of DE-MRI for patient risk assessment to determine the appropriate use of implantable cardioverter-defibrillator (ICD) therapy. In the study by Klem and colleagues [89], 137 patients underwent CMRI, and 104 of these patients had an ICD placed. The investigators found a significant increase in the primary endpoint event rate (all-cause death, sudden cardiac death [SCD], or ICD discharge) when the amount of DE was >5 % of the LV mass; however, the event rate then plateaued with further increases in DE. In addition, DE of >5 % was the only significant independent predictor of SCD or ICD discharge, with an HR of 4.8 (95 % CI, 1.7–13.7; $P = 0.0004$). The authors then used an LVEF cut-off of 30 % to assess the effect of DE % on the event rates of SCD and ICD discharge; they obtained the following results: (1) LVEF >30 %, DE ≤5 %, 3-year event rate = 6 %; (2) LVEF >30 %, DE <5 %, 3-year event rate = 25 %; (3) LVEF ≤30 %, DE ≤5 %, 3-year event rate = 11 %; and (4) LVEF ≤30 %, DE >5 %, 3-year event rate = 35 %. These results suggest that even in patients with a low LVEF (≤30 %), the presence or absence of significant DE could affect the occurrence of these adverse outcomes. A similar trend was also seen in all-cause mortality. The second study to assess the use of DE-MRI for risk stratification followed up 257 patients after ICD implantation; both the percentage of DE (HR, 1.8; 95 % CI, 1.1–2.8; $P = 0.02$) and the number of transmural segments (HR, 1.4; 95 % CI, 1.2–1.7; $P = 0.001$) were independent predictors of the need for ICD therapy in this study [90].

Area-at-risk Assessment

Area-at-risk (AAR) is defined as the region of myocardium that becomes ischemic during an acute coronary occlusion [91]. The T_2-weighted imaging used in CMRI is sensitive to water-bound protons, and it has been postulated that this method can be used to detect myocardial edema, regardless of whether the edema is caused by inflammation or coronary occlusion [92]. From data collected by T_2-weighted imaging and DE-MRI, the following parameters can be computed: (A) AAR = myocardial edema volume / volume LV mass; (B) percentage of infarct size = volume infarct / volume LV mass; (C) myocardial salvage = (A) – (B); and (D) myocardial salvage index = (C) / (A) (Fig. 13.11) [93]. In a study by Ugander and colleagues [94], measurements of the AAR myocardium after coronary occlusion taken by T_2 mapping were in good agreement with those taken by the reference standard of microsphere blood flow assessment ($R^2 = 0.96$) in a canine model. In several publications, T_2-weighted imaging has been used to assess myocardial edema or myocardial salvage during acute coronary syndrome [93, 95–98].

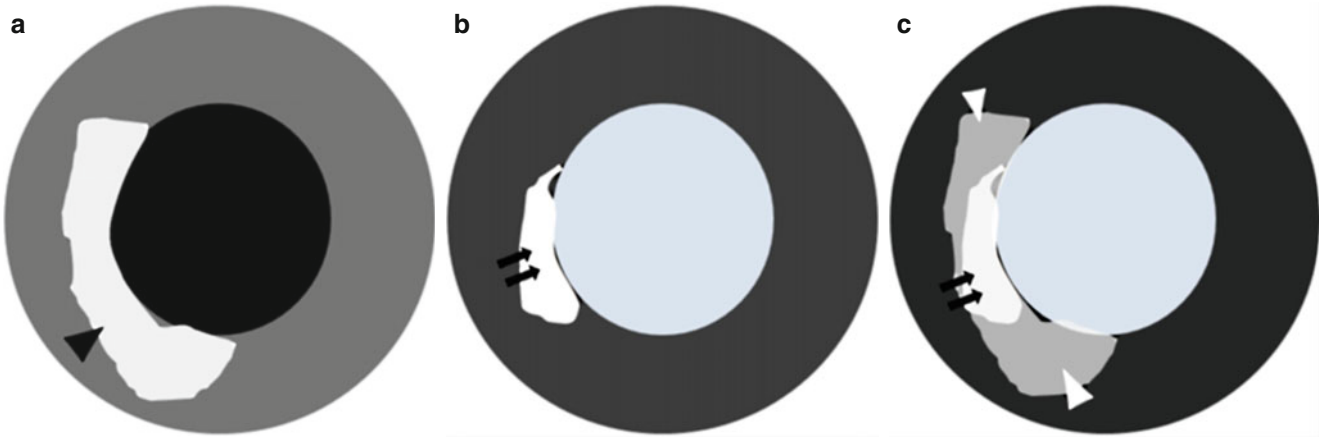

Fig. 13.11 Diagram depicting how the area-at-risk is measured. (**a**) Representation of a T_2-weighted image of myocardial edema (*black arrowhead*) in the interventricular septum, indicating area-at-risk. (**b**) The corresponding delayed-enhancement (DE) magnetic resonance imaging results, showing the presence of a subendocardial scar (*black arrows*). Note that the area of DE is less than the area of myocardial edema. (**c**) The salvaged myocardium (**b**–**c**) is indicated by the grey area (*white arrowheads*)

To define the prevalence and significance of myocardial edema in patients with non-STEMI, Raman and colleagues [97] analyzed data from 88 patients who had non-STEMI and adequate CMRI studies before coronary angiography. These data included results from triple inversion T_2-weighted edema imaging and DE-MRI. The treating physicians were blinded to the CMRI results. All CMRI data were analyzed in a semi-quantitative fashion. Revascularization was required for significantly more patients with myocardial edema than for patients without edema (88 % vs 26 %, respectively; P <0.0001). When compared to patients without myocardial edema, those with myocardial edema had a higher risk of having a cardiovascular event or dying within 6 months after the index event (HR, 4.5; 95 % CI, 1.0–20.0; P = 0.05).

Eitel and colleagues [93] analyzed the CMRI results of more than 200 patients with STEMI to determine the prognostic significance of the myocardial salvage index in reperfused STEMI. For each patient, CMRI was performed within 4 days of the index event. The analyzed parameters included myocardial edema, infarct size, myocardial salvage index, and standard LV functional parameters. Higher myocardial salvage index values correlated with shorter symptom-to-percutaneous intervention times (i.e., symptom-to-balloon time). In multivariable regression analysis, only the myocardial salvage index was an independent and significant predictor of the study endpoint, which was death, reinfarction, or new congestive cardiac failure within 6 months of the index event (HR, 0.93; 95 % CI, 0.91–0.96; P <0.001). This means that major adverse cardiovascular events are less likely to occur in patients with a higher myocardial salvage index value than in patients with a lower value. In a second publication, Eitel and colleagues [99] provided the results of a follow-up study of the above-mentioned patients (median follow-up period, 18 months). The investigators found that the incidence of major adverse cardiovascular events or death was significantly lower in patients with a median myocardial salvage index of ≥48.3, which indicates a larger degree of myocardial salvage (P <0.0001 for both comparisons). In this study, the percentage of DE was the most significant predictor of major adverse cardiac events—specifically, a composite of death, reinfarction, and new congestive heart failure (HR, 1.06; 95 CI%, 1.03–1.09; P <0.001). Although the myocardial salvage index was not found to be a significant predictor of major adverse cardiac events, it was a significant independent predictor of death (HR, 0.93; 95 CI%, 0.91–0.96, P <0.001). In contrast, traditional prognosticators, such as age, diabetes, and percentage of DE, were not significant predictors of death. In addition, infarct size and myocardial salvage were noted to have a strong inverse correlation (r = −0.86; P <0.001).

In a study of 137 patients with acutely reperfused STEMI, the myocardial salvage index was determined to be the most significant predictor of both early ST-segment resolution (B coefficient = 0.61; P <0.0001) and adverse remodeling, defined as a ≥15 % increase in LV systolic volume on the 4-month follow-up CMRI (odds ratio, 0.64; 95 % CI, 0.49–0.84; P = 0.001) [100].

Larose and colleagues [98] studied 101 patients with acute STEMI who underwent CMRI 12 h after primary percutaneous intervention and 6 months after the index event. The patients were followed up for 2 years. Data from CMRI were used to quantitatively examine LV function and assess DE-MRI of the entire left ventricle; first-pass perfusion and T_2-weighted images were obtained in the apical, mid, and basal left ventricle. The myocardial salvage index was also computed. All of the above-mentioned variables were significant predictors of LV systolic dysfunction at 6 months on univariate analysis, but the percentage of DE measured

during the acute STEMI was the best independent predictor in multivariable analysis (odds ratio, 1.33; 95 % CI, 1.09–1.78; $P=0.002$).

The use of DE-MRI for prognostication has been well established in multiple publications [28, 85, 86]. In the assessment of novel myocardial perfusion strategies, the myocardial salvage index could prove to be a better prognosticator than the percentage of DE because the final infarct size depends on various factors, including the collateral blood flow, duration of ischemia, and extent of AAR. There is a close association between DE size and AAR; the myocardial salvage index corrects the infarct size to the amount of AAR [100]. The myocardial salvage index could be useful in assessing the safety and efficacy of new reperfusion strategies.

The technical limitations of T_2-weighted imaging are well summarized by Wince and colleagues [101]. One such limitation is that the contrast-to-noise ratio is low between edematous and normal myocardium in conventional T_2-weighted imaging. Also, wall-motion abnormalities associated with acute myocardial injury can lead to "slow blood flow," creating a high signal that can be mistaken for edema. In addition, incomplete dark-blood preparation due to reduced cardiac motion and misregistration between the preparation and imaging phase in hypokinetic myocardium can result in a higher signal intensity than that in normal myocardium. Finally, in most studies, the area of edema is arbitrarily defined as a region with a signal intensity that is >2 standard deviations above that of a remote region. Improved imaging sequences [102, 103] and quantitative T_2 measurements [104] may overcome some of these limitations.

Nonischemic Cardiomyopathy

Cardiovascular MRI has emerged as the gold standard for the assessment of nonischemic cardiomyopathy [1–3]. Surface 2-dimensional (2D) echocardiography remains the first-line, noninvasive imaging modality used for patients who present with cardiomyopathy. However, 2D echocardiography has a few potential limitations. First, patient body habitus could affect image quality, especially in patients who are obese or who have chronic obstructive pulmonary disease. Second, the apex may not be readily visible (i.e., in patients with apical ballooning). Third, 2D echocardiography has limitations regarding the accurate assessment of the right ventricle, which is of great importance when one is assessing diseases such as ARVD/C. Fourth, 2D echocardiography relies on geometric assumptions for chamber and mass quantification. Fifth, 2D echocardiography has a limited ability to characterize certain tissues, including fat, fibrosis, and scar.

The following sections provide a brief summary of the role CMRI plays in the diagnosis of various cardiomyopathies commonly encountered in day-to-day clinical practice.

Imaging Techniques

Cine Imaging

Steady-state free-precession cine imaging is the most widely used imaging sequence for functional assessment by means of CMRI, especially for the right ventricle. Parallel imaging can also be used in conjunction with SSFP imaging to reduce the imaging time and enhance patient comfort, to improve the spatial resolution, or both; these benefits come at the expense of a slightly reduced signal-to-noise ratio.

Spin Echo

Tissue characterization is commonly performed with the turbo/fast spin echo sequence, using T_1- or T_2-weighting. A double inversion recovery preparation scheme is commonly used to suppress the blood signal. Briefly, an initial nonselective 180° pulse is applied to the entire imaging volume. Then, a second 180° pulse is applied to the slice of interest immediately after the first 180° pulse to restore the longitudinal magnetization; note that magnetization outside the slice of interest will remain inverted. The acquisition sequence is started after an inversion time that corresponds to the time when blood from outside the imaging slice crosses zero during recovery after the 180° inversion pulse; therefore, the blood will generate no signal. With the application of another inversion pulse to suppress the fat signal, a triple inversion recovery preparation scheme will have been achieved.

For the detection of myocardial edema, the T_2-weighted spin echo sequence is especially useful when long T_2 water-bound protons are used as the contrast-generating mechanism, resulting in high signal intensity in edematous tissue [92]. To evaluate fatty infiltration or replacement, as would be needed for the assessment of ARVD/C, a fat saturation sequence is employed. Examples of these sequences include short inversion-time inversion recovery (STIR), spectral presaturation with inversion recovery (SPIR), spectral attenuated inversion recovery (SPAIR), and the principle of selective excitation technique (ProSet).

Spin echo images have certain limitations. For example, the contrast-to-noise ratio between normal and abnormal myocardium is low; the image quality is affected by background field inhomogeneity; and in areas of reduced myocardial contraction, slow blood flow could result in a bright signal that could be mistaken for myocardial edema. The presence of a significant arrhythmia can also affect image quality. In addition, through-plane motion can cause a loss of the posterior/inferior wall signal, and the use of phase array coils can cause signal intensity variability.

Dixon Technique

Another method of imaging fat (and water) is the Dixon technique [105]. This chemical-shift–based water-fat separation technique was originally described by Dixon in

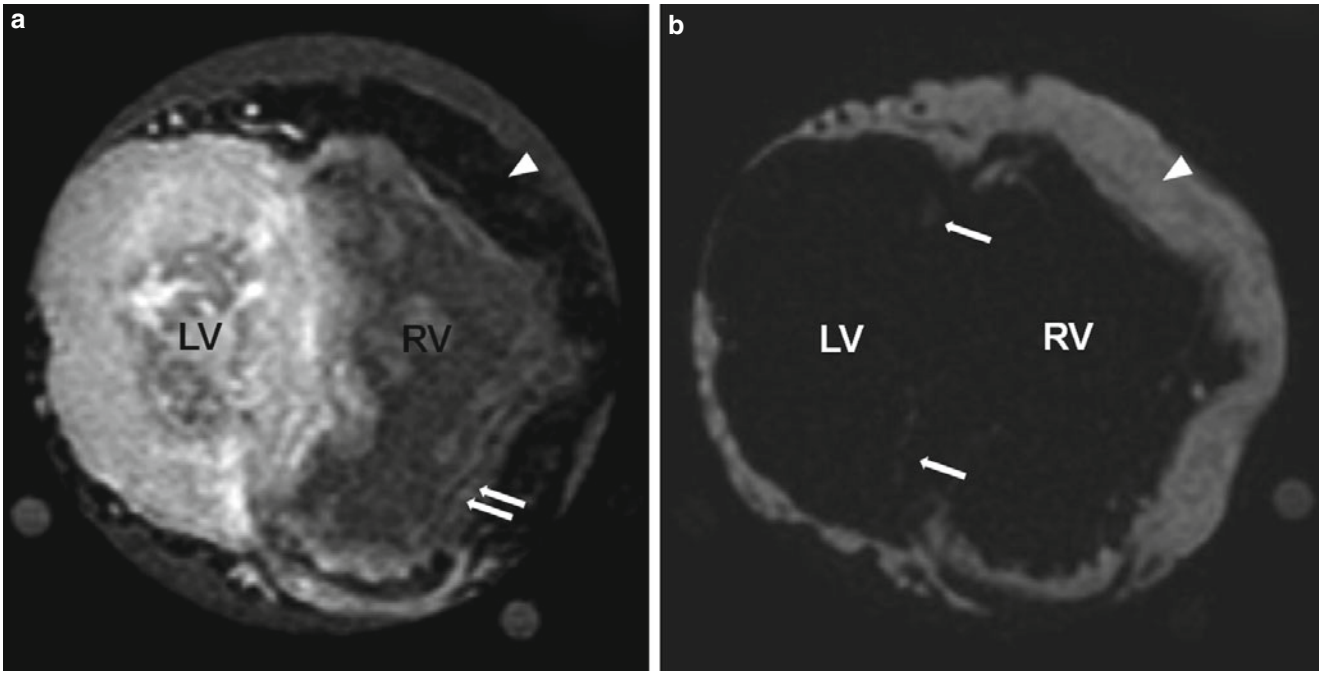

Fig. 13.12 An explanted heart imaged by using cardiac magnetic resonance imaging (MRI) with the Dixon method. The heart was from a 23-year-old man who had cardiomyopathy and a histologic diagnosis of arrhythmogenic right ventricular dysplasia. The explanted heart was imaged by using a T_1-weighted sequence with the Dixon method; (**a**) is the water image and (**b**) is the fat image. The signal intensity for fat is low in the water image and high in the fat image. *Arrowheads* in both images indicate epicardial fat. *Double arrows* in (**a**) indicate the presence of fat in the right ventricle (*RV*). *Single arrows* in (**b**) indicate fat in the left ventricle (*LV*). The image spatial resolution is 1 × 1 × 2 mm

1984 [106]. Protons in water and fat have different resonance frequencies, and phase shifts occur because of these frequency differences. As a result, fat and water can be separated by using the improved multi-echo Dixon technique, which is less susceptible to background magnetic field inhomogeneity than are traditional fat-suppression techniques. This method can be incorporated into contrast-enhanced or cine imaging to achieve a high signal-to-noise ratio with a shorter imaging time, especially when parallel imaging is used [107]. Some clinical applications of the multi-echo Dixon technique include detecting fatty infiltrates in MI, imaging cardiac tumors (such as lipomas), and evaluating ARVD/C (Fig. 13.12) [105].

Delayed-enhancement MRI

The DE-MRI sequence is commonly performed approximately 10–15 min after Gd enhancement. Different types of nonischemic cardiomyopathy can produce different enhancement patterns, such as mid-myocardial, subepicardial, and transmural (Fig. 13.13). A DE pattern alone may not be specific enough to diagnose a disease, but when considered in conjunction with the patient's clinical presentation, symptoms, and extravascular findings (e.g., hilar adenopathy in sarcoidosis), DE-MRI findings can help physicians arrive at the correct clinical diagnosis.

T_1 Imaging

In certain pathological conditions, such as CAD, infiltrative diseases (e.g., amyloidosis), and cardiac hypertrophy (e.g., systemic hypertension, HCM), fibroblasts proliferate and extracellular collagen deposition and fibrosis increase with structural and biomedical remodeling [108]. In a rat model, myocardial fibrosis has been associated with ventricular remodeling, increased myocardial stiffness, and a reduction in systolic function [109]. Fibrosis can be arrhythmogenic because it can lead to electrical conduction disturbances. In humans, the interstitial/extracellular space accounts for approximately 20–25 % of the total heart volume [110]. With fibrosis, the extracellular space increases. Endomyocardial biopsy is the gold standard for evaluating myocardial fibrosis; however, it is an invasive procedure with known morbidity and mortality hazards. Furthermore, such a biopsy could result in sampling error.

In CMRI, there is T_1 shortening after Gd administration. The signal change is related to the extent of the extracellular space. When irreversible injury is present, the intracellular spaces will be directly exposed to Gd. As a result, there will be an apparent increase in the extracellular space and volume of distribution, increasing the signal strength after Gd administration when an appropriate imaging sequence is used (e.g., DE-MRI). Similarly, in an infiltrative cardiomyopathy, such

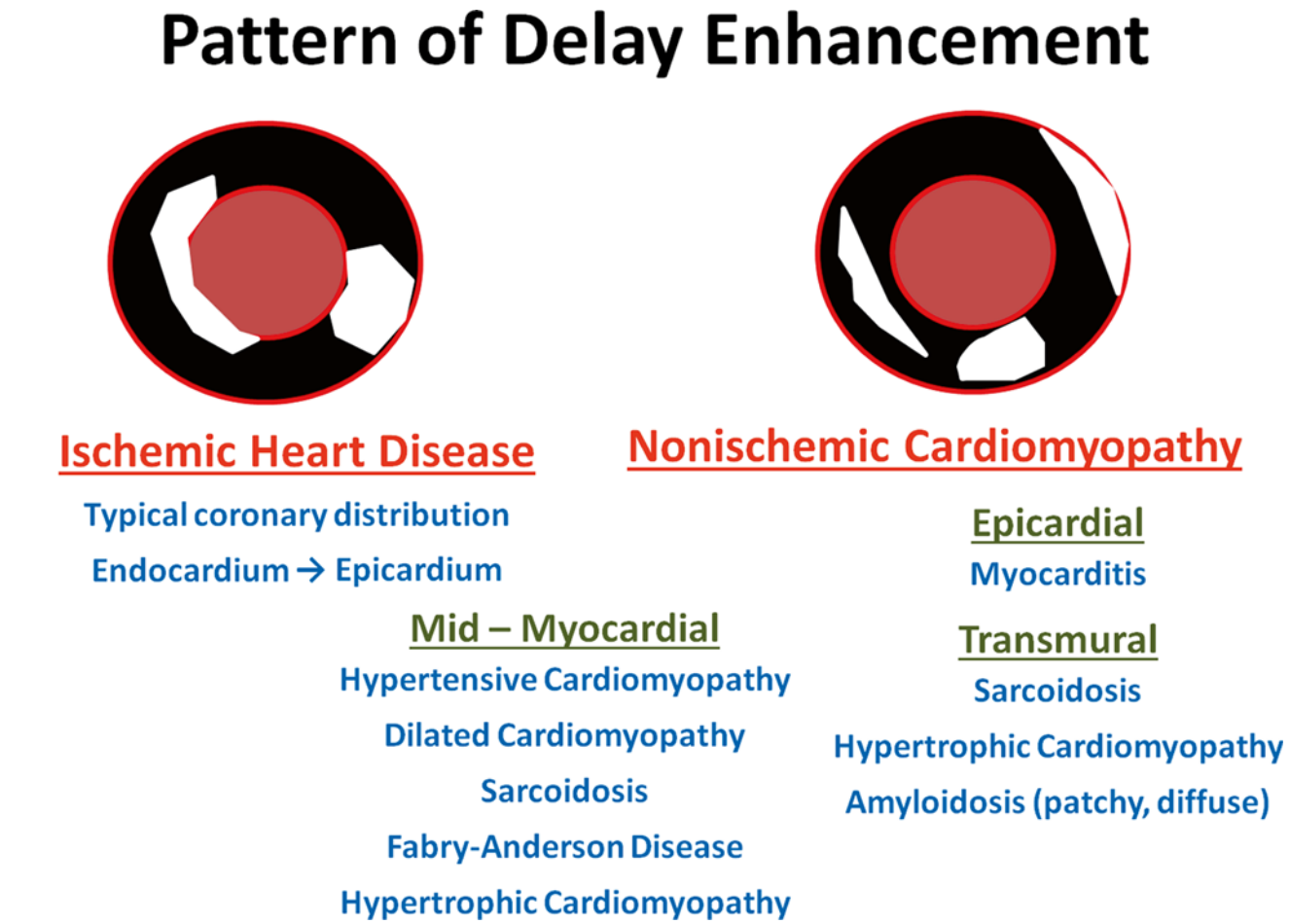

Fig. 13.13 Differential patterns of delayed enhancement (DE) in ischemic and nonischemic cardiomyopathies. In patients with coronary artery disease, DE is usually present in the endocardium of the involved coronary territories and, depending on the degree of myocardial injury, may extend toward the epicardium. In patients with nonischemic cardiomyopathy, the pattern of DE is less specific; it may be subendocardial, mid-myocardial, or subepicardial, and overlap is often seen in different disease processes. Nonetheless, when this information is combined with the appropriate clinical information and with morphologic and extravascular findings (such as asymmetric hypertrophy and hilar adenopathy), clinicians are frequently able to arrive at the correct diagnosis. When images are acquired by using DE-MRI, normal myocardium is dark and DE is bright

as amyloidosis, the expansion of extracellular space could result from fibrosis or amyloid protein accumulation [111]. T_1 mapping provides a more objective assessment of the extracellular space and, therefore, of fibrosis [112]. The extracellular volume fraction (ECF) can be obtained by using the formula $(\Delta R_{1\ \text{Myocardium}}/\Delta R_{1\ \text{Blood}}) \times (1\text{-hematocrit})$, where R_1 is the reciprocal of T_1 (T_1 is the longitudinal relaxation time constant) and ΔR_1 represents the difference between R_1 before and after contrast [113].

T_2 Imaging

Both inflammation (as occurs in myocarditis) and ischemia-reperfusion injury (as occurs in acute coronary syndrome) can lead to myocardial edema [114]. In the initial stages of edema, an Na^+/K^+ pump dysfunction leads to the intracellular accumulation of Na^+, resulting in an influx of water due to an increase in osmotic pressure. With a prolonged insult, capillary membrane damage leads to interstitial edema due to intravascular water leakage. Interstitial edema can cause systolic and diastolic dysfunction and can promote myocardial stiffness and fibrosis [115]. Discriminating between intra- and extracellular myocardial edema by means of noninvasive imaging is difficult.

The T_2-weighted imaging sequence is used clinically to detect myocardial edema, which produces a high signal intensity with this approach. Recently, some improved versions of T_2-weighted imaging have been described. For example, the T_2-prepared SSFP sequence has been shown to have fewer artifacts and higher accuracy than the traditional fast spin echo sequence [103], and a hybrid sequence has been described that combines the advantages of SSFP and turbo spin echo imaging [102]. In addition, quantitative T_2 mapping to detect myocardial edema has been shown to increase objectivity and improve accuracy while also addressing the potential limitations of traditional spin echo imaging sequences [104].

T_2* Imaging

Serum ferritin is commonly measured to determine body iron stores; however, it is not a good indicator of the myocardial iron level. Hepatic iron overloading leads to a reduction in signal intensity, and the T_2 value is reduced when iron is present. Initially, the spin echo T_2 sequence was used to quantify tissue iron content, but the gradient-echo T_2* sequence has shown greater sensitivity to iron deposition [116]. Using the gradient-echo sequences to measure T_2* has the advantage of a shorter acquisition time; therefore, it is possible to produce a motionless image by using a single breath-hold with ECG-gating. Furthermore, the gradient-echo sequence is more sensitive to the paramagnetic effect of iron because it does not require the 180° refocusing pulse used in spin echo sequences to correct for field inhomogeneities [117]. However, the quality of bright-blood gradient-echo images can be affected by noise, motion, and blood artifacts [118]. In bright-blood images, the blood signal spills into the myocardium, potentially affecting T_2* quantification. To reduce blood-signal contamination of the myocardium, a double inversion recovery prepulse sequence can be applied to suppress the blood signal, giving rise to a black blood image when a gradient-echo sequence is used [119]. With this method, the myocardium will appear more homogeneous and have greater border definition than it does when the traditional bright-blood sequence is used. He and colleagues [117, 118] used this optimized black-blood preparation gradient-echo sequence so that the T_2* value could be obtained by using a monoexponential model fit ($SI = ke^{-TE/T2^*}$; where SI = signal intensity, k = constant, and TE = echo time). In contrast, in certain cases, the bright-blood T_2* value could be better estimated by using either the truncation model or the offset model [118, 119]. These measurements were usually made in a full-thickness region of interest that was placed in the mid-ventricular septal region to avoid susceptibility artifact [118].

In 12 hearts obtained from siderotic cardiomyopathy patients after death or cardiac transplantation for end-stage heart failure, midventricular septal iron concentrations and CMRI measurements of R_2* (calculated as $1/T_2$*) were both highly representative of mean global myocardial iron [120]. The same study also confirmed that iron deposition is higher in the epicardium than in the endocardium; therefore, for T_2* measurements, a large, full-thickness section of the midseptum should be chosen as the region of interest.

Nonischemic Cardiomyopathies

Myocarditis

Myocarditis is defined as inflammation of the myocardium. The presentation of myocarditis can vary from nonspecific symptoms to acute hemodynamic instability and death [121]. It has been reported that in some patients myocarditis can progress to dilated cardiomyopathy [122] or ARVD/C [123]. Myocarditis can be caused by an infection (viral, bacterial, or fungal) or can occur secondary to hypersensitivity or immunological conditions.

In patients with suspected myocarditis, CMRI can be used to evaluate global and regional function; wall thickness and mass; pericardial effusion; myocardial edema, which can be detected by characterizing the tissue in T_2-weighted images; increases in volume of distribution caused by hyperemia and capillary leak, which can be detected by early Gd enhancement (the global relative early enhancement ratio, gRE); and myocardial necrosis and fibrosis, which can be detected by using DE. Table 13.2 outlines the proposed Lake Louise Consensus Criteria for using CMRI for diagnosing myocarditis [92].

In a study of 25 patients with clinically diagnosed myocarditis, the sensitivity, specificity, and diagnostic accuracy were determined for three CMRI sequences: (1) the values for the T_2 signal intensity ratio between myocardium and skeletal muscle were 84, 74, and 79 %, respectively; (2) the values for GRE were 80, 68, and 75 %, respectively; and (3) the values for DE-MRI were 44, 100, and 71 %, respectively. When positive results were obtained by any two of the three sequences in a single patient, the values were 76, 96, and 85 %, respectively [124]. In another study of 42 patients with myocarditis, the T_2 signal intensity ratio was elevated in 57 % of the patients, the GRE was elevated in 31 % of the patients, and DE was present in 64 % of the patients. Furthermore, two of these three criteria were present in 76 % of the patients [125]. The fact that not all patients with myocarditis have DE

Table 13.2 Lake Louise consensus criteria for the diagnosis of myocarditis by cardiovascular magnetic resonance imaging

The presence of two of the three following imaging criteria support the diagnosis of myocarditis in clinically suspected cases:
1. Global or regional signal-intensity (SI) increase in T_2-weighted images[a].
2. Increased global early enhancement ratio between myocardium and skeletal muscle in gadolinium-enhanced T_1-weighted images[b].
3. One or more typical DE-MRI lesions that do not fit a coronary distribution.
Consider repeating CMRI in 1–2 weeks if one of the following applies:
1. Strong clinical suspicion of myocarditis but none of the above-mentioned criteria is present.
2. Only 1 criterion is present.
Supportive findings: pericardial effusion or left ventricular dysfunction.

Modified with permission from Friedrich et al. [92]

[a]Global increase in SI ratio of myocardium/skeletal muscle of ≥2.0

[b]Global increase in SI ratio of myocardium/skeletal muscle of ≥4.0 or absolute myocardial enhancement of ≥45 %

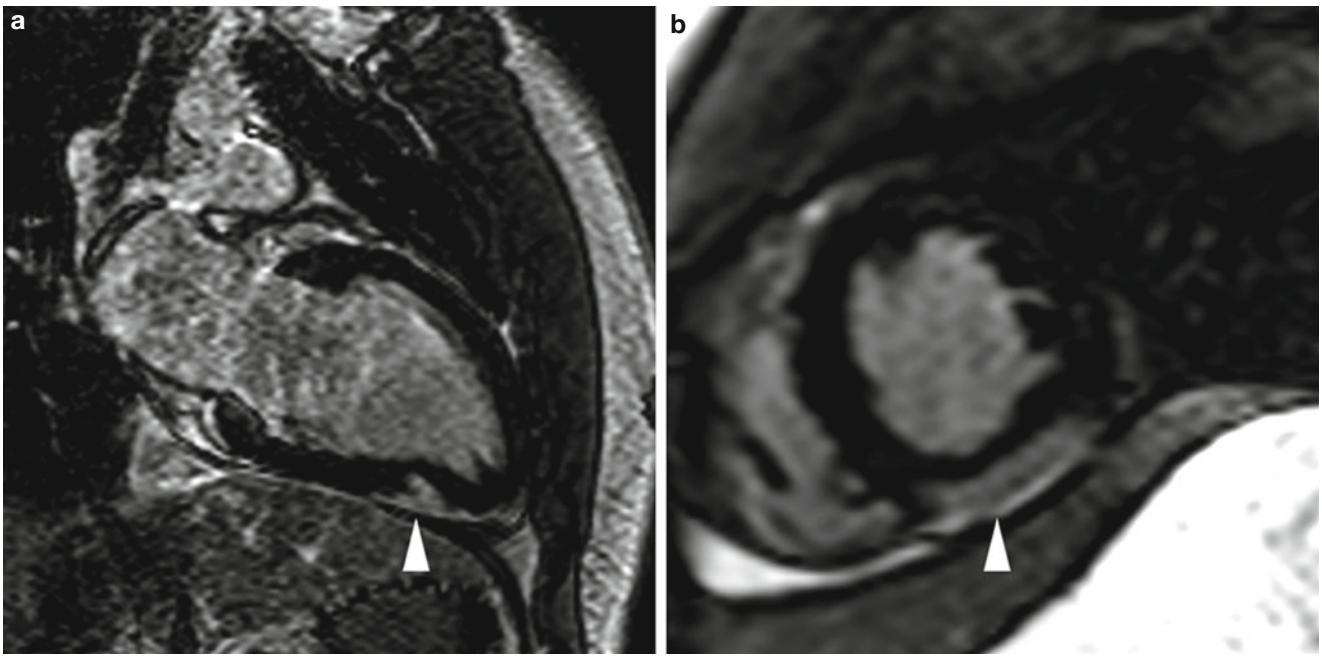

Fig. 13.14 Images from an 18-year-old man who presented with acute chest pain, ST-segment elevation on electrocardiogram, and a mild troponin level increase. Coronary angiography revealed widely patent and normal-appearing coronary arteries. Cardiac magnetic resonance imaging was subsequently performed and showed delayed enhancement (*arrowhead*) in the distal inferior wall (mid-myocardial and epicardial), suggesting a diagnosis of acute myocarditis. Images were acquired in (**a**) the two-chamber orientation and (**b**) the mid short-axis orientation

probably reflects the inability of DE-MRI to reveal diffuse myocardial changes. In DE-MRI, myocarditic lesions typically affect the lateral free wall and the inferior wall, epicardially or mid-myocardially [124, 126], although multifocal or diffuse distribution has also been reported (Fig. 13.14) [92]. Patients with myocarditis have also been shown to have increases in myocardial ECF by T_1 imaging [127].

In a group of 87 patients with active myocarditis who underwent CMRI and endomyocardial biopsy, the most common findings were parvovirus B19 (56 % of patients), human herpesvirus 6 (18 % of patients), and a combination of both viruses (17 % of patients) [128]. Coxsackie B virus and Epstein-Barr virus were infrequently diagnosed (1 % of patients for each virus). Delayed enhancement was seen in the epicardium of the lateral wall in patients who were found to have parvovirus B19; these patients tended to have a relatively benign clinical course on follow-up evaluation. In contrast, DE was commonly found in the anteroseptal region, intramurally, in patients with human herpesvirus 6; the clinical course of these patients was more variable than that of patients with parvovirus B19. For patients affected by both viruses, DE was present in a large area of the anteroseptum, predominantly mid-myocardially. On follow-up examination, these patients were found to have symptoms of persistent congestive cardiac failure and no significant improvement in LVEF. Significant predictors of an impaired LVEF included the presence of DE in the septum, the amount of DE, the end-diastolic volume at presentation, and combined infection with parvovirus B19 and human herpesvirus 6.

Published studies of the use of CMRI for the diagnosis of myocarditis have several limitations. The study cohorts are generally small, and most of the studies involve single-center experiences. Also, different studies use different imaging sequences and diagnostic criteria. Moreover, only a limited number of reports mention histological confirmation of the diagnosis [92].

Arrhythmogenic Right Ventricular Dysplasia/ Cardiomyopathy

Arrhythmogenic RV dysplasia/cardiomyopathy is a heritable form of cardiomyopathy characterized by fibrofatty replacement that primarily affects the right ventricle. At a later stage, the left ventricle can also be affected, thereby worsening the prognosis. The disease is thought to be caused by dysfunctional desmosomes [129]. In 2010, the original 1994 Task Force criteria for the diagnosis of ARVD/C were modified [130]. The diagnosis is fulfilled by the presence of 2 major criteria, or 1 major plus 2 minor criteria, or 4 minor criteria from different categories. These categories include global or regional dysfunction and structural alterations, tissue characterization of RV myocardium, repolarization abnormalities, depolarization/conduction abnormalities, arrhythmias, and family history. The major and minor CMRI criteria proposed in the updated recommendations include regional RV wall-motion abnormality *and* either impaired RV function or increased indexed end-diastolic volume (Table 13.3) [130, 131], whereas the major and minor criteria previously recommended included global dilation of the right ventricle, reduced RV ejection fraction, regional

Table 13.3 Revised 2010 task-force criteria for the diagnosis of arrhythmogenic right ventricular dysplasia/cardiomyopathy by cardiovascular magnetic resonance imaging

Major	Minor
Regional RV akinesia or dyskinesia or dyssynchronous RV contraction	Regional RV akinesia or dyskinesia or dyssynchronous RV contraction
and one of the following:	*and one of the following*:
Indexed end-diastolic volume to body surface area ≥110 mL/m^2 (male) or ≥100 mL/m^2 (female),	Indexed end-diastolic volume to body surface area ≥100 but <110 mL/m^2 (male) or ≥90 but <100 mL/m^2 (female),
or RV ejection fraction ≤40 %	*or* RV ejection fraction >40 but ≤45 %

Modified with permission from Marcus et al. [130] Please refer to this reference regarding the clinical and electrographic criteria
Definite diagnosis =2 major or 1 major and 2 minor criteria or 4 minor criteria from different categories; borderline =1 major and 1 minor or 3 minor criteria from different categories; possible diagnosis =1 major or 2 minor criteria from different categories
RV right ventricular

wall-motion abnormalities (including localized RV aneurysms), and segmental RV dilation.

With the use of a state-of-the-art SSFP sequence, CMRI is inherently suited for the detailed evaluation of wall-motion abnormalities and global RV function, and this method has high temporal resolution and relatively high spatial resolution in comparison with other noninvasive imaging modalities [1]. Quantitative values obtained by means of CMRI are useful for both diagnosis and follow-up evaluation. Imaging of the right ventricle remains challenging because of the limited wall-thickness. The presence of significant ventricular ectopy and tachyarrhythmia also affects accurate ECG-gating. In the proposed 2010 criteria, tissue characterization of the RV free wall is accomplished by endomyocardial biopsy (which is considered the gold standard), not by CMRI [130]. However, as described in the section "Imaging techniques" of this chapter, several CMRI sequences are designed specifically to evaluate fatty and fibrous replacement of the right ventricle. The presence of fat in the right ventricle is not itself specific for ARVD/C, because this finding is commonly associated with aging [132].

To evaluate the presence of fat in the RV myocardium, the typical imaging protocol includes T_1- and T_2-weighted turbo spin echo sequences, with and without fat saturation; images are acquired in both the axial-oblique orientation (parallel to the RV free wall) and the transverse/axial orientation. With the routine use of phased-array surface MRI coils for cardiac imaging, rather than the body coil, the anterior coils can be used alone in order to avoid wrap-around artifacts. In addition, to minimize signal interference and improve image quality, a saturation band can be applied to the anterior chest wall. Fatty infiltration occurs predominately at the epicardial border and extends toward the endocardium in finger-like projections [133]. The LV free wall and the interventricular septum can also be affected. In addition to the technique described above, the multi-echo Dixon technique has also been used to evaluate fatty infiltration [105].

For the accurate quantitative analysis of LV and RV function, high-spatial-resolution cine imaging is performed in the axial-oblique and short-axis orientations by using the state-of-the-art SSFP sequence, which provides high contrast between blood and myocardium. The areas frequently affected by ARVD/C include the RV inflow tract, RV outflow tract, and RV apex; these regions are known as the "triangle of dysplasia" [134]. Patients with ARVD/C may also have heavy trabeculation and dilation of the RV outflow tract (in comparison to the LV outflow tract) [135]; these findings are shown well by SSFP imaging. In patients with ARVD/C, the RV free wall can be thinned and can have a bulging or scalloped appearance, suggesting aneurysmal dilation. In a study of familial ARVD/C, 38 family members of patients who had been diagnosed with ARVD/C and a desmosome mutation underwent genetic testing and CMRI. Of the 25 family members who also had a desmosome mutation, 15 (60 %) of them had RV free wall crinkling that worsened during systole, known as the "accordion" sign, and 8 (32 %) of them reported having cardiac symptoms [136].

When the RV myocardium is imaged, DE-MRI is performed approximately 10–15 min after 0.1–0.2 mmol/kg of Gd is administered [137]. Because the right ventricle is a thin-walled structure, we at our institution commonly acquire DE-MRI images both in systole (the shortest trigger-delay the scanner would allow) and in traditional mid-diastole to optimize visualization of the RV myocardium; in our experience, acquiring the image during systole does not result in significant motion artifact. In addition, because the RV myocardium is much thinner than the LV myocardium, the spatial resolution of the DE-MRI sequence has to be optimized for the evaluation of fibrosis replacement in order to reduce partial volume effects; this potentially increases the imaging time and breathing artifact. The inversion time that should be used for the DE-MRI sequence is the same for both the left and right ventricles [138]. In a study by Tandri and colleagues [137], the presence of DE was highly correlated with the existence of fibrofatty changes in endomyocardial biopsies and inducible ventricular tachycardia, as revealed by electrophysiologic testing. In addition, an increasing amount of DE was found to be correlated with a reduction in the RV ejection fraction and an increase in the RV end-diastolic volume. Figure 13.15 shows the results for a patient with ARVD/C.

Hypertrophic Cardiomyopathy

Hypertrophic cardiomyopathy is a genetic disorder of the myocardium that affects 1 in 500 people and is the most

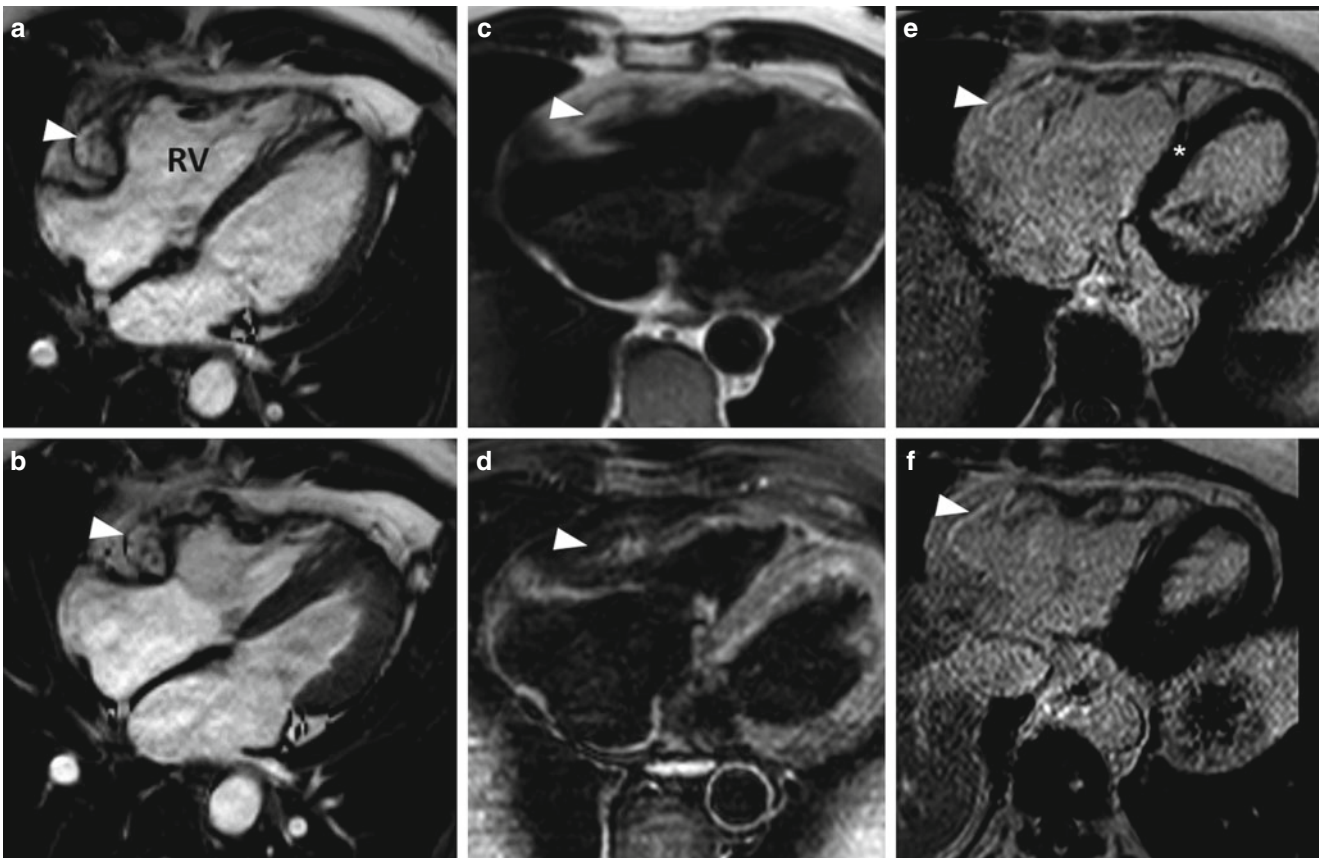

Fig. 13.15 Images from a 58-year-old man with ventricular tachycardia. Images taken during (**a**) end-diastole and (**b**) end-systole show aneurysmal dilation (*arrowheads*) in the basal third of the right ventricle (*RV*). A fat saturation sequence was used to identify fat in the right ventricular myocardium. Double-inversion turbo spin echo images of the right ventricle (**c**) without and (**d**) with fat saturation sequence show signal reduction in the right ventricular myocardium after the fat saturation sequence was applied (*arrowhead*). Delayed-enhancement magnetic resonance imaging showed hyperenhancement in the area where the aneurysmal dilation was present in the right ventricle (**e** and **f** show this dilation at two different levels of the ventricle), indicating fibrous replacement (*arrowheads*). There was moderate right ventricular systolic dysfunction, indicated by a global ejection fraction of approximately 33 %. The imaging results suggested a diagnosis of arrhythmogenic right ventricular dysplasia

common cause of sudden death in youth [139]. Surface echocardiography is the first-line imaging modality for HCM because it is patient friendly and provides information about both systolic and diastolic function and the degree of LV outflow tract (LVOT) obstruction at rest and during provocation maneuvers. However, CMRI can often provide a more precise evaluation of the extent and distribution of hypertrophy. In addition, CMRI with a combination of phase-contrast imaging and ventricular volumetric assessment can be used to ascertain other important aspects of HCM such as LVOT obstruction and the degree of associated mitral regurgitation. Recent reports indicate that DE-MRI can also provide important prognostic information concerning patients with HCM.

Hypertrophic cardiomyopathy is typically diagnosed when the patient has unexplained hypertrophy and an LV wall thickness of $\geq$15 mm with nondilated ventricular chambers [140]. One advantage of CMRI in the context of HCM diagnosis is the ability to image in any plane with no foreshortening or echo dropout, which is especially helpful for visualizing the LV apex. Furthermore, CMRI can accurately quantify LV mass without requiring any geometric assumptions [1, 3]. In a study that compared the diagnostic abilities of CMRI and echocardiography in HCM patients, echocardiography underestimated the maximal LV wall thickness in 10 % of the patients when compared to CMRI (24 ± 3 mm vs 32 ± 1 mm, respectively), and CMRI measurements of the basal anterolateral wall were higher than those taken by echocardiography (17 ± 8 vs 13 ± 6 mm, respectively) [141]. In a study of 333 consecutive HCM patients, CMRI showed that 77 % of the patients had hypertrophy in both the basal anterior wall and the adjacent basal septum [142]. In addition, 12 % of patients had hypertrophy localized in the apex, inferoseptum, or anterolateral wall; this hypertrophy was underestimated or not detected by echocardiography [142]. There are several variants of HCM: asymmetric septal HCM, with and without obstruction; symmetric/concentric HCM;

apical HCM (Yamaguchi's disease); mid-ventricular HCM; mass-like HCM; and noncontiguous HCM [143].

Our institution was among the first to describe the use of DE-MRI in the evaluation of HCM [144]. Delayed enhancement is present in 75–80 % of patients with HCM. Potential causes of HCM include plexiform fibrosis, expanded interstitial spaces, and replacement fibrosis due to underlying ischemia (Fig. 13.16) [64, 145–147]. The presence of DE has been shown to correlate with increased wall thickness [142, 148, 149] and regional wall-motion abnormalities [148].

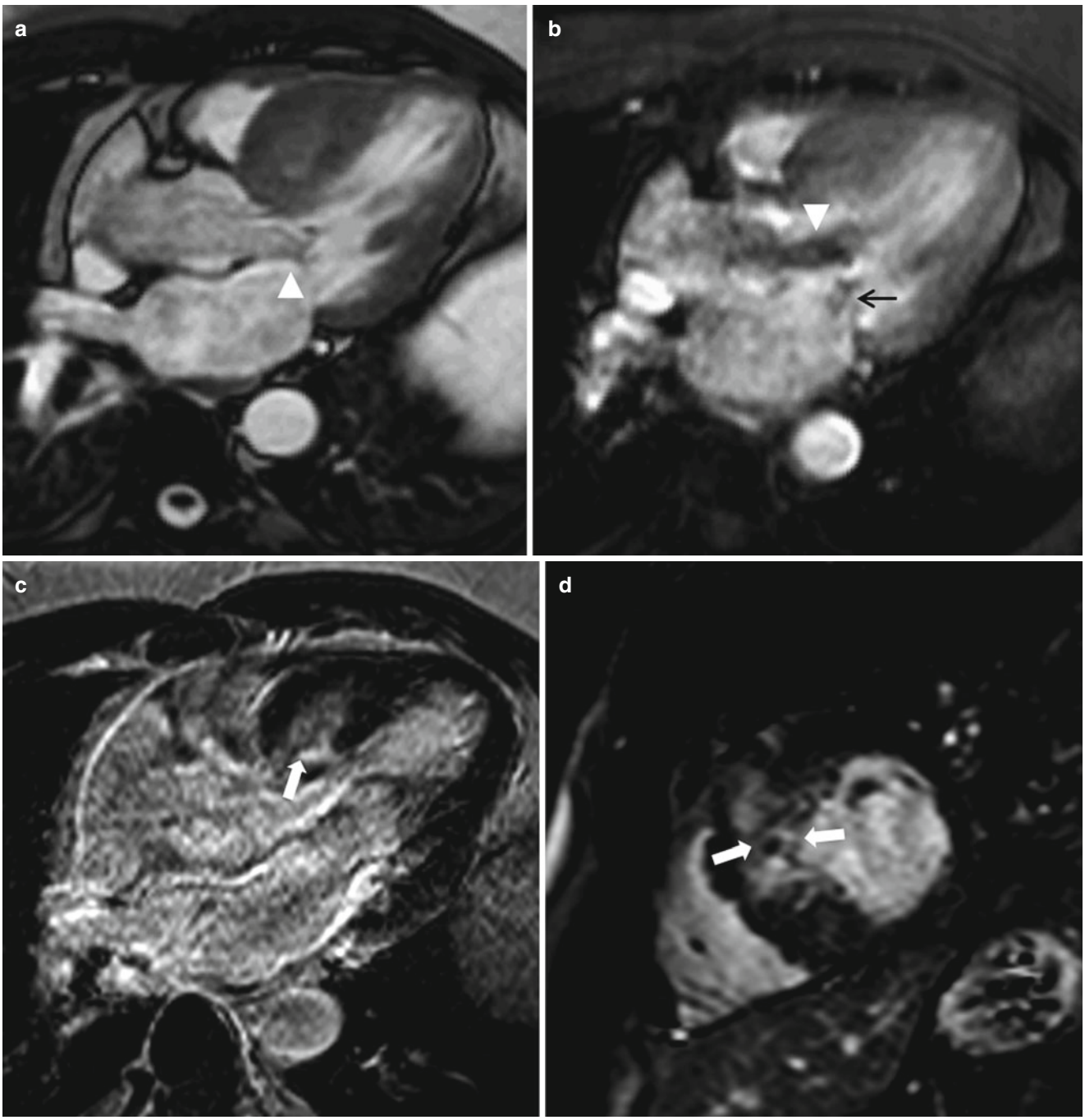

Fig. 13.16 Images from a 58-year-old man who had hypertrophic cardiomyopathy. (**a**) Image acquired by cine gradient echo steady-state free precession in the left ventricular outflow orientation showing systolic anterior motion of the anterior mitral valve leaflet (*arrowhead*). Note that the ventricular septum is hypertrophied; the maximum thickness during end-diastole was 3.1 cm (not shown). (**b**) Corresponding image acquired by using gradient echo planar imaging in the same orientation. The image shows turbulence (*arrowhead*), which indicates outflow tract obstruction. In addition, eccentric mitral regurgitation can be seen (*small black arrow*). (**c**) Delayed-enhancement (DE) magnetic resonance imaging (MRI) in the left ventricular outflow tract orientation showing DE in the septum, where most of the hypertrophy was located (*arrow*). (**d**) DE-MRI in the mid-ventricular short-axis orientation showing diffuse DE in the mid-interventricular septum (*arrows*)

From the CMRI findings in a small series of HCM patients, researchers determined that although patterns of DE distribution can be seen at almost any location that does not follow a coronary artery distribution (such as subendocardial, midmyocardial, transmural, and multifocal DE patterns), certain DE patterns, such as RV septal and transseptal, are associated with a high risk of sudden death [145].

In several recent studies, DE-MRI was used to evaluate the risk of future clinical events and mortality in patients with HCM. The annual mortality rate for these patients was reported to be 1–5 % [150]. In a study that followed up 217 consecutive HCM patients for 3.1 ± 1.7 years, 63 % of the patients were found to have DE [149]. Multivariable analysis showed that for every 5 % increase in the amount of DE, there was a 15 % increase in the risk of reaching the combined primary endpoint of cardiovascular death, unplanned cardiovascular hospital admission, sustained ventricular tachycardia or ventricular fibrillation, or appropriate ICD discharge (HR, 1.15; 95 % CI, 1.01–1.30; $P = 0.03$). In addition, the researchers also determined that the probability of having congestive heart failure increases as the amount of DE increases. Another study followed up 220 HCM patients (60 % were asymptomatic, 11 % had chest pain, 21 % had New York Heart Association functional class I/II symptoms, and 8 % had class III symptoms) for a mean period of 3 years. For these patients, the presence of any DE was an independent prognosticator of cardiac death, which included SCD, congestive heart failure, and aborted SCD (HR, 4.81; $P = 0.035$), whereas the presence of one or two traditional clinical predictors of SCD was not clinically significant [151].

In a study that used CMRI and Holter electrocardiographic monitoring, HCM patients with DE were shown to have significantly more premature ventricular complexes, couplets, and nonsustained ventricular tachycardia than HCM patients without DE, and the presence of DE in these patients was an independent predictor of nonsustained ventricular tachycardia (relative risk, 7.3) [152]. Rubinshtein and colleagues [153] followed up 424 HCM patients for 43 ± 14 months. The 239 (56 %) patients with DE on CMRI had more episodes of nonsustained ventricular tachycardia and a higher frequency of ventricular extrasystoles per 24-h period than did the HCM patients without DE. During the study period, SCD occurred in four patients, and appropriate ICD discharge occurred in four other patients; all eight of these events occurred in patients with DE. Nevertheless, the positive predictive value of DE for SCD or ICD discharge in HCM patients with DE was low (3.3 %). In these cases, myocardial fibrosis could be acting as a substrate that promotes reentrant ventricular tachyarrhythmia. Prospective trials are still needed to determine whether using DE-MRI to risk-stratify HCM patients and to determine whether they need ICD implantation would better promote patient survival than using established traditional risk factors, especially as approximately 75–80 % of patients with HCM are reported to have some degree of DE. The presence of DE/fibrosis could contribute to an increase in myocardial stiffness, leading to diastolic dysfunction and symptoms of heart failure, even in patients with normal systolic function. The amount of DE and the rate of DE increase between two CMRI examinations have both been shown to correlate with a worsening New York Heart Association functional class in HCM patients [154].

Hypertrophic cardiomyopathy patients with severe symptoms that are refractory to medical therapy, as well as dynamic LVOT obstruction, associated septal hypertrophy, and systolic anterior motion of the mitral valve leaflet, can be considered for a surgical myectomy or, possibly, alcohol septal ablation (ASA) [140]. Figure 13.17 shows the DE-MRI results 2 days after ASA. Delayed-enhancement CMRI is inherently suited to evaluating the extent of ASA. If imaged early, patients with ASA are invariably found to have MO. At the same time, patients can be assessed for the presence or absence of a residual LVOT gradient and systolic anterior motion of the anterior mitral valve leaflet. In a study that compared the long-term outcomes of 91 consecutive HCM patients who underwent ASA with the outcomes of 40 HCM patients who underwent a traditional septal myectomy (mean follow-up period, 5.4 years), the patients who underwent ASA were found to have lower 1-, 5-, and 8-year survival rates. Furthermore, in multivariable analysis, ASA was found to be an independent predictor of the composite endpoint of cardiac death and aborted SCD (HR, 6.1; 95 % CI, 1.4–27.1; $P = 0.02$) [155]. In a similar study, however, Sorajja and colleagues [156] found no apparent differences in the survival rate among patients who underwent ASA, individuals in a comparable general population, or age- and gender-matched patients who underwent a myectomy.

Sarcoidosis

Sarcoidosis is an inflammatory disease characterized by the formation of noncaseating granulomas, which can form in multiple organs. The prevalence of cardiac sarcoidosis varies among reports but could be as high as 50 % in the United States [157, 158]. In 13–50 % of cases, sarcoidosis-related death may be cardiac in origin [159, 160], and SCD may account for to 65 % of the deaths that result from cardiac sarcoidosis [161].

Cardiac MRI can be used to detect several morphological abnormalities present in patients with cardiac sarcoidosis [162]. During acute inflammation, T_2-weighted double-inversion spin echo images reveal focal areas of high signal intensity, with and without myocardial thickening. Cine CMRI can be used to detect regional wall-motion abnormalities in locations that have sarcoid infiltration. In advanced cases, focal myocardial thinning and even focal aneurysmal

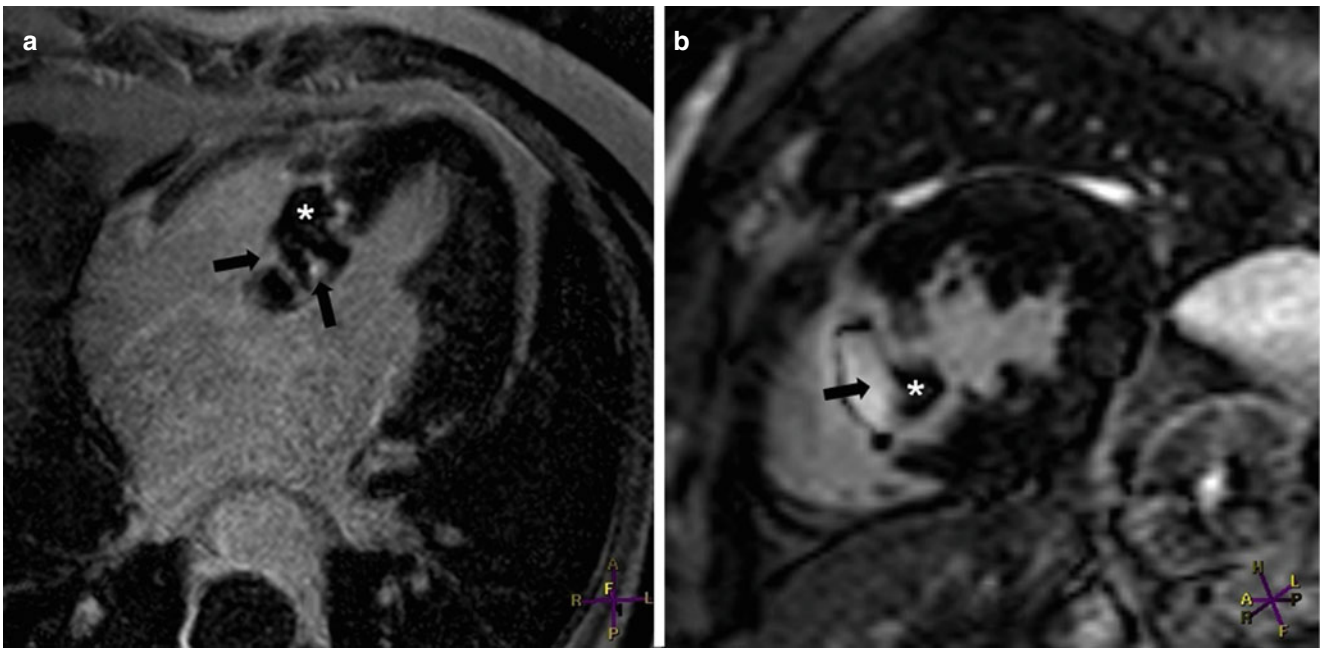

Fig. 13.17 Images from a 53-year-old woman who had symptomatic asymmetric hypertrophic cardiomyopathy. Two days after alcohol septal ablation, delayed enhancement (DE)-magnetic resonance imaging was performed in (**a**) the four-chamber orientation and (**b**) the mid-left ventricular short-axis orientation. The alcohol ablation caused transmural DE (*black arrows*) in the basal half of the interventricular septum. The "islands" of low signal intensity (*white asterisks*) represent microvascular obstruction

dilation have been detected, especially in the basal septum. In patients with pulmonary involvement, pulmonary hypertension can occur; the associated CMRI findings can include enlarged pulmonary arteries, RV dilation, and hypertrophy. Furthermore, the findings of mediastinal and hilar adenopathy in axial spin and gradient-echo images may suggest pulmonary sarcoidosis.

Many authors have described the use of DE-MRI for evaluating patients with suspected or confirmed cardiac sarcoidosis [163–167]. This condition has a predilection for the interventricular septum, especially the basal septum [163, 167]; however, DE may be present in almost any myocardial segment [165]. Delayed enhancement may be mid-myocardial, perhaps extending into the subepicardium or subendocardium, or may be transmural, possibly extending into the adjacent right ventricle. In addition, DE may be multifocal (Fig. 13.18) [163, 165, 167].

Using the guidelines provided by the Japanese Ministry of Health and Welfare as the standard for diagnosing cardiac sarcoidosis, the sensitivity and specificity of CMRI in the diagnosis of this condition were found to be 100 and 78 % (n = 58), respectively, by Smedema and colleagues [165] and 75 and 77 % (n = 21), respectively, by Ohira and colleagues [164]. Patients in both studies had documented extravascular sarcoidosis, and they presented for evaluation of suspected cardiac sarcoidosis. The study by Smedema and colleagues did not require endomyocardial biopsy, and the criteria for diagnosis of cardiac sarcoidosis by CMRI included a combination of wall-motion abnormalities and DE. In the study by Ohira and colleagues, only two patients underwent endomyocardial biopsy, and the criteria for diagnosing cardiac sarcoidosis by CMRI included an increased signal intensity in T_2-weighted imaging and/or the presence of DE. In another study in which DE-MRI was used to evaluate ten patients with cardiac sarcoidosis (diagnosed by either clinical criteria [nine patients] or biopsy [one patient]), the sensitivity of DE-MRI was 100 %; four of the ten patients also had regional wall-motion abnormalities. In addition, these patients underwent ^{201}Tl and ^{67}Ga scintigraphy; the detection rates for these techniques were only 50 and 20 %, respectively [166]. All the above-mentioned studies had the same limitations: a small sample size and few histologically confirmed cases of cardiac sarcoidosis.

Patel and colleagues [167] evaluated the ability of DE-MRI to identify cardiac involvement in 81 patients with biopsy-confirmed extracardiac sarcoidosis (biopsy specimens were all obtained from the RV side of the interventricular septum). Endomyocardial biopsy or autopsy results for 15 patients (19 %) revealed histologic evidence of cardiac sarcoidosis in four patients, all of whom also had DE. Of the remaining 11 patients whose pathology findings were negative for cardiac sarcoidosis, six patients (55 %) had DE. The DE was present in the left ventricle, not in the right ventricle, highlighting the possibility that a sampling error might have occurred during the biopsy. In patients with DE, the event rate (all-cause mortality, symptomatic bradycardia, or

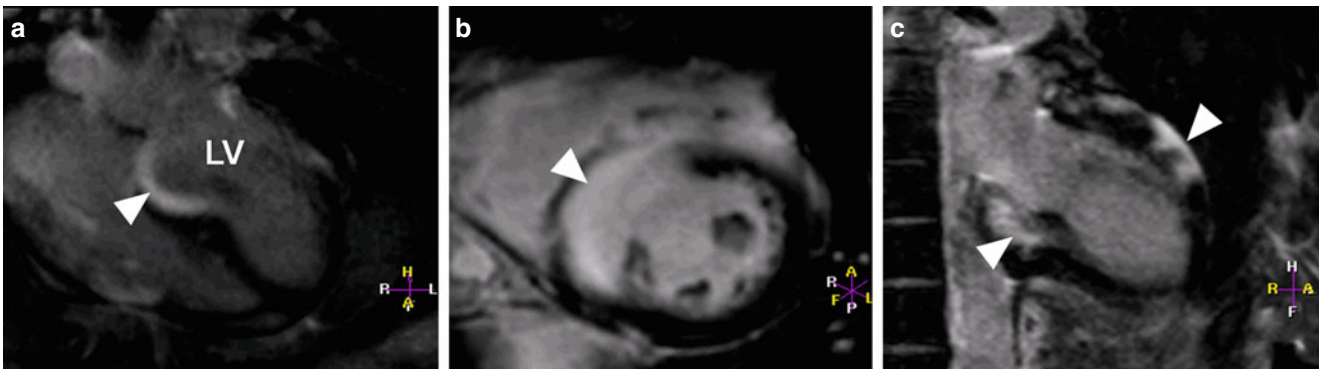

Fig. 13.18 Images from a 23-year-old woman who had pulmonary sarcoidosis and presented with ventricular tachycardia. Angiography, performed 1 week earlier, showed no evidence of coronary artery obstruction. Aneurysmal dilation was seen in the basal interventricular septum when images were acquired in (**a**) the four-chamber orientation and (**b**) the mid left ventricular short-axis orientation. Near-transmural delayed enhancement (DE) (*arrowheads*) can be seen in both (**a**) and (**b**). The image acquired in the two-chamber orientation (**c**) revealed DE extending to the inferior wall and involving the anterior epicardial wall. *LV* left ventricle

ventricular tachyarrhythmia) and the cardiac death rate were, respectively, 9 and 11.5 times higher than in patients without DE [167]. Because of the limited number of adverse events, larger prospective studies should be conducted to confirm whether CMRI and DE-MRI could be used to risk-stratify patients with cardiac sarcoidosis.

Left Ventricular Noncompaction

Left ventricular noncompaction (LVNC) is characterized by excessive and prominent trabeculations with deep recesses that communicate with the ventricular cavity but not with the coronary circulation [168]. This condition is denoted by many different names, including spongiform cardiomyopathy, honeycombed myocardium, LV hypertrabeculation, and isolated LV abnormal trabeculation. It may have been mentioned as early as the 1920s [169], and it is increasingly being described in the current literature, probably because of technological advances in noninvasive imaging modalities.

The exact etiology of LVNC is unknown. Many authors regard LVNC to be a developmental abnormality. Usually, during the second month of embryogenesis, the trabecular meshwork that constitutes the fetal myocardium undergoes intrauterine compaction. In LVNC, however, this compaction is believed to be arrested, resulting in the characteristic thin, compacted epicardial layer with an overlying noncompacted layer of trabeculations [170]. During normal embryogenesis, the trabecular layer of the developing LV myocardium is known to compact from the base to the apex, from the epicardium to the endocardium, and from the septal wall to the lateral wall [171]; this process explains the typical location of LVNC, as shown by CMRI (see below). Some authors have proposed that LVNC may be due to impaired myocardial growth, may represent an adaptation to different hemodynamic conditions, or may result from metabolic defects [172]. Although the American Heart Association classifies LVNC as a primary, genetically determined cardiomyopathy [173], the World Health Organization and the European Society of Cardiology regard LVNC as an unclassified cardiomyopathy [22, 23].

Left ventricular noncompaction is commonly associated with congenital heart disease. In a series of 202 patients who fulfilled the imaging criteria for LVNC, 24 patients also had congenital heart disease. Of these 24 patients, 11 had LVOT abnormalities (uni- or bicuspid aortic valve, aortic coarctation, aortic hypoplasia, or subaortic stenosis), 6 had Ebstein anomaly, and 2 had tetralogy of Fallot. Conversely, when the authors reviewed the records of patients with different congenital heart diseases at the same institution, they found that LVNC was most prevalent in patients with Ebstein anomaly (15 %; 6 of 40 patients), followed by coarctation of the aorta (3 %; 2 of 60 patients) and tetralogy of Fallot (2 %; 3 of 129 patients) [174]. The current discussion will be limited to patients who have LVNC without associated cardiac abnormalities.

Despite the increased diagnosis of LVNC by state-of-the-art noninvasive imaging, there is currently no consensus regarding the criteria to use for diagnosing LVNC by CMRI [175–177] or echocardiography [168, 178–180]. Because of the inherently high contrast-to-noise ratio, the state-of-the-art imaging sequence SSFP can be used to visualize the myocardial trabeculation and the blood pool present in LVNC patients. This approach offers high spatial and temporal resolution (Fig. 13.19). Furthermore, because no geometric assumptions are necessary, this sequence can produce accurate and reproducible LV quantitative data, including LV volumes and cardiac mass. Two echocardiographic reports have indicated that LVNC commonly involves the apical segment (the entire apex was regarded as 1 segment) [168, 181]. Furthermore, in correctly performed CMRI, there should be no ventricular foreshortening; this is particularly important in the detection of LV thrombus, a well-described complication in symptomatic LVNC with impaired LV systolic function. Black-blood imaging with the double-inversion recovery sequence can help detect abnormal areas with increased tra-

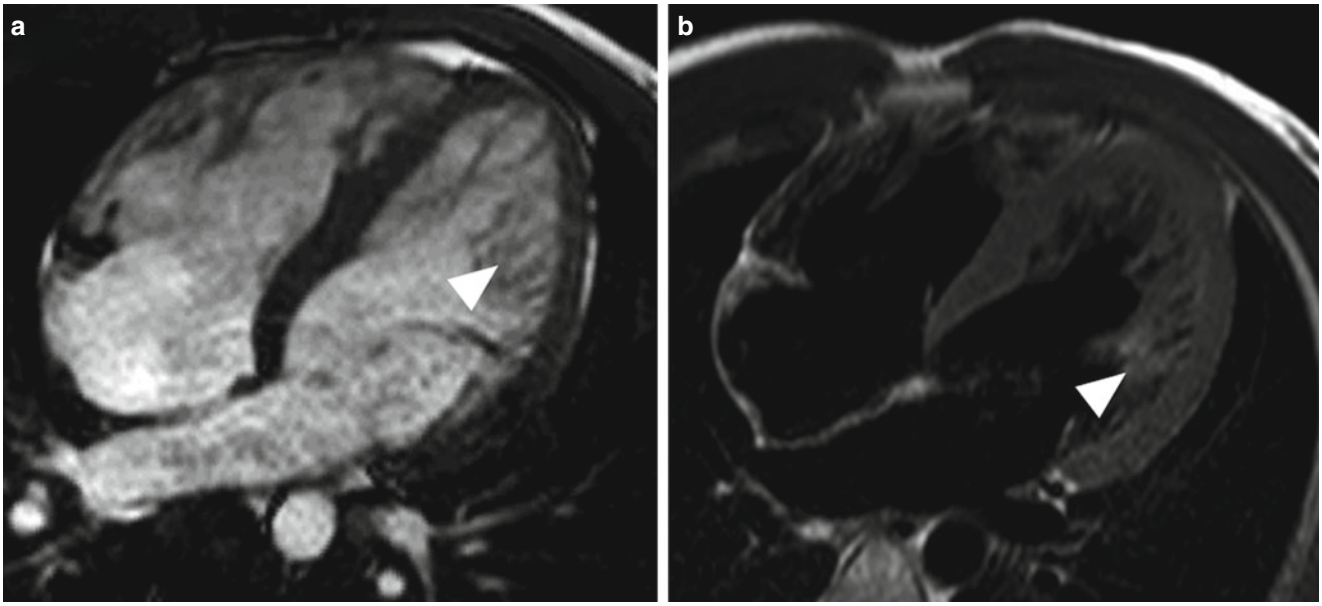

Fig. 13.19 Images from a 28-year-old man who had left ventricular noncompaction. A significant increase in trabeculation in the distal third of the left ventricle (*arrowhead*) can be seen in (**a**) a cine gradient echo image acquired by steady-state free precession in the four-chamber orientation and (**b**) the corresponding double-inversion recovery T_2-weighted spin-echo image

Table 13.4 Surface echocardiographic criteria commonly used to diagnose left ventricular noncompaction

Chin et al. [178]	Jenni et al. [168]	Stollberger et al. [180]
Ratio of X/Y ≤0.5, where X is the distance between the epicardial surface and the trough of the trabeculation and Y is the distance between the peak of trabeculation and the epicardial surface. Measurements taken during end-diastole at the level of the mitral valve and the papillary muscles (parasternal long-axis view) and at the apex (apical 4-chamber or subxiphoid views).	Markedly thickened LV wall that has two layers (NC and C). NC/C ratio of >2 at end-systole in the parasternal short-axis view (basal, mid, and apical). Color Doppler evidence of deep intertrabecular recesses filled with blood. Hypokinesia of the affected/ adjacent segments. Prominent trabecular meshwork in the LV apex or midventricular segments of the inferior and lateral wall. More than three trabeculations present, as defined by Stollberger and colleagues [180]. No other cardiac abnormalities present.	Three trabeculations protruding from the left ventricle, apically to the papillary muscles, visible in one imaging plane. Color Doppler evidence of deep intertrabecular recesses filled with blood.

LV left ventricular, *NC* noncompacted, *C* compacted

beculations by revealing slow flow. Although surface echocardiography is the first-line noninvasive imaging modality, CMRI more completely delineates the extent of trabeculation in patients with LVNC [182]. In addition, some findings that can mimic LVNC can be easily distinguished by CMRI; examples include false tendons, abnormal insertion of papillary muscles, and aberrant bands.

Table 13.4 summarizes the criteria commonly used for the diagnosis of noncompaction by means of surface echocardiography [168, 178, 180], and Table 13.5 presents the criteria used in recent publications to diagnose LVNC by means of CMRI [175–177]. In a CMRI study of healthy volunteers between 20 and 80 years old, the mean trabecular:compacted layer ratio during end-diastole was shown to be less than 1 in all cardiac segments except 16 (the apical lateral wall, 1.19) [183].

Using CMRI, Petersen and colleagues [175] noted that trabeculations occur most frequently in the apex and in the distal third of the left ventricle, followed by the mid-anterior, lateral, and inferior walls. Similarly, Grothoff and colleagues [177] noted that trabeculations are most frequently located at the apex and in the distal third of the left ventricle, followed by the mid-inferior, lateral, and mid-anterior walls. The basal septum is usually not involved.

Many investigators have observed DE in LVNC patients [184–189], although the location and extent of DE varies by report; DE can be subendocardial, mid-myocardial, subepicardial, transmural, or a combination of these, and it can affect both normal segments of the heart and areas with noncompaction [186, 188, 189]. There appears to be no association between DE and noncompaction of the LV segment [189]. In a case report regarding a patient who underwent

Table 13.5 Cardiovascular magnetic resonance criteria used to diagnose left ventricular noncompaction

Petersen et al. [175]	Jacquier et al. [176]	Grothoff et al. [177]
NC/C ratio of >2.3 during end-diastole[a] Images acquired in three views: vertical long-axis, horizontal long-axis, and parasternal long-axis The apex (segment 17) is excluded from analysis because the myocardium is thinner at this level and prominent trabeculation is commonly seen in the apex of normal subjects	Trabeculated mass >20 % of global LV mass[b] Papillary muscles are included in the myocardial mass measurement (compacted mass) Trabeculation is defined as myocardium protruding from the LV wall into the LV cavity Trabeculated mass = global LV mass (mass including papillary muscles and trabeculation) – compacted mass	Percentage of noncompacted myocardial mass >25 %[c] Total noncompacted myocardial mass index >15 g/m^2 [c] NC/C ratio ≥3 in at least 1 of the following segments: 1–3 or 7–16[c] NC/C ratio ≥2 in segments 4–6[c]

NC noncompacted, *C* compacted, *LV* left ventricular

[a]When this single criterion is used, the sensitivity, specificity, positive predictive value, and negative predictive value are 86, 99, 75, and 99 %, respectively

[b]When this single criterion is used, the sensitivity and specificity are both 94 %

[c]When three of the four criteria are present, the sensitivity, specificity, positive predictive value, and negative predictive value are 92, 100, 100, and 96 %, respectively

cardiac transplantation because of LVNC with severe congestive cardiac failure, the near-transmural DE seen in the interventricular septum (free of trabeculations) corresponded to the presence of fibrosis, as shown by histologic analysis. Furthermore, diffuse DE was seen in the free wall of the left ventricle and in the associated noncompacted area; histologic examination revealed fibrosis in the trabeculated areas and mucoid degeneration in the endocardium [190]. In an original article by Jenni and colleagues [168], the hearts of seven LVNC patients were studied anatomically, either postmortem or after heart transplantation; none of the seven patients had other cardiac abnormalities. Histologic examination revealed ischemic lesions in the thickened endocardium and in the prominent trabeculations. Interstitial fibrosis was also detected in six of the seven patients.

The exact mechanism of DE in LVNC is largely unknown. In LVNC patients, diminished coronary flow reserve has been observed in noncompacted and compacted segments on PET evaluation, suggesting microvascular dysfunction [191]. Similar observations have been made in children with LVNC [192]. The reduction in flow reserve and the altered myocardial perfusion could be due to failure of the coronary microcirculation to grow in conjunction with the increasing LV mass [185]. The above-mentioned mechanisms could potentially contribute to myocardial ischemia and, ultimately, scarring. Microvascular dysfunction could lead to contractile impairment.

In a study by Kohli and associates [193], echocardiographic results from patients with LV systolic dysfunction were compared with results from 60 healthy volunteers (30 white and 30 black). Five of the volunteers (4 black and 1 white) fulfilled 1 or more of the echocardiographic criteria for LVNC (as listed in Table 13.4), raising the question of whether the imaging criteria for LVNC are too sensitive. A similar observation was made in a recent CMRI study of 323 participants in the Multi-Ethnic Study of Atherosclerosis who had no history of LVNC, cardiac disease, or hypertension and who showed no DE on CMRI examination [194]. Of these 323 participants, 140 (43 %) had a noncompaction:compaction (NC:C) ratio of >2.3 in at least 1 region, and 20 (6 %) had an NC:C ratio of >2.3 in >2 regions. An NC:C ratio of >2.3 was most frequently located in the apical anterior, apical septal, and apical lateral wall.

Cardiac Amyloidosis

Cardiac amyloidosis refers to the extracellular deposition of low-molecular-weight, insoluble amyloid fibrils in a β-pleated sheet configuration [195]. There are three common subtypes of amyloidosis: (1) AL amyloidosis, or primary amyloidosis, which is characterized by the accumulation of monoclonal immunoglobulin light chains and has the worst prognosis; (2) ATTR amyloidosis, which can be caused by either a transthyretin gene mutation, leading to hereditary amyloidosis, or by wild-type transthyretin deposits, resulting in senile systemic amyloidosis; and (3) systemic AA amyloidosis, which involves amyloid fibrils that arise from serum amyloid A protein and can complicate chronic inflammatory diseases [195].

The noninvasive-imaging findings that are commonly produced by surface echocardiography in patients with cardiac amyloidosis—such as biventricular hypertrophy, normal or small ventricular size, bi-atrial enlargement, and septal thickening [196]—can also be optimally evaluated by CMRI. A CMRI study by Fattori and colleagues [197] showed that the interatrial septum, right atrial free wall, and RV free wall were significantly thicker in patients with cardiac amyloidosis than in patients with HCM. In addition, approximately half of the patients with cardiac amyloidosis also had pericardial and or pleural effusions.

In a study by Maceira and associates [111], 30 patients who had histologically proven amyloidosis with cardiac involvement, diagnosed predominantly by echocardiographic criteria, were all assessed by late Gd enhancement CMRI. Twenty (69 %) of these patients had global and diffuse subendocardial DE after Gd-chelate administration that was evident in the right and left ventricles. This pattern of

subendocardial DE has also been observed in other studies [198–200]. In Maceira's study [111], the Gd washout from the myocardium and the blood was also faster than normal, probably because of the increased extracellular space and the increased distribution of Gd into the total amyloid load (the use of 0.1 mmol/kg of Gd could also have contributed to this finding). Therefore, the DE-MRI sequence produced similar myocardial and blood T_1 values in patients with amyloidosis, so the blood pool had a persistently low signal intensity, similar to that of the myocardium [111]. At our institution, we have noted that in patients who are subsequently confirmed to have cardiac amyloidosis, the "nulling-time" in the DE-MRI sequence necessary to suppress the myocardial signal is difficult to achieve, resulting in widespread patchy enhancement in the entire myocardium (Fig. 13.20). This finding is consistent with an increase in extracellular space due to amyloid protein deposition in the heart, rather than true myocardial fibrosis [198]. The same observation has been reported by other investigators [198, 201]. In a study of patients with amyloidosis, CMRI was performed in a subset of patients who had histologically proven cardiac sarcoidosis. Abnormal DE was found in 34 of the 35 patients (97 %); 21 of these patients (60 %) had global transmural DE, and 8 (23 %) had global subendocardial DE [198]. The location of DE matched the distribution of interstitial amyloid in the histologic specimens.

Endomyocardial biopsy is considered the gold standard for the diagnosis of cardiac amyloidosis [202]. A series of 33 consecutive patients who had congestive heart failure with a restrictive filling pattern underwent endomyocardial biopsy and a comprehensive CMRI examination [199]. The biopsy confirmed the diagnosis of cardiac amyloidosis in 15 of the patients. In this study, the typical DE pattern for cardiac amyloidosis was circumferential subendocardial with various degrees of extension into the adjacent myocardium. Using endomyocardial biopsy as the standard, the sensitivity,

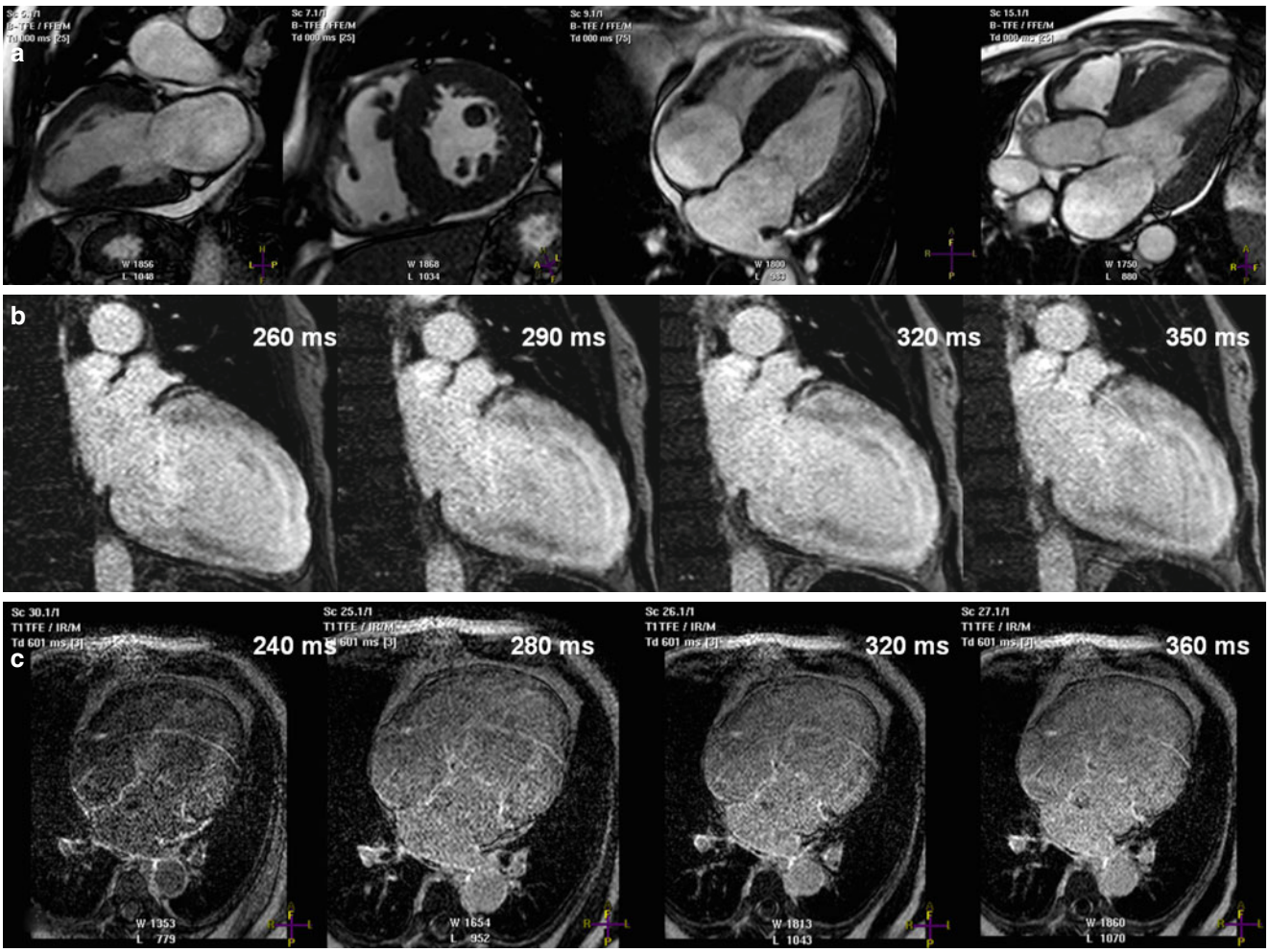

Fig. 13.20 Images from a 68-year-old man who presented with malaise, biventricular failure, and a history of multiple myeloma. The *top row* (**a**) shows still frames acquired by using steady-state free precession in various orientations. They show left ventricular hypertrophy and, possibly, mild right ventricular hypertrophy. The *middle row* (**b**) shows images acquired by using delayed-enhancement magnetic resonance imaging (DE-MRI) in the two-chamber orientation. In these images, the left ventricular myocardium was never well "nulled" at the different inversion times (shown in the *right upper corner*). Similarly, the myocardium was never well nulled in the images on the *bottom row* (**c**), which were acquired by using DE-MRI in the four-chamber orientation. Twelve-lead electrocardiography revealed low voltage in both the chest and limb leads (not shown). Subsequent fat-pad biopsy confirmed the diagnosis of amyloidosis

specificity, positive predictive value, and negative predictive value of DE-MRI were calculated to be 80, 95, 92, and 85 %, respectively [199]. In a recent study by Austin and colleagues [203], a subset of patients with suspected cardiac amyloidosis (38 of 47 patients) underwent endomyocardial biopsy and complete CMRI study, including DE-MRI. The diagnostic utility of DE was compared with that of low-voltage ECG (Carroll's ECG criteria), abnormal deceleration time on Doppler echocardiography (≤150 ms), and the combination of ECG and deceleration-time criteria. The presence of DE had the highest diagnostic accuracy of the noninvasive imaging parameters tested. The sensitivity, specificity, positive predictive value, and negative predictive value of DE-MRI, using endomyocardial biopsy as the standard, were 88, 90, 88, and 90 %, respectively. These results are in agreement with those published by Vogelsberg and colleagues [199].

Besides using DE-MRI to evaluate suspected cardiac amyloidosis, various investigators have also relied on measured T_1 times and estimates of ECF due to extracellular space expansion to diagnose cardiac amyloidosis [111, 200, 204, 205]. Krombach and colleagues [200], using a 1.5 T MRI scanner, found that a patient with biopsy-proven cardiac amyloidosis had substantially higher myocardial T_1 times (1,387 ± 63 ms) than did a group of individuals without known myocardial disease (1,083 ± 33 ms). In another study, the T_1 times were longer in 19 consecutive patients with cardiac amyloidosis than in ten healthy control subjects (1,340 ± 81 vs 1,146 ± 71 ms; P <0.0001) [200]. A T_1 time of 1,273 ms was determined to be the best discriminatory value for diagnosing cardiac amyloidosis by ROC analysis, with a sensitivity of 84 % and a specificity of 100 %. Using a 3 T MRI scanner, Mongeon and colleagues [204] quantified myocardial ECF in 14 patients with biopsy-proven cardiac amyloidosis. The median ECF in amyloid patients was 0.49, whereas the median ECF in healthy subjects was 0.24 (P = 0.0001). The increase in myocardial ECF (reflecting the expansion of the extracellular matrix) is due to either amyloid protein accumulation in the interstitial space or fibrosis, both of which can lead to an increase in Gd uptake [111, 204]. In patients with cardiac amyloidosis, obtaining high-quality DE images could prove to be technically challenging because of the rapid myocardial uptake of Gd and the associated difficulty of selecting the correct inversion time for accurate "nulling" of the myocardium. The measurement of myocardial ECF could overcome this difficulty and provide an objective means to quantify the degree of amyloid deposition, fibrosis, or both. Another possible use of the ECF measurement could be disease monitoring after the treatment for amyloidosis has been administered.

Several recent studies have indicated that DE could be an adverse prognosticator for cardiac amyloidosis [203, 206, 207]. In a study by Ruberg and colleagues [206], which involved 28 patients with systemic AL amyloidosis, 19 patients were found to have DE. Although the presence of DE did not predict mortality (during the median follow-up time of 29 months), the amount of DE, expressed as a percentage of the LV mass, was the strongest independent predictor of the B-type natriuretic peptide level when compared to other LV quantitative factors. In another group of patients with AL amyloidosis, 23 (79 %) of the 29 patients who underwent CMRI had DE [207]. After 26 ± 13 months of follow-up, 14 of those 23 DE-positive patients had died, whereas none of the patients without DE had died (P = 0.0061). Potential mechanisms proposed by the authors to account for these adverse outcomes in patients with AL amyloidosis included systolic and diastolic dysfunction, underlying myocardial ischemia with perivascular and interstitial deposition of amyloid proteins, and endothelial dysfunction [207]. Like Ruberg and colleagues, Maceira and associates [208] did not identify DE as a significant predictor of mortality (only a trend was seen); however, the difference between the T_1 values of the subepicardium and subendocardium, as measured 2 min after Gd administration, was able to predict mortality with 85 % accuracy when a threshold value of 23 ms was used. The close T_1 values between the subepicardium and subendocardium probably reflect the underlying myocardial amyloid burden.

Takotsubo (Stress) Cardiomyopathy

Takotsubo cardiomyopathy (TCM), also known as stress cardiomyopathy, has been increasingly recognized as a differential diagnosis of acute coronary syndrome. Patients typically present with chest pain, ECG changes, and mild elevation of cardiac enzymes; these changes are often precipitated by emotional stress in the absence of significant CAD [209–211]. Classically, there is a "balloon-like wall-motion" abnormality that predominately involves the LV apex and the distal left ventricle [212]. However, different subtypes have been described, including "reverse TCM," in which the base of the left ventricle has a wall-motion abnormality and the apex is hyperdynamic; the mid-LV variant, in which the base and apex of the left ventricle are spared; and the localized variant, which affects various segments of the left ventricle [209, 213]. Furthermore, although the left ventricle is usually affected, involvement of the right ventricle has also been well described [214–217]. The Mayo Clinic's diagnostic criteria for TCM, as suggested by Hurst and colleagues [209], are outlined here with modifications: (1) transient wall-motion abnormalities of the LV apex and mid segment that involve more than a single vascular bed (although, as detailed above, wall-motion abnormalities can occur elsewhere), (2) absence of CAD or angiographic evidence of plaque rupture, (3) new ECG changes and elevation of myocardial biomarker levels, and (4) absence of pheochromocytoma and myocarditis.

Various CMRI sequences are helpful in the assessment of TCM. The cine SSFP sequence allows excellent morphological evaluation of both the left and right ventricles, especially the apices, and accurate quantitative assessment of biventricular function. The spin echo sequence with fat saturation can be used to evaluate myocardial edema. In addition, DE-MRI detection of myocardial fibrosis and necrosis is especially important in the differential diagnosis of acute coronary syndrome and TCM.

Eitel and colleagues [217] conducted 1 of the largest studies of TCM, which included 256 patients, 239 (93 %) of whom had CMRI data available. Two hundred seven patients (81 %) were postmenopausal women, 225 patients (88 %) presented with symptoms consistent with acute coronary syndrome, and 182 patients (71 %) had experienced a significant stressful event within the 48 h before presentation. Classical apical ballooning was detected by CMRI in 197 patients (82 %); in 81 patients, both the left and right ventricles were involved. In this study, patients with both RV and LV involvement (suggesting more extensive disease) were older, were hospitalized longer, and had lower LVEFs than patients without RV involvement (43.1 % vs 45.3 %; P <0.001). These findings are similar to those reported by other authors [214, 216]. Eitel and colleagues also detected evidence of myocardial edema in 162 of the 199 patients (81 %) who had dedicated imaging sequences performed; the location of myocardial edema was similar to the distribution of wall-motion abnormalities in the left ventricle. Furthermore, when the signal intensity threshold was limited to between 3 and 5 standard deviations, 22 patients (9 %) were shown to have focal or patchy DE, but the DE was not identified in follow-up CMRI examinations. Patients who were DE-positive tended to have higher cardiac troponin levels at presentation, although no significant difference was noted in the quantitative functional values between the DE-positive and DE-negative groups. Associated CMRI findings included pleural effusion (more often in patients with biventricular involvement), pericardial effusion (more often in patients with myocardial edema), and ventricular thrombus (in four patients) [217].

Myocardial edema has been observed in patients with TCM [217–222]. In T_2-weighted images acquired by CMRI, the majority of TCM patients appear to have an increase in signal intensity with a transmural distribution that corresponds to the location of wall-motion abnormalities [217, 219, 221]. In the study by Eitel and colleagues [217], 158 patients (62 %) underwent follow-up CMRI (median follow-up period, approximately 3 months). A significant reduction in the T_2 ratio (signal intensity of myocardium/signal intensity of skeletal muscle) was noted, indicating an improvement in myocardial edema. Similarly, Neil and colleagues [220] observed a reduction in T_2 signal intensity at the 3-month follow-up CMRI study; however, the signal intensity in patients with TCM was still higher than the signal levels in healthy control subjects. In contrast to the other authors referenced above, Neil and colleagues noted that although the T_2 signal intensity was greater at the apex than at the base (P <0.0001) in patients with typical TCM, these patients still had a higher T_2-signal intensity at the base than did age-matched control subjects [220]. Various mechanisms have been proposed to explain the presence of myocardial edema in TCM patients, including inflammation, transient ischemia, and increased wall stress. In addition, high intraventricular pressure could cause a perfusion abnormality that could subsequently lead to edema [217]. Figure 13.21 shows typical findings from a TCM patient.

It is not clear whether DE is associated with TCM. Some reports indicate that DE is absent in this condition [223, 224], whereas others indicate the opposite [217, 221, 222]. When DE has been detected at presentation, it has always been noted to resolve on follow-up CMRI examinations. Some authors have noted that the DE signal intensity is lower in TCM patients than in MI patients. Furthermore, the distribution of DE in TCM patients has been found to be either focal or patchy and located where wall-motion abnormalities are present [217, 222]. In a study by Rolf and colleagues [222], endomyocardial biopsy and CMRI results from patients with TCM were available from both the acute and recovery phases. The biopsy results revealed no signs of oncotic or apoptotic cell death in the acute phase [222, 225]. The amount of collagen-1, which reflects fibrosis, was significantly higher in DE-positive patients than in patients without DE. During the recovery phase, the amount of collagen-1 returned to normal in parallel with the resolution of DE, suggesting that these findings could represent reactive fibrosis rather than replacement fibrosis [222].

Chagas Disease

Chagas disease is caused by the parasite *Trypanosoma cruzi*. Symptoms are present during the acute phase, which lasts approximately 6–8 weeks. The majority of patients then enter a chronic yet asymptomatic period known as the indeterminate phase. Many years later, certain patients develop chronic symptoms, entering the chronic symptomatic phase. The manifestations of chronic Chagas disease mainly involve the cardiac and digestive systems. The most serious manifestation, Chagas cardiomyopathy, primarily presents as arrhythmia, cardiac failure, and thromboembolism [226].

In the acute phase, the *T. cruzi* organism can be detected by parasitologic tests, whereas in the chronic phase, serologic tests are used to detect antibodies against *T. cruzi* antigens [227]. Cardiac MRI can be used for morphologic evaluation of Chagas cardiomyopathy and for accurate quantitative assessment of the cardiac chambers. In multivariable analysis, left atrial volume, as determined

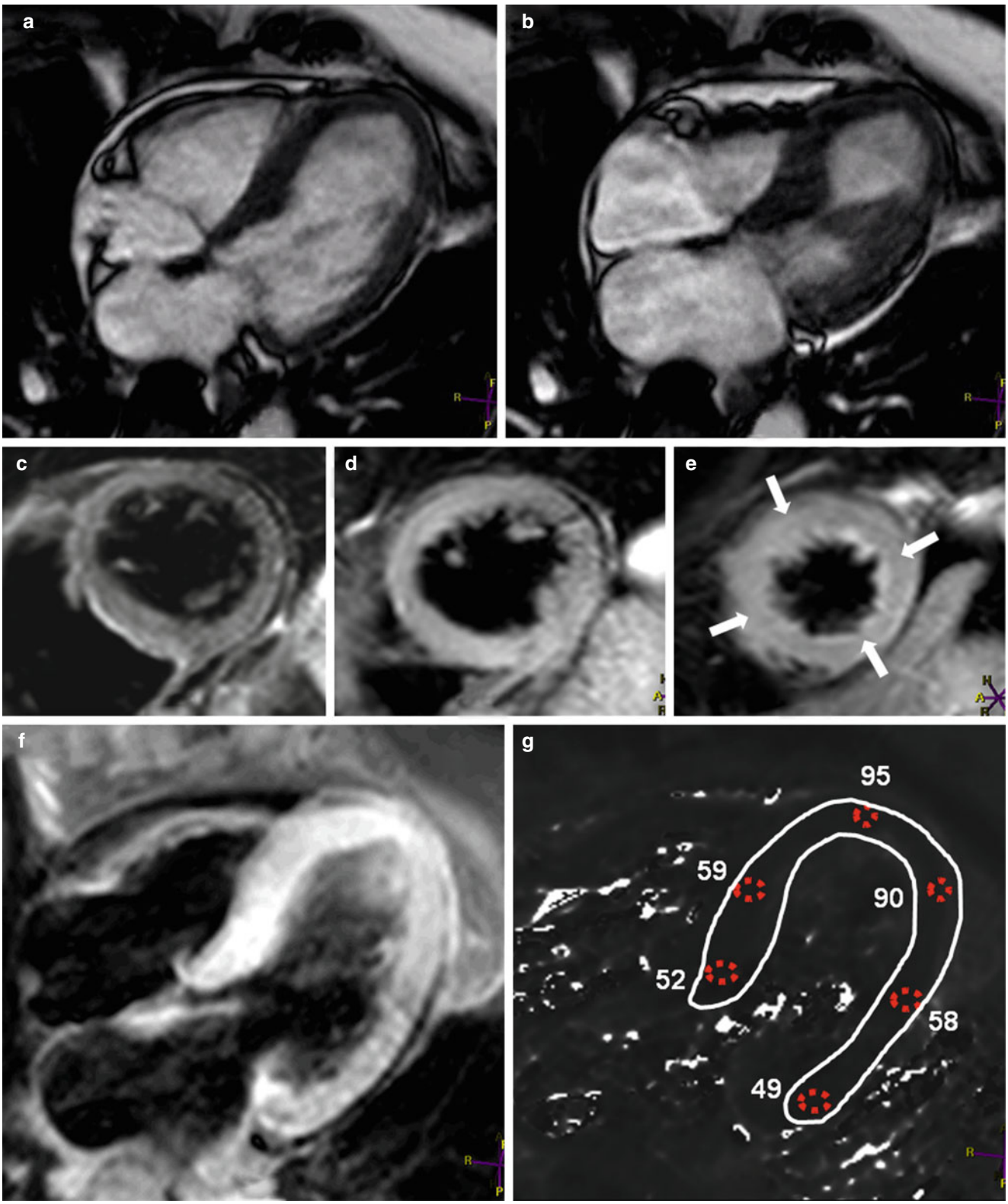

Fig. 13.21 Images from a 48-year-old woman who had acute chest pain. The images were acquired by using steady-state free-precession cine imaging in (**a**) end-diastole and (**b**) end-systole. Note that only the basal 2/3rds of the left ventricle are contracting during systole, which is typical for classical apical ballooning syndrome, also known as Takotsubo syndrome. Double inversion T_2-weighted spin echo images are shown of the basal third (**c**), the middle third (**d**), and the distal third (**e**) of the left ventricle. Note the increased signal intensity in the distal third of the left ventricle (*arrows*). Dedicated T_2-mapping was carried out in the four-chamber orientation (**f**). Results of the T_2 analysis are shown in (**g**). The T_2 values in the distal left ventricle were higher than the patient's normal myocardial T_2 values, which were between 40 and 60 ms. These results confirm the visual assessment and correspond to the wall-motion abnormality. Delayed-enhancement magnetic resonance imaging results were normal (not shown)

echocardiographically, has been shown to be a powerful independent prognosticator for cardiac death or transplantation in patients with Chagas cardiomyopathy (HR, 1.04 per 1-mL/m^2 increase; 95 % CI, 1.018–1.056; P <0.001) [228]. Furthermore, LV systolic dysfunction has consistently been shown to affect the outcome in these patients [226, 229].

A recent CMRI study included 67 patients who were serologically positive for Chagas disease. The patients were divided into three groups: group I (n = 27) had no ECG or echocardiographic abnormalities, group II (n = 19) had only ECG abnormalities, and group III (n = 21) had both ECG and echocardiographic abnormalities [230]. Compared to the other groups, group III had the lowest LVEF, largest end-diastolic and end-systolic volumes, and largest atrial size. In addition, the amount of DE expressed as the percentage of the LV mass was the greatest in group III (12.4 %) versus group I (4.0 %) and group II (3.7 %). Wall-motion abnormalities and DE were more frequently observed in the apical segment and in the inferolateral walls, and the distribution of DE in this cohort was heterogeneous (27 % subendocardial, 14 % midwall, 23 % subepicardial, and 36 % transmural) [230]. Rochitte and colleagues [231] noted similar CMRI findings. In their study, patients with Chagas disease were also divided into three groups: (1) patients with indeterminate disease, (2) those with known Chagas cardiomyopathy, and (3) those with known Chagas cardiomyopathy and a history of ventricular tachycardia. When the three groups were compared, patients with indeterminate disease had the highest LVEF (65.7 ± 7.5 %) and the lowest amount of DE (0.9 ± 2.3 %), expressed as a percentage of the LV mass, whereas patients with Chagas cardiomyopathy and a history of tachycardia had the lowest LVEF (32.3 ± 12.7 %) and the highest amount of DE (25.4 ± 9.8 %), (P <0.001 for both comparisons). Delayed enhancement was predominantly located in the LV apex and in the inferior and inferolateral walls. De Mello and colleagues [232] noted that the relative risk of ventricular tachycardia in patients with Chagas cardiomyopathy was 4.1 when transmural DE was present in two or more segments, whereas the relative risk was 2.8 when the LVEF was ≤40 %.

In patients with Chagas cardiomyopathy, aneurysmal dilation is commonly seen at the apex or at the basal inferolateral wall; this can be seen well by using the state-of-the-art SSFP CMRI sequence. Any associated thrombus can also be easily detected by CMRI [233]. The LV apex (located at the terminal circulation of the left anterior descending [LAD] and right coronary artery [RCA]) and the basal inferolateral wall (located at the terminal circulation of the left circumflex artery and the RCA) are postulated to be the preferential sites of aneurysmal dilation because they may be especially prone to repeated ischemic insults due to chronic myocardial inflammation as various inflammatory mediators and cytokines are released [233].

Anderson-Fabry Disease

Anderson-Fabry disease (AFD) is an X-linked progressive disorder that is caused by a deficiency of the lysosomal enzyme α-galactosidase A, which leads to the accumulation of globotriaosylceramides (glycosphingolipids) [234]. Many organs can be affected, including the heart, kidneys, and brain. Enzyme replacement therapy (agalsidase alfa or beta) can stop the progression of the disease, and early treatment can prevent irreversible organ damage [234]. Cardiac manifestations of AFD include LV and/or RV hypertrophy, atrial dilation, valvular heart disease, conduction abnormalities, and diastolic dysfunction. Eventually, these patients can have congestive cardiac failure, an arrhythmia, or even an MI due to CAD [235].

The echocardiographic findings in AFD can be similar to those in symmetric HCM, making the differential diagnosis difficult. However, using DE-MRI, investigators have identified a DE pattern that appears to be specific to patients with AFD [236, 237]. Specifically, of the 13 patients with AFD who were imaged by De Cobelli and colleagues [236], 10 (77 %) had DE in the basal inferolateral wall (two patients also had DE that extended to the mid inferolateral wall, one patient also had DE in the mid inferior wall, and one patient also had DE in the apical lateral wall) [236, 237]. In a study of AFD patients by Moon and colleagues [237], CMRI revealed DE in half of the 18 males and half of the 8 females; in 92 % of these patients, DE occurred in the basal inferolateral wall. In addition, in both studies described above, the location of DE was mid myocardial, always sparing the subendocardium and the subepicardium. When Imbriaco and colleagues [238] compared normal healthy volunteers to HCM patients and AFD patients, the T_2 relaxation time was longest in the patients with AFD for all myocardial regions (measurements were obtained in the septum, apex, and lateral wall). The median T_2 values in the lateral wall were 52, 68, and 79 ms, respectively (P <0.001). The authors postulated that the prolonged T_2 relaxation time might be related to the myocardial glycolipid deposits. When 11 patients with AFD were treated with agalsidase beta for 45 months, the LV mass, LV wall thickness, and average T_2 relaxation times were significantly reduced after treatment [239]. No significant change in LVEF was noted, but the Mainz Severity Score Index (an objective assessment of the severity of AFD) significantly decreased after treatment. Another study of the effects of enzyme replacement therapy with agalsidase beta resulted in similar CMRI findings, but no change in LV systolic function was observed; however, the New York Heart Association functional class did improve during follow-up observation [240].

Iron Overload Cardiomyopathy

Iron overload cardiomyopathy (IOC) is defined as a systolic or diastolic dysfunction due to increased myocardial iron

deposition [241]. In patients with iron overload, the transferrin saturation is >55 %, and the serum ferritin level is usually >200 μg/L in women and >300 μg/L in men [242]. Significant myocardial siderosis is generally defined as a myocardial T_2* value of <20 ms when assessed by CMRI with the T_2* imaging sequence [116, 243]. The causes of IOC can be divided broadly into two groups: those related to increased iron absorption (primary hemochromatosis) and those related to frequent blood transfusion therapy (secondary hemochromatosis). Anemia requiring blood transfusion can be hereditary, as in thalassemia and sickle cell disease, or can be acquired, as in myelodysplastic syndromes and myeloproliferative disorders [244]. The main organs that are affected by severe iron overload include the heart, endocrine glands, and hepatic system. Significant myocardial iron deposition causes cardiac failure and death at a young age. In fact, IOC is responsible for a third of all deaths in patients with hereditary hemochromatosis, is a major cause of death in patients with secondary hemochromatosis, and is the leading cause of mortality in patients with thalassemia major [245]. Without proper iron chelation therapy, most patients with IOC will develop a dilated phenotype, which is characterized by LV remodeling and LV systolic dysfunction, as well as LV and RV enlargement. In contrast, a minority of these patients (<10 %) will develop a restrictive phenotype, which is characterized by biatrial enlargement, a restrictive LV filling pattern, RV enlargement, and a preserved LVEF [245].

Echocardiography can be used to evaluate ventricular and atrial chamber size and to assess both systolic and diastolic function indices by using traditional and novel imaging parameters [246]. Chamber enlargement or LV systolic dysfunction may indicate advanced disease [116]. Echocardiography cannot detect the presence or absence of myocardial siderosis, much less quantify it. Serum ferritin also cannot be used to predict the myocardial iron content [116]. Tissue biopsy is considered the gold standard for the diagnosis of IOC. However, tissue biopsy is an invasive procedure, and the patchy distribution of myocardial siderosis may be missed by this technique.

Currently, CMRI is the only noninvasive means for quantifying myocardial siderosis. The Royal Brompton Hospital group pioneered the use of T_2* for the diagnosis of IOC [116]. Figure 13.22 shows an example of findings for a patient with both hepatic and myocardial siderosis. In the United Kingdom, the use of T_2* CMRI to identify IOC appears to have improved the survival of patients with thalassemia major because they received timely intensification of chelation therapy, thereby preventing myocardial iron overload [247]. Between 1980 and 1999, these patients' rate of death due to iron overload was 7.9 per 1,000 patient-years, whereas between 2000 and 2003, it was 2.9 per 1,000 patient-years—a 71 % reduction (P <0.05). In the original CMRI T_2* assessment of patients with thalassemia major by Anderson and colleagues [116], all patients with ventricular dysfunction had a T_2* value of <20 ms, leading the authors to suggest that values above this threshold indicate the presence of substantial myocardial siderosis. Wood and colleagues [248] subsequently sought to confirm the utility of T_2* measurements for quantifying myocardial iron by using an iron dextran-loaded gerbil model. Myocardial and hepatic T_2* measurements were taken both in vivo and ex vivo. The investigators found a strong correlation between $1/T_2$* and myocardial iron (wet weight) ($r^2 = 0.94$).

T_2* measurement can accurately quantify myocardial iron levels in IOC patients. This is important for assessing the risk of cardiac complications and tailoring the appropriate iron-chelating treatment [119]. Furthermore, T_2* measurement allows the early detection of myocardial siderosis, which may be reversible if aggressive chelation therapy is commenced early enough [243]. In addition, T_2* measurement can be used to monitor the chelating regime in these patients. Excellent review articles by Kremastinos and colleagues [245] and by Gujja and coauthors [246] provide management algorithms that are guided by CMRI T_2* measurements for patients with IOC.

In a recent CMRI study of more than 1,400 patients with thalassemia major, myocardial T_2* imaging was performed [249]. At the time of examination, the majority of patients had no arrhythmias or clinical signs of congestive heart failure. Of the patients with a T_2* value of <6 ms, 47 % developed heart failure and 14 % developed an atrial or ventricular arrhythmia within 1 year of scanning. Table 13.6 shows the risk of developing congestive heart failure or an arrhythmia in relation to the patient's T_2* value [249]. In another study, 15 patients with thalassemia major underwent a combination chelating treatment with subcutaneous deferoxamine and oral deferiprone [243]. At 1-year follow-up evaluation, the myocardial T_2* values had increased from 5.7 ± 0.98 to 7.9 ± 2.47 ms (P = 0.010), and the LVEF had increased from 51.2 ± 10.9 % to 65.6 ± 6.7 % (P <0.001).

Magnetic Resonance Angiography of Coronary Artery Disease

According to the American Heart Association, more than one million inpatient diagnostic cardiac catheterizations were performed in 2009 [250]. The American College of Cardiology Foundation and the Society for Cardiovascular Angiography

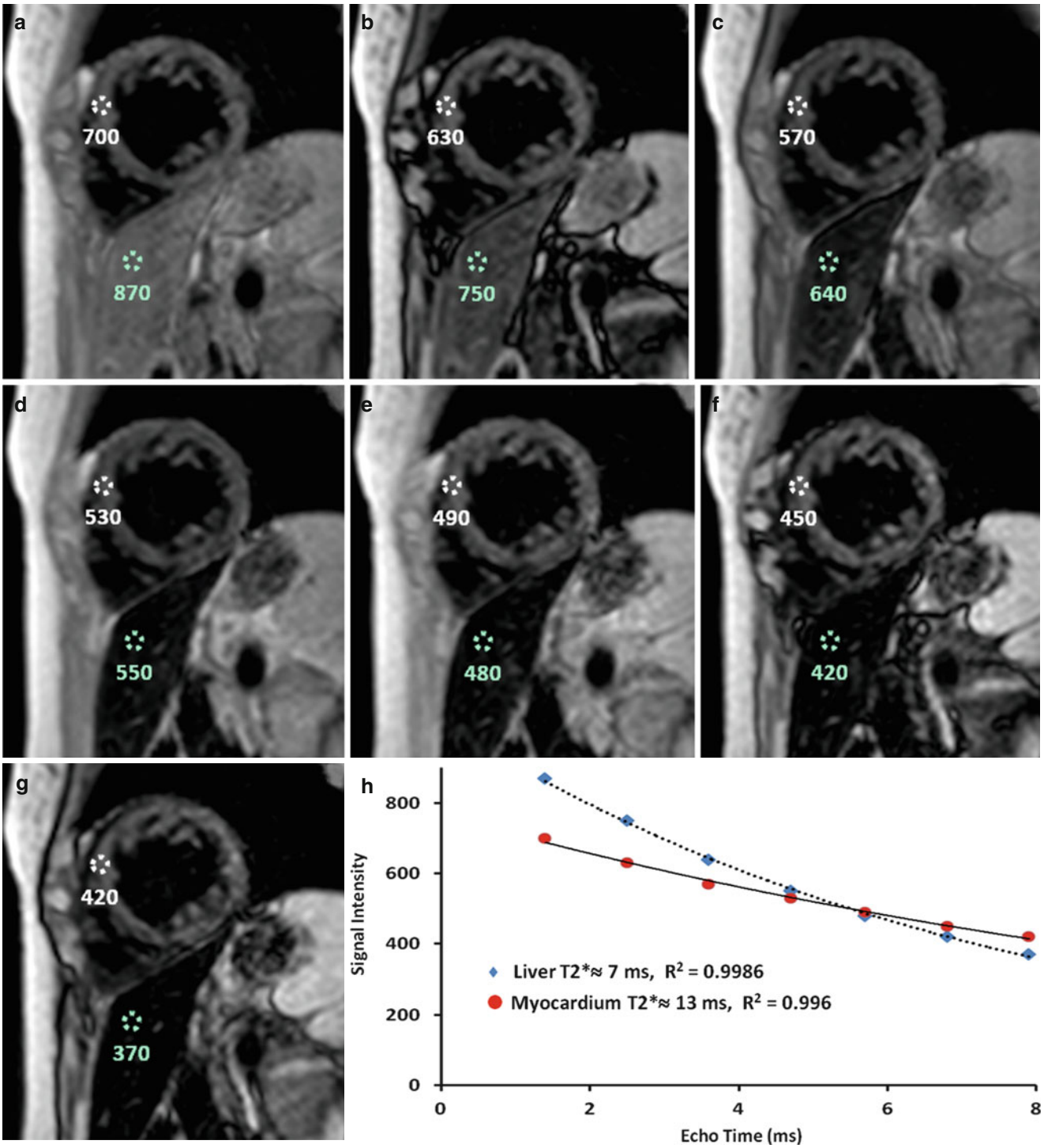

Fig. 13.22 Images from a 38-year-old man with hemochromatosis who presented for evaluation of possible cardiac involvement. Cine gradient-echo images of the heart indicated normal left ventricular systolic function (not shown). A T2* analysis of the heart and liver was performed in the mid left ventricular short-axis orientation by using a multi-echo, inversion-recovery black-blood preparation, gradient-echo sequence. For the heart, the region of interest was placed in the interventricular septum and propagated to the same location in each image. A similar procedure was performed in the liver. (**a**–**g**) Images showing the signal intensity for each organ at different echo times. (**h**) The T2* values of the myocardium and the liver were computed by plotting the signal intensities of each against the echo times. In this patient, the T2* values of the myocardium and liver were 13 and 7 ms, respectively, suggesting significant iron deposition in both organs (<20 ms indicates significant iron deposition). The high R^2 values indicate that the curves generated fit the data well

Table 13.6 Risk of congestive cardiac failure and arrhythmia in patients with thalassemia major, as assessed by cardiovascular magnetic resonance imaging using the T_2* sequence

Congestive heart failure					
Cardiac T_2*(ms)	**No. of Pts**	**Pts with CHF (No.; %)**	**Relative risk**	**95 % CI**	***P* value**
<6	72	34 (47.2)	270	64–1,129	<0.001
6–<8	98	29 (29.6)	171	41–718	<0.001
8–<10	108	15 (13.9)	81	19–357	<0.001
≥10	1,164	2 (0.17)	1	Reference	–
Atrial or ventricular arrhythmias					
Cardiac T_2* (ms)	**No. of Pts**	**Pts with arrhythmia (No.; %)**	**Relative risk**	**95 % CI**	***P* value**
<6	72	14 (19.4)	8.79	4.03–19.2	<0.001
6–<8	98	20 (20.4)	7.5	3.71–15.2	<0.001
8–<10	108	16 (14.8)	6.82	3.28–14.2	<0.001
10–<15	263	21 (8.0)	3.23	1.65–6.3	0.001
15–<20	165	10 (6.1)	2.21	0.97–5.02	0.058
≥20	736	17 (2.3)	1	Reference	–

Modified with permission from Kirk et al. [249]
Pts patients, *CHF* congestive heart failure, *CI* confidence interval

Table 13.7 Comparison of coronary magnetic resonance angiography and coronary computed tomography angiography

Variable	CMRA	CCTA
Time for data acquisition	Minutes	Seconds
Radiation	No	Yes
Contrast medium	None or gadolinium	Iodine
Low heart rate for data acquisition	Not mandatory	Highly recommended
Spatial resolution	≈1 × 1 × 1 mm^3	≈0.5–0.625 mm in x, y, z direction
Sensitivity	≈88 %	>95 %
Specificity	>90 %	>90 %
Technical expertise	High	Low
Arrhythmia	Less important due to averaging	Important, as the whole scan usually takes less than a few seconds
Patient comfort	Average (mostly due to scan duration: reduced in screening CMRA)	Very comfortable
Atherosclerosis analysis	Has been described in literature	Has been well described in literature
Prognostic data	No	Yes

CMRA coronary magnetic resonance imaging, *CCTA* coronary computed tomography angiography

and Interventions estimates that the rate of normal findings or insignificant CAD varies from 20 to 39 % [251, 252]. Conventional coronary angiography is still the gold standard for assessing coronary artery stenosis. Nevertheless, angiography is an invasive procedure with a small, yet inherent risk of complications, including MI, stroke, arrhythmias, and death [251]. A noninvasive imaging method that could directly assess the integrity of the coronary lumen would be desirable.

Over the past decade, coronary CT angiography (CCTA) has been shown to be a robust noninvasive modality in the assessment of CAD. In a meta-analysis comparing 64-slice CCTA with diagnostic angiography, the patient-based pooled sensitivity, specificity, and positive and negative predictive values were 99, 89, 93, and 100 %, respectively; in a segment-based analysis, these same values were 90, 97, 76, and 99 %, respectively [253]. During CCTA, patients are exposed to radiation in the form of iodinated contrast agents. For high-quality results, the heart rhythm must be slow and regular.

Coronary magnetic resonance angiography (CMRA) was first described by Paulin and colleagues [254] using spin-echo sequences (1987) and by Wielopolski and colleagues [255] using gradient-echo sequences (1995). Since then, CMRA imaging has undergone significant improvement with respect to coverage, spatial resolution, and acquisition time, as well as the use of Gd-based contrast agents to further improve image quality. Table 13.7 shows a comparison between CMRA and CCTA.

This review provides a brief synopsis of the basic technical aspects of CMRA, as well as some common indications for its use.

Technical Aspects

Because of its high spatial resolution (approximately 0.1–0.2 mm) and high temporal resolution (10–20 ms), cardiac

catheterization with coronary angiography is considered the gold standard for evaluating CAD [256]. This approach can also allow therapeutic intervention in the same setting. Several technical challenges involved in noninvasive imaging of the coronary arteries with CMRA include the need for (1) a relatively high spatial resolution for evaluating stenosis; (2) a high temporal resolution and fast imaging time to "freeze" the fast-moving arteries; (3) methods for overcoming patient respiratory and cardiac motion, which affect the quality of the image; and (4) adequate coverage of the entire coronary tree. An excellent review of the technical aspects of CMRA has been published by Flamm and Muthupillai [257].

Imaging of epicardial coronary arteries is demanding because of their relatively small diameter (2–5 mm). The scan time for a 2D image is governed by the repetition time (ms) × the number of phase-encoding steps. Using a fixed field of view, one may increase the spatial resolution by increasing the number of phase-encoding steps and, therefore, prolonging the scan time. The introduction of parallel imaging techniques, such as SENSE, allows either a faster imaging time or increased spatial resolution [258]. In addition, a state-of-the-art phase-array coil, such as a 32-channel cardiac coil, allows the use of SENSE in two directions. Compared to the standard 5-channel cardiac coil, the 32-channel coil reduces the imaging time by almost 50 % while offering comparable imaging quality. Alternatively, it can improve spatial resolution at the expense of increased imaging time [259]. With a 1.5 T scanner, 32-channel coil, and Gd infusion, the imaging spatial resolution was $1.1 \times 1.1 \times 1.5$ mm^3 in a series recently reported by Nagata and colleagues [259]. With a 3 T scanner, 32-channel coil, and slow gadobenate dimeglumine infusion, Yang and associates [260] obtained a spatial resolution of $1.1 \times 1.1 \times 1.3$ mm^3. The rest period for coronary arteries is short, ranging from 66 to 333 ms (mean, 161 ms) for the left coronary artery (LCA) and from 66 to 200 ms (mean, 120 ms) for the RCA [261]. A coronary artery can move several centimeters during the cardiac cycle, and peak velocities of 2 cm/s have been documented during certain phases, such as rapid cardiac contraction and relaxation. As a result, high temporal resolution is necessary to obtain a motionless image [254]. In CMRA, the data are synchronized with the electrocardiogram and are usually acquired in the *telediastolic* phase (55–75 % of the R-R interval, or approximately −300 to −400 ms before the electrocardiographic R wave), when cardiac motion is usually minimal. In patients with a higher heart rate, the *telesystolic* phase may be used (25–35 % of the R-R interval, or approximately 200–300 ms after the R wave), when cardiac contraction is limited during isovolumic contraction. Because the RCA has a shorter rest period than the LCA [261], the trigger delay (selected time at which to start imaging during the cardiac cycle) is determined by performing a free-breathing cine SSFP sequence in the axial orientation involving a high number of cardiac phases. Both the trigger delay and the duration in which the RCA is relatively stationary are then determined at the imaging console [255].

To suppress respiratory motion, two approaches may be used. In one approach, different segments of the coronary arteries are imaged separately during different breath-holds after an initial low-resolution, 3-dimensional (3D) scan is performed in a single breath-hold [262]. This approach is termed volume coronary angiography with target scans. The other method for suppressing respiratory motion is respiratory gating, which uses a prospective real-time navigator to measure displacement of the coronary arteries due to breathing; the data are then accepted or rejected on the basis of displacement [263]. In this approach, a navigator pencil beam is usually placed on the dome of the right hemidiaphragm, along the liver-lung boundary in the foot-to-head direction, to monitor respiratory motion. An acceptance window is set, usually between 3 and 6 mm. Data will be accepted if they fall into this window; otherwise, the data will be rejected and remeasured in other cardiac cycles. The advantage of respiratory gating is that images are collected with free breathing, so a high spatial resolution and signal-to-noise ratio can be achieved. The disadvantages are the longer imaging time, sensitivity to irregular breathing patterns, and individual variations in the relationship between diaphragmatic and cardiac motion. As the motion of the heart is less than that of the diaphragm during breathing, a scale factor of 0.6 is commonly applied [264]. Some investigators also ask the patient to wear an abdominal belt to suppress diaphragmatic motion during breathing [259, 265].

In 2003, Weber and colleagues [266] introduced the 3D whole-heart imaging approach, using parallel imaging to reduce the scan time and an SSFP imaging sequence to improve the image quality. In the whole-heart approach, the entire heart is imaged from the origins of the coronary arteries to the cardiac base. Planning can easily be done on the basis of information obtained in the survey scan, thereby reducing the time required in the target-volume approach for coronary artery orientation planning. The trigger delay is determined by a high-temporal-resolution cine scan, as described above, and whole-heart data are acquired with a free-breathing technique. In the original report, the spatial resolution was $1 \times 1 \times 1.5$ mm^3, with a mean imaging time of 13:48 min (range, 7:18–20:18 min).

Whole-heart CMRA is currently the most widely used approach in coronary imaging [7, 260, 264, 267, 268]. Steady-state free-precession sequences are preferred with the 1.5 T scanner, which utilizes fully refocused gradients in each repetition time to maintain steady-state transverse magnetization. Therefore, the signal-to-noise and contrast-to-noise ratio is higher than with the traditional spoiled GRE sequence, as the GRE sequence has limited blood-inflow–related signal enhancement. However, a major challenge of

Table 13.8 Diagnostic accuracy of coronary magnetic resonance angiography for significant coronary artery disease: results of selected studies

Authors	No. of Pts	Scanner	Contrast	Level	Sens (%)	Spec (%)	PPV (%)	NPV (%)	Acc (%)	Angio cutoff	Imaging time (min)	Success rate	Remarks
Sakuma et al. [267]	113	1.5 T	No	Pt Vessel Seg	82 78 78	90 96 96	88 79 69	86 95 98	87 93 94	≥50 % diameter reduction. Vessel ≥2 mm	12.9 ± 4.3	113/131 pts (86 %)	SSFP; 5-channel coil. No medication given. CAD prevalence 45 %. Weight = 63 ± 10 kg
Yang et al. [268]	62	3 T	Yes[a]	Pt Vessel Seg	94 92 91	89 94 96	91 86 76	92 97 99	92 94 95	≥50 % diameter reduction. Vessel ≥1.5 mm	9.0 ± 1.9	62/69 pts (90 %)	Oral β-blocker if HR >75 bpm. 12-channel coil. Segmented GRE. CAD prevalence 55 %. BMI = 24 ± 2.8 kg/m^2
Kato et al. [265]	127	1.5 T	No	Pt Vessel Seg	88 83 81	72 90 98	71 67 71	88 96 99	79 89 97	≥50 % diameter reduction. Vessel ≥2 mm	9.5 ± 3.5	127/138 pts (92 %)	ISDN 5 mg given. 5-channel coil. SSFP. CAD prevalence 44 %. BMI = 24 ± 4 kg/m^2
Nagata et al. [259]	67	1.5 T	No	Pt Vessel Seg	87 86 83	86 93 98	89 86 81	83 93 98	87 91 97	≥50 % diameter reduction. Vessel ≥2 mm	6.2 ± 2.8	67/67 pts (100 %)	ISDN 5 mg given. 32-channel coil. SSFP. CAD prevalence 58 %. BMI = 23 ± 3 kg/m^2
Yang et al. [260]	101	3 T	Yes[b]	Pt Vessel Seg	96 89 85	87 91 92	87 69 51	96 97 98	91[c] NR 98[c]	≥50 % diameter reduction. Vessel ≥1.5 mm	7.0 ± 1.8	101/110 patients (92 %)	Oral β-blocker if HR >75 bpm. CAD prevalence, 49 %. 32-channel coil. Segmented GRE. BMI = 24 ± 3 kg/m^2

No. of Pts number of patients, *Sens* sensitivity, *Spec* specificity, *PPV* positive predictive value, *NPV* negative predictive value, *Acc* accuracy, *Angio* angiography, *SSFP* steady state free precession, *Seg* segment, *CAD* coronary artery disease, *HR* heart rate, *GRE* gradient-recalled echo, *BMI* body mass index, *ISDN* isosorbide dinitrate, *NR* not reported

[a]0.2 mmol/kg gadobenate dimeglumine

[b]0.15 mmol/kg gadobenate dimeglumine

[c]Calculated from available data

using SSFP sequences in 3 T compared to 1.5 T imaging is sensitivity to increased B_0 and B_1 inhomogeneities [269]. With the increases in field strength, the specific absorption rate is also increased, so the repetition time must be longer. The imaging flip angle also needs to be higher to obtain sufficient contrast between the blood and myocardium. A gradient-echo sequence is the modality of choice in 3 T CMRA.

A magnetization-prepared, T_2-weighted sequence (T_2-prep) is commonly used to accentuate the difference between the T_2 values of arterial (250 ms) and venous (35 ms) blood and myocardium (50 ms), thus suppressing signals from the myocardium and venous structures [270]. In addition, to suppress signals from surrounding fat, a spectrally selective fat-saturation pulse is applied before data acquisition.

Acquired Coronary Artery Disease

In 2001, Kim and colleagues [271] described a single-vendor, multicenter CMRA study in which a 1.5 T scanner without Gd contrast was used with a targeted approach and a respiratory navigator free-breathing technique. A total of 109 patients were imaged, and the results were compared to those of invasive coronary angiography (in which significant stenosis is defined as ≥50 % luminal narrowing). The prevalence of CAD was 59 %. The CMRA analysis was limited to the proximal coronary segments. The mean coronary coverage was approximately 6 cm for the LAD, 8 cm for the RCA, and 3 cm for the left circumflex artery. Based on the consensus of two expert readers at the core laboratory, the sensitivity, specificity, and accuracy of CMRA for detecting significant CAD were 93, 42, and 72 % respectively. For the detection of left main coronary artery (LMCA) or three-vessel disease, the sensitivity, specificity, and accuracy were 100, 85, and 87 %, respectively. The results were poorer for individual arteries. The limitations of the study included the long imaging time, the fact that only 84 % of the segments could be evaluated, and the limited coronary coverage.

Since Kim's report was published, advances in hardware and software, as well as the introduction of the SSFP sequence, have significantly improved the ability of CMRA to detect CAD. Table 13.8 summarizes some selected recent publications about the use of CMRA with the whole-heart approach versus invasive angiography as the gold standard for diagnosing CAD [259, 260, 265, 267, 268]. Interestingly,

the included publications predominantly concern the Asian population, whose relatively low body-mass index (mean, <25 kg/m^2) could certainly affect image quality. As Nagel indicated in his editorial [272], the results of the CMRA studies included in Table 13.8 were comparable to those observed in the recently published CORE-64 CCTA study [273, 274]. In the original report of this study, 291 patients with an Agatston calcium score of <600 were analyzed by using invasive coronary angiography as the reference standard. The sensitivity, specificity, and positive and negative predictive values were 0.85, 0.90, 0.91, and 0.83, respectively [274]. The subsequent report concerned another 80 patients with Agatston calcium scores of ≥600 who were not included in the original report; in their cases, the sensitivity, specificity, and positive and negative predictive values were 0.94, 0.44, 0.93, and 0.50, respectively [273]. When both groups were combined, the overall sensitivity, specificity, and positive and negative predictive values were 0.88, 0.87, 0.92, and 0.81 [273].

For evaluating the coronary anatomy in patients with chest pain and an intermediate pretest likelihood of CAD, CCTA is probably the noninvasive imaging modality of choice, due to its short imaging time (from 5 to 6 s of breath-holding in a 64-detector CT scanner to 1 s of breath-holding in a 320-detector or dual-source CT scanner) [275]. Moreover, CCTA is preferred despite the need for ionizing radiation and iodinated contrast, as well as a slow, steady heart rate to achieve high-quality data and minimize radiation. Compared to CMRA, all CT scanners with 64 or more detectors have detector widths of 0.5–0.625 mm and, therefore, offer high isotropic spatial resolution. However, in patients who have a true allergy to iodine contrast or who have significant calcification, CMRA could play a role in the assessment of coronary stenosis [276]. In the American Heart Association's 2008 scientific statement regarding CMRA and CCTA [277], the committee recognized that the majority of reports were published by experienced physicians at academic centers. The committee concluded that "*the utility of coronary MRA in general practice has not been established, and multivendor trials have not been conducted*."

Most CMRA studies have been performed without Gd contrast administration. Hu and colleagues [7] evaluated the use of 0.2 mmol/kg of gadobenate dimeglumine injected at 2 cc/s during whole-heart CMRA with a 1.5 T scanner. The signal-to-noise and contrast-to-noise ratios were significantly higher in the contrast study than the noncontrast study, which were performed 1 week apart in each subject. In addition, the coronary artery vessel length was greater in the contrast study than the noncontrast study. Myocardial suppression was also improved with the application of a nonselective inversion pulse. Similarly, in 3 T CMRA, the use of Gd improves the signal-to-noise and contrast-to-noise ratios, especially when the GRE technique is the preferred imaging sequence [263, 268]. With the addition of an inversion pulse, the contrast between blood and background tissue is higher; with the higher spatial resolution, 3 T CMRA can assess smaller and more distal vessels (up to 1.5 mm in diameter) [263, 268].

Kawasaki Disease

Kawasaki disease (KD) is an acute necrotizing vasculitis of medium and small vessels that affects mostly infants and young children. It is characterized by fever, a rash, bilateral nonexudative conjunctivitis, erythema of the lips and oral mucosa, cervical lymphadenopathy, and changes in the extremities [278]. Organs that may be affected by this systemic disease include the heart, liver, lungs, and kidneys. Coronary artery aneurysm or ectasia develops in 20–25 % of untreated patients and can lead to myocardial ischemia, infarction, and death [279].

Because coronary artery aneurysm or ectasia is a major potential complication of KD, noninvasive imaging of the heart and coronary arteries is an important part of the evaluation and follow-up of KD patients [278]. The American Heart Association and other professional societies recommend surface echocardiography as the imaging method of choice for these patients [278]. Although invasive coronary angiography is the gold standard for evaluation of the coronary anatomy, CMRA has been shown to be a noninvasive alternative that reduces radiation exposure and the potential complications of coronary angiography. In six patients with KD, Greil and colleagues [280] performed targeted 3D segmented k-space free-breathing gradient echocardiography with navigator gating, as well as CMRA and conventional coronary angiography. Compared to coronary angiography, CMRA correctly identified all coronary aneurysms (n = 11), coronary stenoses (n = 2), and coronary occlusions (n = 2). In addition, there was close agreement between CMRA and conventional coronary angiography with regard to the proximal coronary artery diameter and the distance from the coronary ostium to the origin of the aneurysm.

A recent review has suggested that CCTA, rather than CMRA, may be the preferred imaging method for monitoring the evolution of KD over time, with regard to both aneurysmatic dilatation and mural thrombosis [281]

Magnetic Resonance Imaging of Congenital Coronary Artery Anomalies

In a frequently quoted analysis of 125,595 patients who underwent invasive coronary angiography at the Cleveland Clinic Foundation [282], the following incidences of congenital coronary artery anomalies (CAAs) were documented: LMCA, LAD, or RCA arising from the pulmonary artery, 0.01 %; LMCA arising from the right sinus of Valsalva (RSV), 0.018 %; LAD arising from the RSV, 0.03 %; and RCA arising from the left sinus of Valsalva (LSV), 0.108 %.

More recent, unbiased CMRA studies of a large general population in adolescents revealed that 0.7 % of the subjects had important CAAs (see below) [283]. Machado and colleagues [284] were probably the first to report the use of MRI to visualize an anomalous RCA with T_1 spin-echo sequences. McConnell and associates [285] used 3D breath-hold, ECG-gated, segmented k-space, gradient-echo sequences to evaluate 15 patients with CAAs. All 15 patients had anomalous CAAs on invasive angiography, and CMRA correctly identified 14 of them. Post and colleagues [286] studied 37 patients by means of breath-hold 2D fast gradient-echo images; 19 patients were known to have anomalous coronary artery origins, and the remainder of the patients (the control group) had normal coronary origins. The CMRA images were reviewed blindly by two observers, and two other independent cardiologists reviewed the invasive angiograms separately. In the final consensus interpretation by all readers, CMRA had a sensitivity and specificity of 100 % in identifying the origins and proximal course of the anomalous arteries [286]. Because some patients may not be able to perform adequate breath-holding, current CMRA performed for CAA assessment is usually achieved with 3D gradient-echo sequences using a respiratory navigator technique, thus allowing the data to be acquired during free breathing. As the majority of clinical examinations are requested for suspicion of anomalous coronary origin without a concern for underlying arterial stenosis, coverage could be limited to the aortic root and proximal ascending aorta, with a relatively generous in-plane spatial resolution of 1–1.5 × 1–1.5 mm. With a navigator efficiency of 30–50 % and a cooperative patient, the dataset could be acquired in less than 5 min in most instances.

In the 2006 multi-group Appropriateness Criteria for CCTA and Cardiac MRI, the use of CMRA for assessment of suspected CAAs is graded as *appropriate*, with an average score of 8 (a score of 7–9 indicates an appropriate test for a specific indication) [2]. In addition, the 2008 American Heart Association scientific statement gives a Class IIa, evidence level B, recommendation for the use of CMRA or CCTA in evaluating CAAs [277]. This rating is presumably due to the relatively limited number of studies, which have mostly been confined to single centers.

Most CAAs diagnosed by CMRA are accidental findings that are discovered during the investigation of coronary atherosclerotic disease in the adult. The following section discusses (1) the general outline of the entity known as CAA (Table 13.9); (2) the use of MRI for screening young people to evaluate the risk of SCD; (3) the use of MRI for evaluating the severity of stenosis in some forms of CAA; and (4) the use of MRI versus CCTA versus intravascular ultrasonography or intravascular optical coherence tomography for imaging CAAs.

General Outline of Coronary Artery Anomalies

Coronary artery anomalies are defined as coronary anatomic patterns that are outside the spectrum of normal [287, 288].

1. "Normal" anatomic forms are generally defined as all the variants observed in more than 1 % of the general population.
2. Clinically or prognostically "serious" CAAs are those that entail a high risk for SCD, especially in young persons and during exercise.
3. Serious CAAs are distinguished by their capacity to produce ischemia and its consequences: chest pain, dyspnea, and syncopal equivalents, as well as sudden cardiac arrest or death [287, 288].
4. In the diagnostic imaging of CAAs, the primary and fundamental objective is to properly identify the morphologic variants, especially those that have significant prognostic implications.

Classification of Coronary Artery Anomalies

Schemes for classifying CAAs are widely discussed in the current literature, but no final, widely recognized classification scheme has been agreed on. Table 13.9 shows a classification proposed by our group at the Texas Heart Institute [287], including a brief characterization of each form in terms of the demonstrated or likely mechanism of ischemia. Magnetic resonance angiography is quite able to identify most of these variants (Figs. 13.23–13.34).

Whereas 1–5 % of the general population has some type of CAA [287], less than 10 % of these "carriers" will experience ischemic consequences. The only CAAs that can potentially cause ischemic manifestations are those involving a mechanism of stenosis that varies in severity in each case. Here we will discuss the most important of these "potentially serious CAAs," which occur in young persons and adults. Most other CAAs also need to be diagnosed properly because of the confusion that an incorrect diagnosis can generate.

Anomalous Coronary Artery Originating from the Opposite Sinus of Valsalva with an Intramural Course

In adults, the best characterized and most clinically serious type of CAA—the one that most frequently features the pathophysiologic mechanism of a high-risk CAA—involves an ectopic artery that originates from the opposite sinus of Valsalva (ACAOS) and has an intramural course inside the aortic root [287–291]. In this entity, typically either the RCA arises from the LSV (R-ACAOS), or the LCA

Table 13.9 Classification of coronary anomalies in human hearts

Anomaly	Mechanism of ischemia
A. *Anomalies of origination and course*	
1. Absent left main trunk (split origination of LCA)	None
2. Anomalous location of coronary ostium within aortic root or nearby	None
(a) Proper aortic sinus of Valsalva (for each artery)	
(b) High or commissural	
(c) Sometimes IM	
3. Anomalous location of coronary ostium outside normal "coronary" aortic sinuses	
(a) Right posterior aortic sinus ("noncoronary")	Sometimes IM
(b) Ascending aorta and aortic arch	
(i) Innominate artery	None
(ii) Right carotid artery	None
(iii) Internal mammary artery	None
(iv) Bronchial artery	None
(v) Subclavian artery	None
(c) Left ventricle	Steal
(d) Right ventricle	Steal
(e) Origin from pulmonary artery	
(i) LCA arising from posterior left-facing sinus	Steal
(ii) Cx arising from posterior left-facing sinus	Steal
(iii) LAD arising from posterior left-facing sinus	Steal
(iv) RCA arising from anterior right facing sinus	Steal
(v) Ectopic location (outside facing sinuses) of any coronary artery arising from pulmonary artery:	
(*a*) From anterior left sinus	Steal and sometimes IM with stenosis
(*b*) From pulmonary trunk	Steal and sometimes IM with stenosis
(*c*) From pulmonary branch	Steal and sometimes IM with stenosis
4. Anomalous location of coronary ostium at improper coronary sinus (which may involve joint origination or a "single" coronary pattern)	
5. RCA arising from left anterior sinus, with anomalous course	
(a) Posterior atrioventricular groove or retrocardiac	None
(b) Retroaortic	None
(c) Between aorta and pulmonary artery	IM Stenosis
(d) Intraseptal	None
(e) Anterior to pulmonary outflow	None
(f) Postero-anterior interventricular groove (wrap-around)	None
6. LAD arising from right anterior sinus, with anomalous course	
(a) Between aorta and pulmonary artery	IM Stenosis
(b) Intraseptal	None
(c) Postero-anterior interventricular groove (wraparound)	None
7. Cx arising from right anterior sinus, with anomalous course	
(a) Posterior atrioventricular groove	None
(b) Retroaortic	None
8. LCA arising from right anterior sinus, with anomalous course	
(a) Posterior atrioventricular groove	None
(b) Retroaortic	None
(c) Between aorta and pulmonary artery	IM Stenosis
(d) Intraseptal	None
(e) Anterior to pulmonary outflow	None
(f) Postero-anterior interventricular groove	None
B. *Anomalies of intrinsic coronary arterial anatomy*	
1. Congenital ostial stenosis or atresia (LCA, LAD, RCA, Cx)	Stenosis
2. Coronary ostial dimple	None
3. Coronary ectasia or aneurysm	Thromboembolism

(continued)

Table 13.9 (continued)

Anomaly	Mechanism of ischemia
4. Absent coronary artery	None
5. Coronary hypoplasia	None
6. Intramural coronary artery (myocardial bridge)	Spasm
7. Subendocardial coronary course	None
8. Coronary crossing	None
9. Anomalous origination of posterior descending artery from the anterior descending branch or a septal penetrating branch	None
10. Split RCA	None
11. Split LAD	None
12. Ectopic origination of first septal branch	None
C. *Anomalies of coronary termination*	
1. Inadequate arteriolar/capillary ramifications—Hypoperfusion	
2. Fistulas from RCA, LCA, or infundibular artery to:	
(a) Right ventricle	Thromboembolism, stenosis, steal
(b) Right atrium	Same
(c) Superior vena cava	Same
(d) Coronary sinus	Same
(e) Pulmonary artery	Same
(f) Pulmonary vein	Same
(g) Left atrium	Same
(h) Left ventricle	Same
(i) Multiple, to right and/or left ventricles (microfistulas)	
(*a*) Anomalous anastomotic vessels (congenital, no stenosis)	None

Adapted from Angelini [287, 288] with permission
LCA left coronary artery, *IM* intramural, *Cx* circumflex artery, *LAD* left descending coronary artery, *RCA* right coronary artery

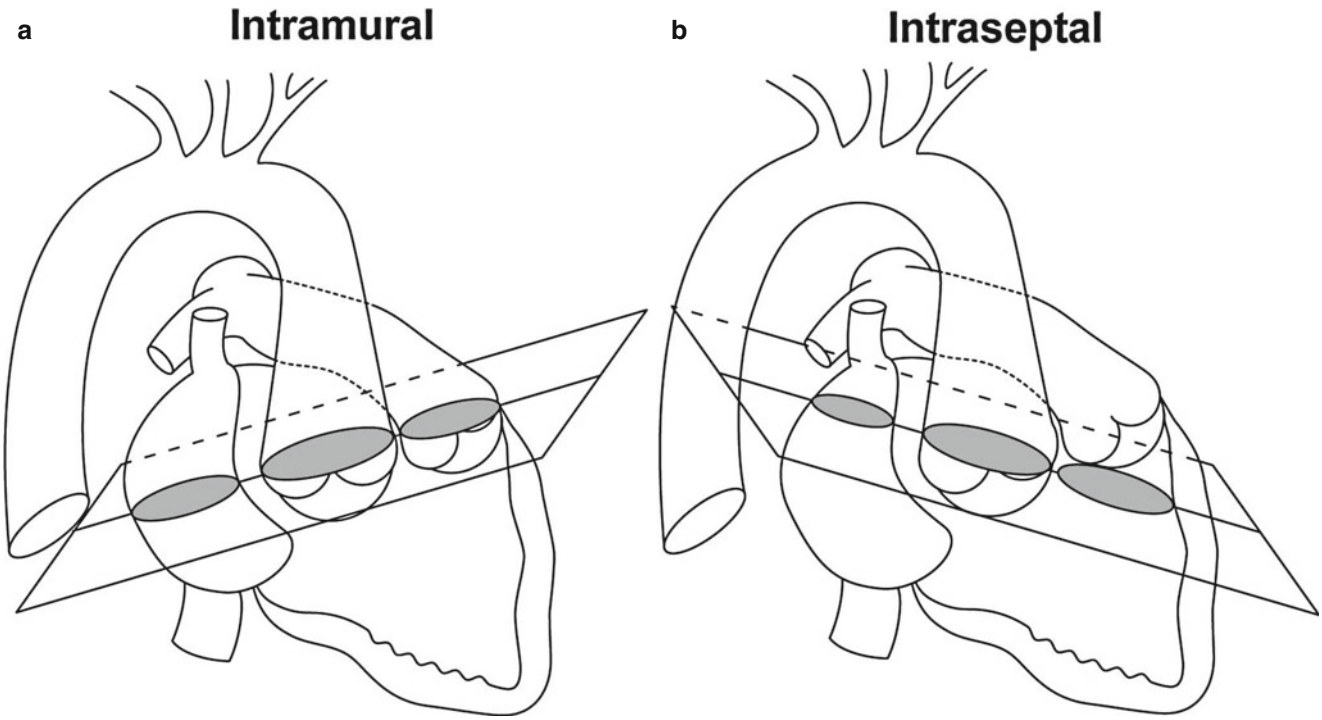

Fig. 13.23 Diagrammatic views of typical tomographic images of the proximal coronary arteries in cases of ectopic aortic origin, typically used in diagnosing intramural (**a**) versus intraseptal (**b**) abnormal courses of the left coronary artery (LCA) (see text). Note that the two cuts pass though the aortic root: in view (**a**), the cut is also through the pulmonary root (around the level of the sinutubular junctions); in view (**b**), however, the more anterior section of the cut is obliquely oriented in order to pass though the right ventricular outlet. In view (**a**), the cut is ideal for studying ACAOS, and in view (**b**), the cut is ideal for studying the intraseptal (or infundibular) variety

arises from the RSV (L-ACAOS), and the affected artery pursues a preaortic course, running inside the aortic-wall media and crossing in front of the anterior aortic commissure before reaching its proper destination [289, 290]. This type of course has long been called "between the aorta and pulmonary artery, or interarterial" [287, 288]. Because of the recent discovery that this treacherous course is, however, always located inside the aortic wall and is essential to the nature of this entity, it has been suggested that previous names be changed to ACAOS and that the "intramural course" be underscored as the required common feature, which correlates with the prognosis and symptoms [287, 289–291]. At the embedded segment, the coronary artery is affected both in its internal circumference (which is typically smaller than that of the distal segment, leading to a characteristic but variable degree of hypoplasia, and is also laterally compressed, as shown in Figs. 13.30–13.34) and in its pulsatile cross-sectional area, which is further later-

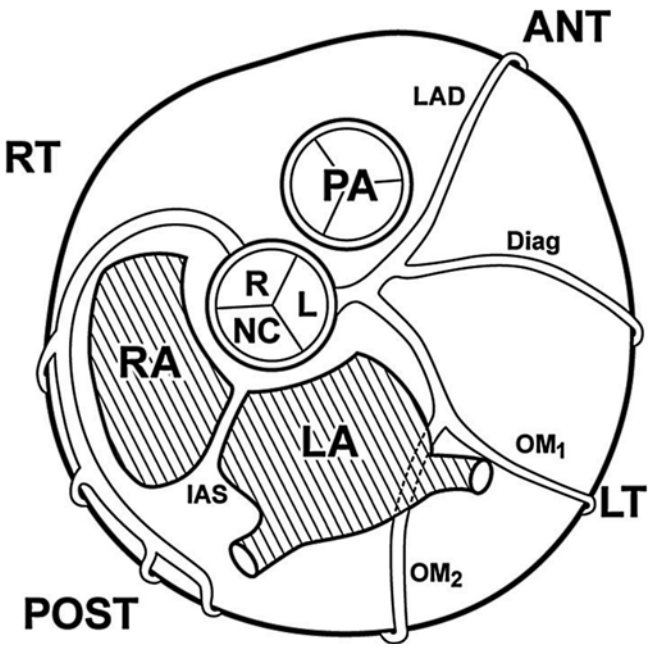

Fig. 13.24 Normal coronary arteries. Diagrammatic rendering of the normal coronary arteries on the customary computed tomography angiography or magnetic resonance imaging planes, as seen from below (Cartesian coordinates: *ANT* anterior, *LT* left, *POST* posterior, *RT* right), passing through an oblique cut at the sinutubular junctions of the great vessels (see Fig. 13.23). In a similar plane, the observer should be able to identify the basic reference structures that describe the coronary anatomy, including the commissures of the aortic valve, as well as the sinuses of Valsalva: the right anterior (*R*), left anterior (*L*), and posterior or noncoronary (*NC*) sinuses. In this format, the proximal right coronary artery (RCA) is directed superiorly/laterally and around the right atrium (*RA*), while originating from the middle of the proper sinus. The proximal left coronary artery (LCA) arises from the middle of the left sinus and courses around the left atrium (*LA*). Note that the noncoronary sinus is aligned with the interatrial septum (*IAS*), while the anterior commissure is located at the contact site between the aorta and pulmonary artery. *Diag* diagonal artery, *LAD* left anterior descending artery, OM_1 first obtuse marginal branch, OM_2 second obtuse marginal branch, *PA* pulmonary artery

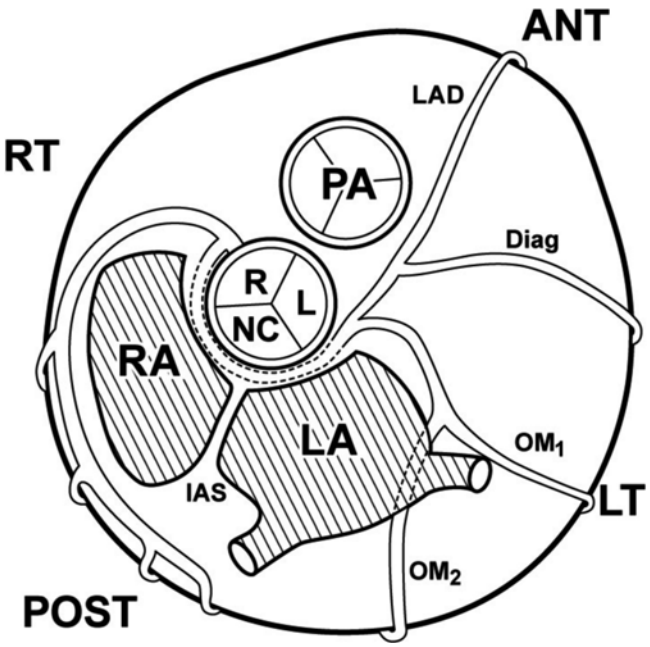

Fig. 13.25 In the *retroaortic course* of the left coronary artery (LCA) arising from the right sinus of Valsalva (RSV), the LCA originates either from the same common trunk that leads to the normal right coronary artery (RCA) or from a site posterior to the RCA. The proximal LCA courses posterior to the aorta, in the space between the bottom of the aortic valve and the mitral annulus, but not inside the aortic-sinus wall (there is no lateral compression or pulsatility in this "intramural" course). More distally, the LCA main trunk runs epicardially, anterior to—and around—the mitral annulus, before separating into the left anterior descending (LAD) and circumflex arteries. Abbreviations as in Fig. 13.24

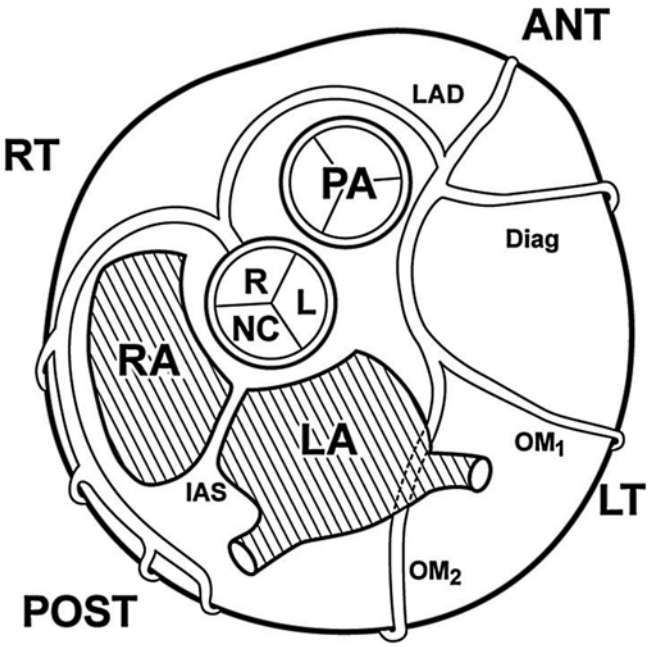

Fig. 13.26 In the *prepulmonic course* of the left coronary artery (LCA), arising from the right sinus of Valsalva (RSV), the ostium is located at the RSV, originating either from a single trunk with the RCA or anterior to the RCA. The left main trunk courses around, and in front of, the pulmonary infundibulum, to reach the anterior interventricular groove and split into the LAD and circumflex arteries. Abbreviations as in Fig. 13.24

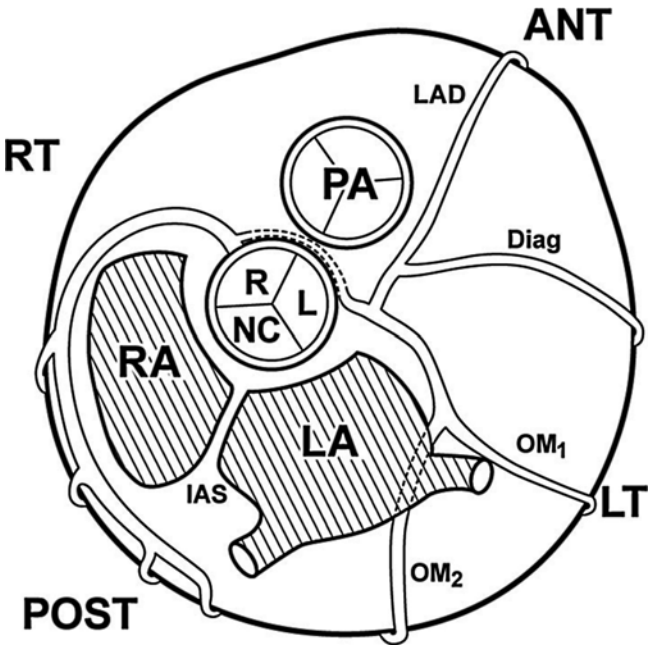

Fig. 13.27 Left coronary artery (LCA) arising from the opposite sinus of Valsalva (*L-ACAOS*; *intramural course*): the left main coronary artery arises from the right sinus of Valsalva (RSV), with—or next to—the right coronary artery. The LCA courses around the aortic wall at the sinutubular sinus (see Figs. 13.23 and 13.32) and is visualized on CMRA as "*between* the aorta and pulmonary artery" (having an "*interarterial course*"). The proximal LCA is indeed "*intramural*" and usually appears laterally compressed on cross-sectional imaging (see Fig. 13.32). Abbreviations as in Fig. 13.24

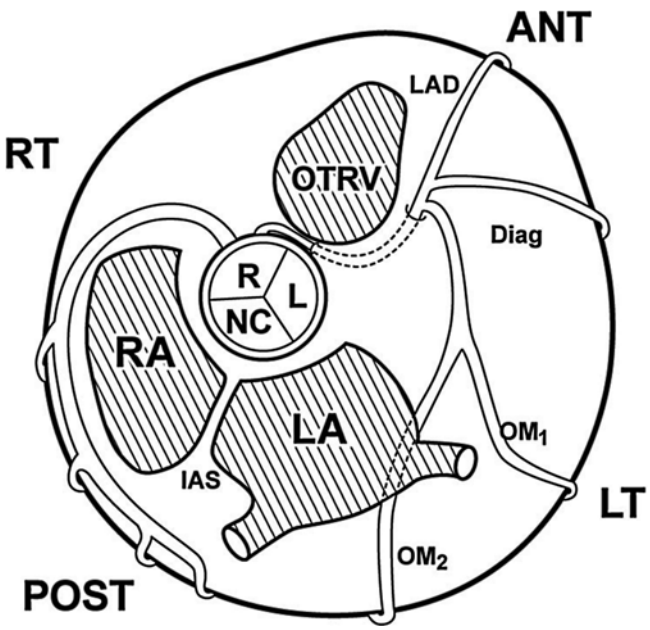

Fig. 13.28 In ectopic left coronary artery (LCA) arising from the right sinus of Valsalva (RSV) with an *intraseptal* course, the LCA originates from a common trunk with the right coronary artery (RCA) (normal origin) or next to the RCA (as in LCA arising from the opposite sinus [L-ACAOS]), but the LCA's course is off the aortic wall, directed anteriorly, and located first inside the right ventricular (RV) outflow tract and then in the upper/middle ventricular septum (see Fig. 13.23). The left coronary system arises from the RSV, either with the RCA or next to it. *OTRV* outflow tract of the right ventricle; other abbreviations as in Fig. 13.24

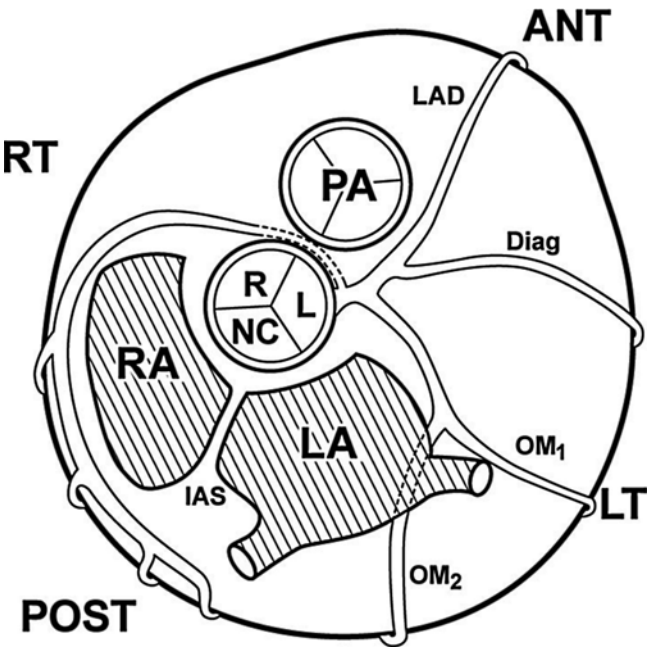

Fig. 13.29 In ectopic origin of the right coronary artery (RCA) from the left sinus of Valsalva (LSV) with an intramural course, the proximal RCA may originate from a common trunk with the normally originating left coronary artery, as in this case. The RCA courses adjacent to the aortic root toward its normal distal location. Lateral compression can best be seen in the longitudinal or sagittal view (along the ascending aorta; see text and Fig. 13.34b)

ally compressed in systole and with exercise, while affected by aortic-wall phasic expansion during the cardiac cycle [289–291]. Unfortunately, such pulsatility of ACAOS vessels is poorly evaluated by CMRA protocols (which routinely show only end-diastolic compression and which lack the temporal and spatial definition for a similar evaluation), whereas the amount of stenosis that results from such mechanisms varies from case to case (Fig. 13.31). The intramural course of an LCA originating from the RSV is clinically and functionally much more important than that seen in cases of anomalous origin of the arteries from the opposite sinus with intraseptal, infundibular, or subpulmonic courses [287–290], which, by themselves, lack intrinsic stenotic effects (see Figs. 13.25, 13.26, and 13.28). Unfortunately, "intraseptal" anomalies are frequently confused with (intramural) ACAOS, partly due to the traditional label of interarterial or "between the aorta and pulmonary artery (*or* infundibulum)." Figures 13.25, 13.26, and 13.28 show the most common benign variants of anomalous origin of the LCA from the opposite sinus. The anterior, retroaortic, subpulmonic, or intraseptal courses are rarely associated with SCD [289–291]. The interarterial course in L-ACAOS is characterized by an LCA that arises either from the RCA or separately from the RSV, following a preaortic and intramural aortic course [283, 289–292], while the intraseptal variety of LCA arising from the RSV can be recognized easily on coronary angiography, CCTA, or CMRA because of the following specific features (Fig. 13.23a):

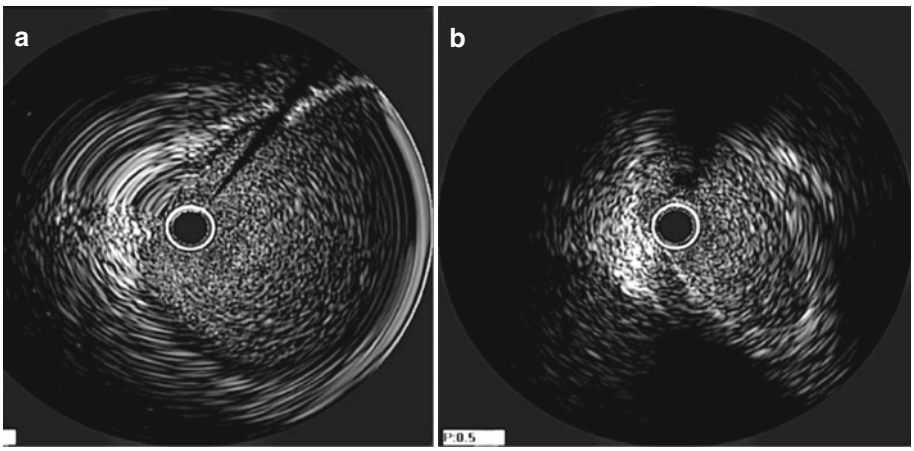

Fig. 13.30 (**a**, **b**) Intravascular ultrasound (IVUS) images obtained in a symptomatic patient with anomalous left coronary artery arising from the opposite sinus of Valsalva (L-ACAOS). (**a**) Distal reference cross-section, with mild atherosclerosis. Intimal thickening related to atherosclerotic build-up is clearly seen in this extramural segment (but is consistently missing in the intramural segment). This extramural segment of the artery is round and has a 3.5-mm uniform diameter, with an area of 19.34 mm^2. (**b**) The proximal most stenotic segment is close to the ostium and shows lateral compression and hypoplasia with respect to the distal segment

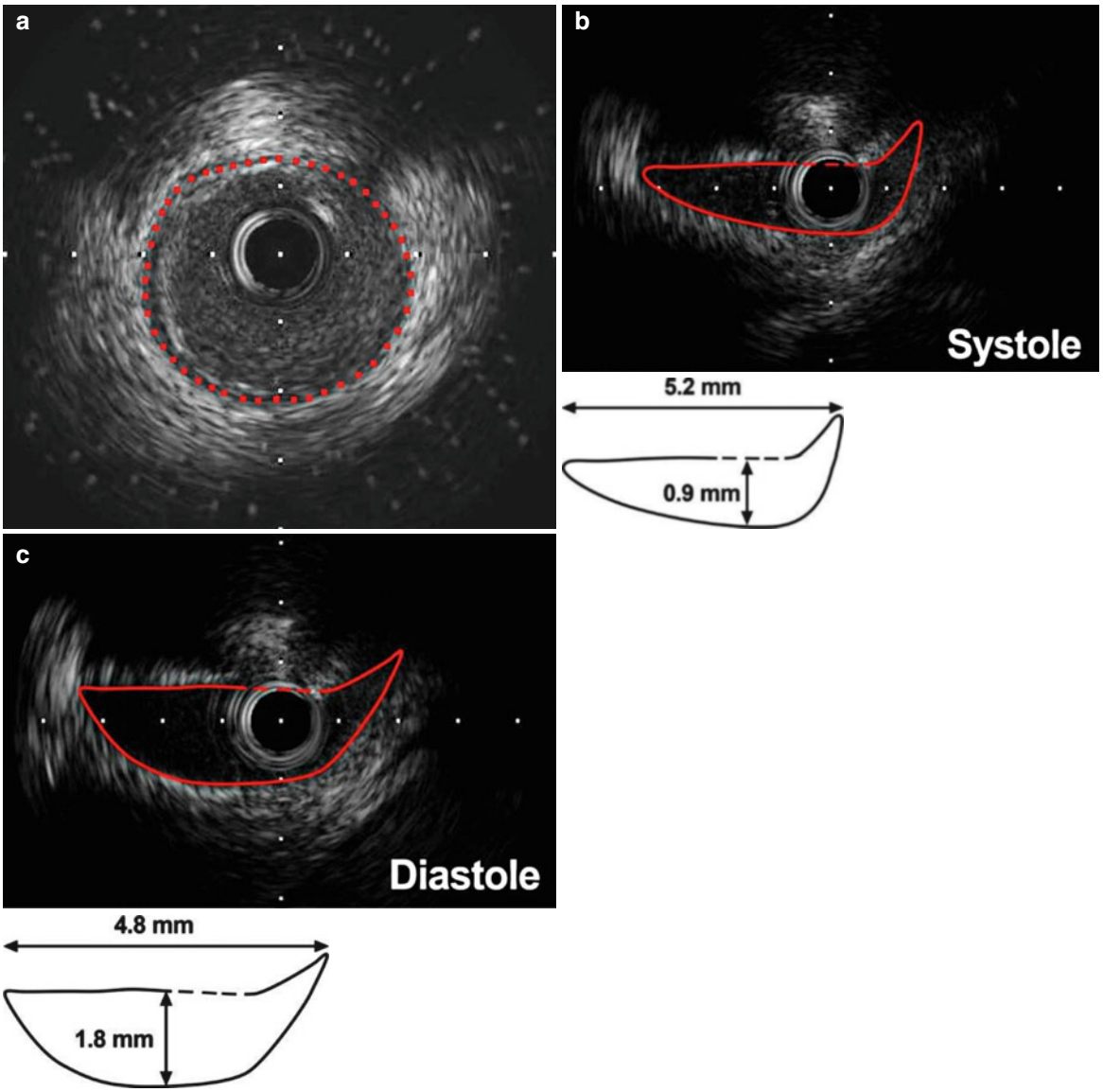

Fig. 13.31 Intravascular ultrasound (IVUS) images in a case of right coronary artery arising from the opposite sinus (R-ACAOS) (see Fig. 13.29) in a patient with atypical chest pain and a negative stress-test result. (**a**) Distal cross-section; (**b**) proximal cross-section, close to the ostium. The cross-sectional proximal area (in view **b**) is fairly well visualized, indicating a smaller size than that of the distal left main trunk (extramural, in view **a**). The short diameter of the proximal section was calculated as being 1.0 mm in systole and 1.8 mm in diastole (in view **c**). The inner edges of the cross-sectional lumen can be precisely visualized with IVUS

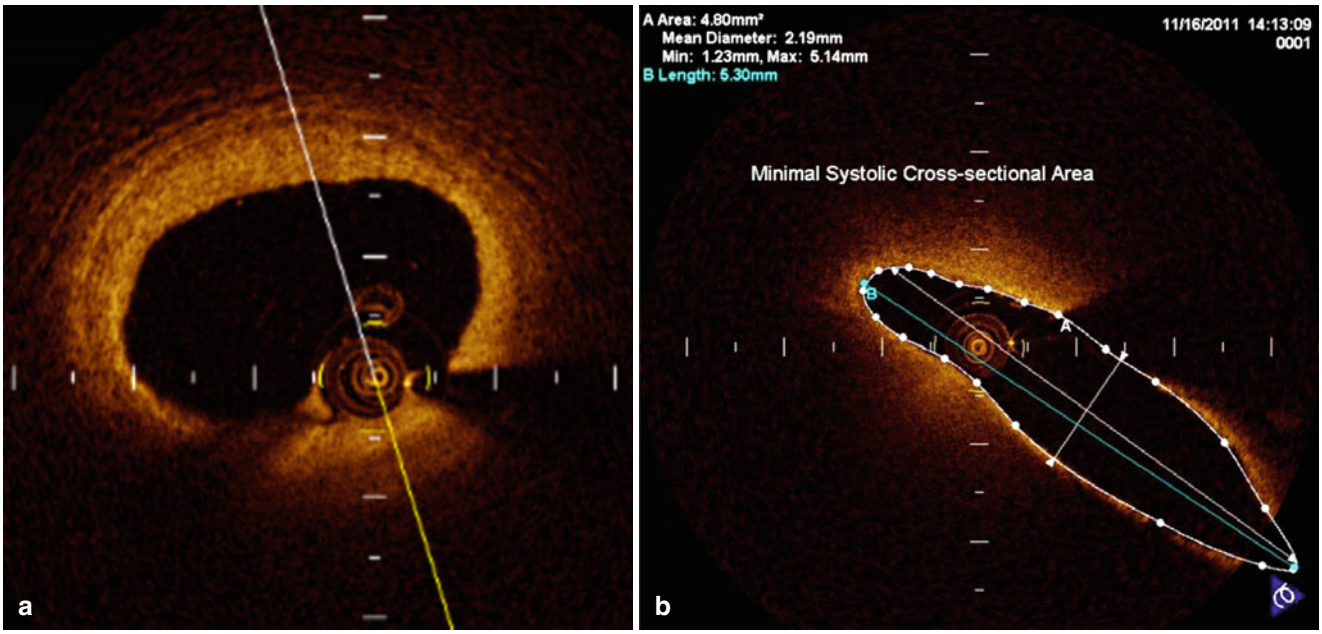

Fig. 13.32 Optical coherence tomographic (OCT) image obtained in a symptomatic patient with an anomalous right coronary artery (RCA) arising from the opposite sinus (R-ACAOS). (**a**) Reference cross-sectional area (CSA) obtained during systole; (**b**) site of the worst ostial stenosis (in systole). The detailed inner edges of the arterial lumen are clearly seen. The long diameter is 5.2 mm, and the short diameter is 0.9–1.2 mm. The CSA is calculated as 4.56 mm^2. Compared to the distal, extramural left main artery, the RCA has a stenosis of about 47 % under resting conditions, but this percentage may increase significantly during exercise (see text). Similar images obtained over the entire duration of a heartbeat (30 frames/min) allowed the most accurate possible depiction of the phasic changes in the CSA at rest and during exercise; for this purpose, OCT was much better than intravascular ultrasound

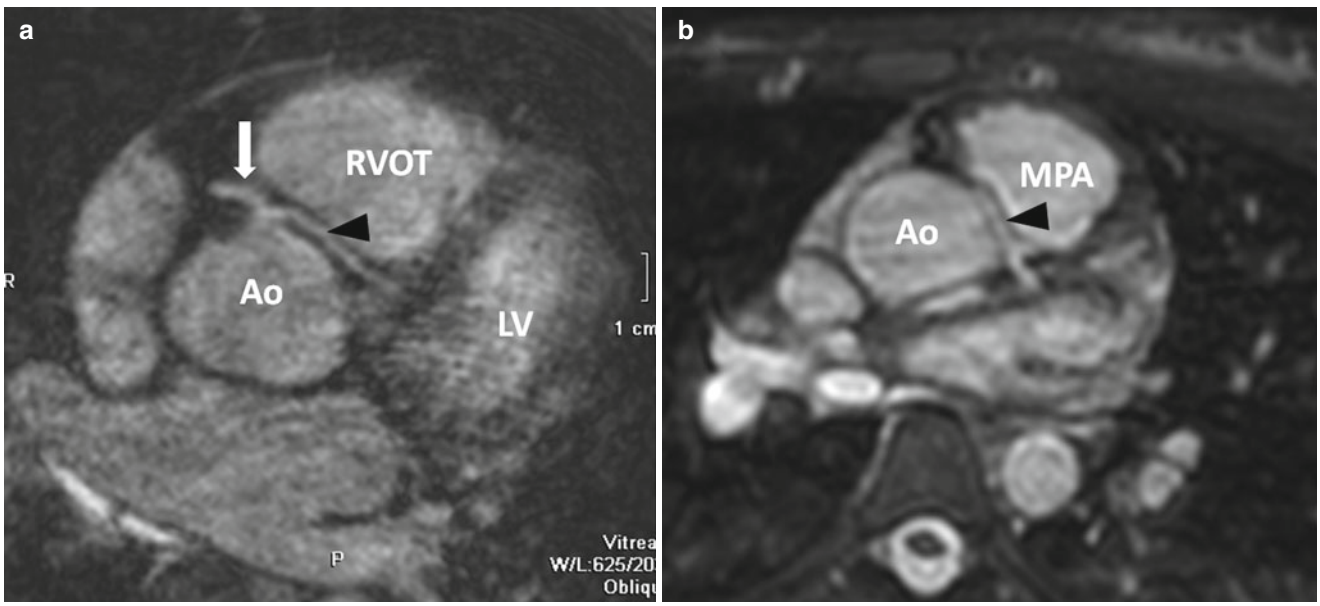

Fig. 13.33 (**a**) Intraseptal course (see Fig. 13.23b). Coronary magnetic resonance angiography (CMRA) of the left coronary artery (LCA) (*black arrowhead*) arising from the right sinus of Valsalva (RSV) from a different ostium than the right coronary artery's (RCA, *white arrow*). Note that the takeoff of the left main artery (LM) is leading away from the aortic wall and is situated between the aortic root (*Ao*) and the right ventricular outflow tract (RVOT), hence the course is *not* interarterial but *intraseptal* (see text). This accidental finding was observed during routine screening in an asymptomatic patient. (**b**) For comparison, an LCA (*black arrowhead*) arising from the opposite sinus of Valsalva (L-ACAOS) with an *intramural course* is shown (see Fig. 13.23a). This course is also called interarterial (see text). The female patient was resuscitated from a cardiac arrest that occurred while she was running in a marathon. *LV* left ventricle, *MPA* main pulmonary artery

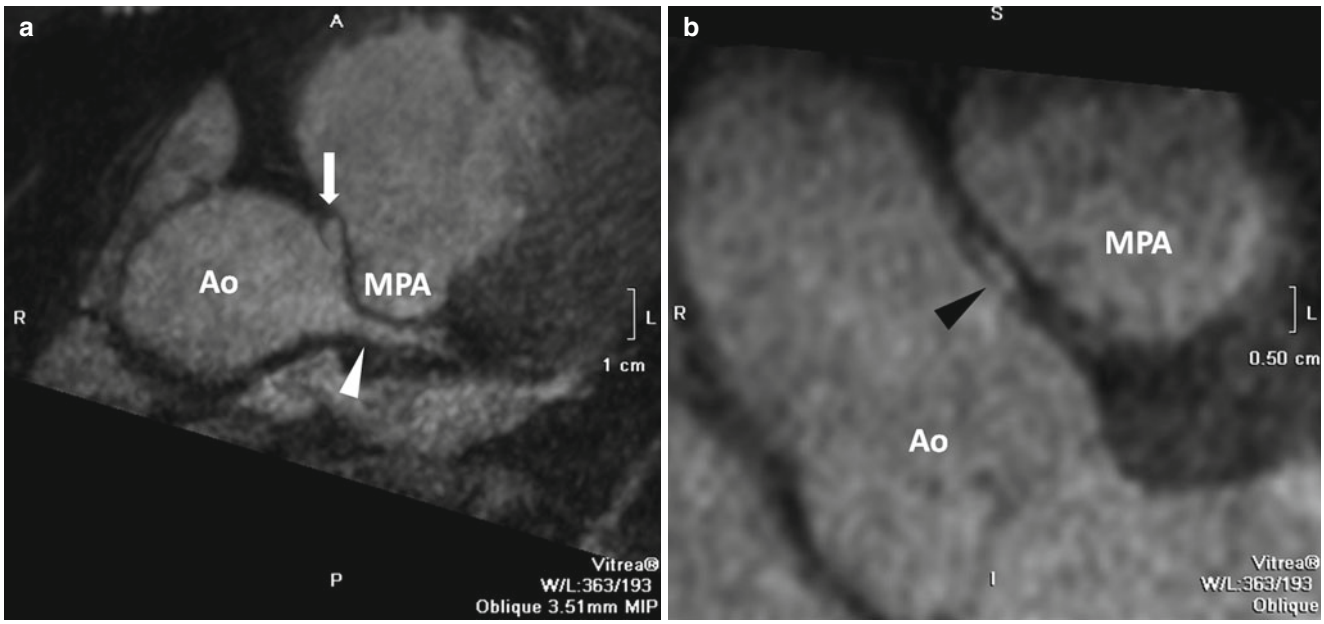

Fig. 13.34 Coronary magnetic resonance angiography (CMRA) of the right coronary artery (RCA) arising from the opposite sinus of Valsalva (R-ACAOS) in a 30-year-old man who presented with exertional chest pain. (**a**) Cross-sectional tomographic plane at the level of the semilunar valves. *White arrowhead* indicates the left main coronary artery, and *white arrow* indicates the right coronary artery. (**b**) Near-"sagittal" tomographic CMRA of the aortic root cuts the roots of the great vessels at their middle (at the level of the aortopulmonary septum), revealing a "between the aorta and pulmonary artery course," with lateral compressive narrowing of the proximal RCA (Fig. 13.23a). This cut is at the level of the anterior commissure (horizontal cross-section) and is known as the "Angelini/Cheong cut." It has been proposed as a fundamental measurement of the severity of proximal obstruction of R-ACAOS (or left-ACAOS); in dedicated studies, this short diameter can be measured fairly precisely in these projections (computed tomography angiography offers a better-defined image and is preferred for evaluating such stenosis; see text). *Black arrowhead* indicates the left coronary artery main trunk. *Ao* aorta, *MPA* main pulmonary artery

- The LCA originates from the RSV—either with, or next to, the RCA—as in the case of an intramural course, but the LMCA trunk then travels anteriorly, inside the supraventricular crista and the upper or mid interventricular septum, and reaches the LAD at the proximal or mid trunk, where the LMCA becomes subepicardial, at the anterior interventricular sulcus (the proximal LAD provides the circumflex trunk).
- The distal portion of the LMCA trunk courses inside the ventricular septum and tends to behave like a myocardial bridge: it may undergo mild systolic compression, and it usually provides a large first septal branch. Such an intraseptal course is generally considered benign and does not require treatment, although some patients with this condition have been erroneously sent to surgery with a confusing diagnosis. (This course is not "between the aorta and pulmonary artery" but runs "from the aorta to the RV infundibulum," away from the aortic wall, as shown in Figs. 13.23 and 13.33).

Like CCTA, CMRA clearly allows a consistent and definitive diagnosis of an intraseptal course, ruling out the dangerous intramural variety (ACAOS). Other abnormal courses of ectopic coronary arteries (prepulmonic, retroaortic, or posterior to the atrioventricular valves) are also quite adequately and consistently identified by CMRA as generic types, even though this imaging technique cannot definitively document the cross-sectional area in a tomographic rendering (which indicates the severity of an individual case).

At the Texas Heart Institute, the Center for Coronary Artery Anomalies has recently been involved in a large, population-based screening study of 10,000 children [283]. This study includes generalized screening by a simplified CMRA protocol essentially designed to identify the prevalence of CAAs, cardiomyopathies, and high-risk electrocardiographic abnormalities in school children [283]. The protocol for this MRI-based screening study includes no intravenous line, Gd infusion, or sedation and involves a shortened acquisition time (approximately 5 min for studying the origin and proximal courses of the coronary arteries). In our initial 1,836 cases, the accuracy and consistency in identifying the proximal coronary anatomy (see the Introduction to this Section) has been in the range of 99 % [283]. Most types of CAAs can be clearly delineated by this method. However, in evaluating the severity of stenosis of the intramural course (a critical clinical necessity), CMRA does not have the space/time resolution necessary to quantify stenosis in such small arteries, which are phasically moving during the cardiac cycle (Table 13.7). Consequently, CMRA

appears to be quite adequate and reliable in the first-stage screening of young populations for an increased risk of SCD (most such deaths in the context of CAAs occur during or after exertion in the young) [283, 291], but neither CMRA nor CCTA is precise enough to guide the clinical management of individual CAAs [291, 292]. The severity of an individual CAA seems to correlate with (1) previous symptoms (chest pain and/or dyspnea with exertion, syncope, cardiac arrest); (2) the results of stress testing (which has a low precision for quantifying risk in the young, due to a high incidence of false positive or negative results); and (3) the severity of stenosis of the ectopic coronary artery at the level of the intramural segment. For this purpose, more-predictive imaging can be performed by evaluating the cross-sectional area of the proximal ectopic vessel on CT-scan angiography [292]. For even more precision, one may (and probably should) in selected cases—involving patients with symptoms, stress-test abnormalities, syncope, or other high-risk characteristics—perform an invasive procedure such as intravascular ultrasonography [291] (Figs. 13.30 and 13.31) or optical coherence tomography (Fig. 13.32). These two techniques are able to provide tomographic cross-sectional images that are, respectively, 10 and 100 times more accurate than CMRA images [293–295].

Other Coronary Artery Anomalies: Imaging and Clinical Relevance

In addition to ACAOS, other CAAs may be found fairly often during screening or diagnostic CMRA in the adolescent or adult population. These entities are sometimes clinically significant but are more often benign. The three most frequent and/or important of them are coronary myocardial bridges (CMBs), coronary-cameral fistulas (CCFs), and anomalous left coronary artery arising from the pulmonary artery (ALCAPA).

Coronary Myocardial Bridges

Coronary myocardial bridges are frequently observed in anatomic, dedicated studies (involving microdissection and histologic imaging) [288], but they are also seen on CCTA, CT scans, or CMRA. In the human heart, a CMB is defined as a proximal coronary artery that is normally epicardial (lying on the surface of the myocardium) but that dips inside the myocardium, becoming compressed during systole (as shown also on angiography). This is a normal anatomic feature in many mammals and birds but is usually considered abnormal or potentially clinically significant in humans [287, 289].

Like CCTA, CMRA can properly identify the more severe forms of CMBs but not the milder forms, in which the bridging myocardium has a thickness of less than 1 mm. Clinical evaluation of the severity of individual CMBs cannot be carried out by using a morphologic, "still" imaging technique (even though these techniques offer the advantage of a tomographic approach that allows visualization of both the coronary vessel and the related myocardial bridge). Typically, CMRA allows only for imaging of the end-diastolic appearance of a CMB (but not phasic systolic narrowing of the coronary lumen, which can theoretically be assumed to impair coronary flow to some degree). Additionally, a routine CMRA study does not properly evaluate CMB thickness unless the tomographic plane is perpendicular to the target segment. Thickness, by itself, does not define the severity of a CMB, which is more likely related to the degree of systolic compression of the coronary lumen adjacent to the CMB, as well as the possibility of an excessive tendency to spasticity [290, 293].

Patients with hypertrophic obstructive cardiomyopathy have the highest probability of showing systolic blanching of the coronary branches (epicardially or intraseptally located). Magnetic resonance imaging is useful for identifying HCM (by the thickness of the septal wall and the free wall and by the pressure gradient at the subaortic stenosis), but it is not likely to identify systolic compression of the small septal branches, as shown by selective angiography. In HCM, such systolic compression could be the most relevant means of inferring the presence of myocardial fiber disarray with obstruction (a potentially important prognostic parameter for the risk of SCD) [291].

Coronary-Cameral Fistulas

Coronary-cameral fistulas are characterized by any type of abnormal coronary termination in any vascular thoracic structure. They are fairly frequent CAAs, which can be identified and evaluated with CMRA. These entities can be subdivided into two types, grossly based on their size [290].

1. *Smaller CCFs* (grossly: having less than 500 mL/min of blood flow) most frequently include two subtypes: (1) those that drain into the proximal pulmonary artery and (2) those that drain into 1 or both ventricles. Both subtypes are generally small in diameter and involve multiple fistulous tracts. The CCFs that drain into the pulmonary artery are easily recognized with CMRA because of their multiple snake-like coronary side-branches that typically originate from 1 or 2 proximal coronary arteries. The multiple micro-CCFs to the ventricles originate from either coronary artery, or both, and drain into the right and/or left apical ventricular portions; they are generally difficult or impossible to recognize on routine CMRA studies. Both subtypes of small CCFs are relatively benign and do not usually require interventional treatment, except in the face of aneurysmal formation in rare

coronary-to-pulmonary forms. The indication for CMRA of such CCFs is mainly related to the possible utility of a tomographic technique for better describing the extent and location of these entities on the pulmonary arterial wall, especially in planning catheter or surgical interventions.

2. *Large CCFs* (more than 500 mL/min of blood flow) terminate into a thoracic cardiovascular cavity (at venous, pulmonary, and atrial or ventricular sites) [291]; indeed, blood flow through such fistulas could range from 500 mL to an amount that equals the total cardiac output, even in infants. In studying large-diameter, high-flow CCFs, the advantage of MRI (rather than CCTA) is the additional capacity to estimate the amount of blood shunting, valvular insufficiency, and reversible myocardial ischemia and/or scar tissue. No doubt, though, because of CCTA's improved anatomic detail, this method is better for studying two critical aspects of CCF: (1) the site(s) of origin and the size and location of the *nutrient branches* arising from the fistulous tract (these branches must be spared during any interventional treatment) and (2) the size of *ectasia/aneurysms*, in addition to mural thrombus and/or coronary stenosis. Establishing the exact size of the fistulous loops' lumen is particularly useful for planning coil embolization treatment of CCF and is best achieved with CCTA. Furthermore, the presence of distal fistulous-tract ostial stenosis (which is occasionally present in older CCF patients) is an important point to be clarified in view of the sometimes difficult decision about coil embolization versus surgical ligation of CCF [290]. The presence of stenosis favors coil embolization, because stenosis is associated with a decreased chance of coil distal embolization (into the pulmonary arteries) in the case of very large fistulas [290].

Anomalous Origin of the Left Coronary Artery from the Pulmonary Artery

In newborns or infants, anomalous origin of the LCA from the pulmonary artery (ALCAPA) is the fundamental entity that can be well diagnosed by CMRA [296–301]. This anomaly is frequently recognized clinically (based on a heart murmur, cardiomegaly, abnormal electrocardiogram, and heart failure) and is quite lethal. Typically, it is first diagnosed early after birth ("infantile-type" ALCAPA), because of the onset of an acute MI when the pulmonary artery pressure decreases, as is normally expected during the first few weeks after birth. Because of the presence of tachycardia, dyspnea, congestive heart failure, and/or shock, CMRA is rarely used in this context. Echocardiography may diagnose the essential features of ALCAPA, indicating the need for emergency surgical treatment of these fragile, unstable (and tachycardic) small patients.

When ALCAPA is discovered at a later age ("adult type"), CMRA may be an attractive means of imaging the anomaly and carrying out a functional study [296–301]. In addition to clearly defining the basic anatomic features of the anomaly, CMRA may be quite useful for assessing LV function (diagnosing reversible ischemia versus scar tissue in different myocardial segments and assessing the global ejection fraction), especially in view of the need for postoperative follow-up testing when recovery of ventricular function is variable in adults.

A particular detail that is useful to surgeons in planning a repair technique is the exact site of origin of the ectopic coronary artery. Usually, ALCAPA arises from the left posterior sinus of the pulmonary valve, but it could also arise from the more distal pulmonary main trunk, the proximal right or left pulmonary branches, the right sinus of the pulmonary valve, or the nonfacing sinus of the pulmonary valve (the anterior one), which may have a juxta-commissural location with an intramural proximal course. These features have possible implications regarding the choice of surgical technique used for repair.

Conclusions

In studying CAAs, MRI/MRA is commonly useful as a screening test in general populations at risk for SCD (such as athletes, military recruits, or patients without a previous diagnosis but with chest pain and/or a positive stress-test result). This modality is also useful as a secondary test in patients with an initial previous diagnosis of CAA, based on inconclusive coronary catheter angiography. Unfortunately, in some anomalies, CMRA does not have the necessary precision to indicate interventional treatment; in particular, it cannot establish the severity of stenosis of the luminal cross-sectional area of relatively small, possibly obstructed vessels, as in ACAOS.

References

1. Pennell DJ, Sechtem UP, Higgins CB, et al. Clinical indications for cardiovascular magnetic resonance (CMR): Consensus Panel report. Eur Heart J. 2004;25(21):1940–65.
2. Hendel RC, Patel MR, Kramer CM, et al. ACCF/ACR/SCCT/SCMR/ASNC/NASCI/SCAI/SIR 2006 appropriateness criteria for cardiac computed tomography and cardiac magnetic resonance imaging: a report of the American College of Cardiology Foundation Quality Strategic Directions Committee Appropriateness Criteria Working Group, American College of Radiology, Society of Cardiovascular Computed Tomography, Society for Cardiovascular Magnetic Resonance, American Society of Nuclear Cardiology, North American Society for Cardiac Imaging, Society for Cardiovascular Angiography and Interventions, and Society of Interventional Radiology. J Am Coll Cardiol. 2006;48(7):1475–97.
3. American College of Cardiology Foundation Task Force on Expert Consensus Documents, Hundley WG, Bluemke DA, Finn JP, et al.

ACCF/ACR/AHA/NASCI/SCMR 2010 expert consensus document on cardiovascular magnetic resonance: a report of the American College of Cardiology Foundation Task Force on Expert Consensus Documents. J Am Coll Cardiol. 2010;55(23):2614–62.
4. Smith SM, Jenkinson M, Woolrich MW, et al. Advances in functional and structural MR image analysis and implementation as FSL. Neuroimage. 2004;23 Suppl 1:S208–19.
5. Russo V, Renzulli M, Buttazzi K, Fattori R. Acquired diseases of the thoracic aorta: role of MRI and MRA. Eur Radiol. 2006;16(4):852–65.
6. Hansen T, Wikstrom J, Eriksson MO, et al. Whole-body magnetic resonance angiography of patients using a standard clinical scanner. Eur Radiol. 2006;16(1):147–53.
7. Hu P, Chan J, Ngo LH, et al. Contrast-enhanced whole-heart coronary MRI with bolus infusion of gadobenate dimeglumine at 1.5 T. Magn Reson Med. 2011;65(2):392–8.
8. Jerosch-Herold M, Seethamraju RT, Swingen CM, Wilke NM, Stillman AE. Analysis of myocardial perfusion MRI. J Magn Reson Imaging. 2004;19(6):758–70.
9. Detre JA, Alsop DC, Vives LR, et al. Noninvasive MRI evaluation of cerebral blood flow in cerebrovascular disease. Neurology. 1998;50(3):633–41.
10. Charles-Edwards EM, deSouza NM. Diffusion-weighted magnetic resonance imaging and its application to cancer. Cancer Imaging. 2006;6:135–43.
11. Kim HW, Lee D, Pohost GM. (31)P cardiovascular magnetic resonance spectroscopy: a unique approach to the assessment of the myocardium. Future Cardiol. 2009;5(6):523–7.
12. Razavi R, Hill DL, Keevil SF, et al. Cardiac catheterisation guided by MRI in children and adults with congenital heart disease. Lancet. 2003;362(9399):1877–82.
13. Zhang L, Chen WZ, Liu YJ, et al. Feasibility of magnetic resonance imaging-guided high intensity focused ultrasound therapy for ablating uterine fibroids in patients with bowel lies anterior to uterus. Eur J Radiol. 2010;73(2):396–403.
14. Meaney TF. Magnetic resonance without nuclear. Radiology. 1984;150(1):277.
15. Pooley RA. AAPM/RSNA physics tutorial for residents: fundamental physics of MR imaging. Radiographics. 2005;25(4):1087–99.
16. Jacobs MA, Ibrahim TS, Ouwerkerk R. AAPM/RSNA physics tutorials for residents: MR imaging: brief overview and emerging applications. Radiographics. 2007;27(4):1213–29.
17. Morelli JN, Runge VM, Ai F, et al. An image-based approach to understanding the physics of MR artifacts. Radiographics. 2011;31(3):849–66.
18. Plewes DB, Kucharczyk W. Physics of MRI: a primer. J Magn Reson Imaging. 2012;35(5):1038–54.
19. Ridgway JP. Cardiovascular magnetic resonance physics for clinicians: part I. J Cardiovasc Magn Reson. 2010;12:71.
20. Zhang H, Maki JH, Prince MR. 3D contrast-enhanced MR angiography. J Magn Reson Imaging. 2007;25(1):13–25.
21. Miyazaki M, Akahane M. Non-contrast enhanced MR angiography: established techniques. J Magn Reson Imaging. 2012;35(1):1–19.
22. Richardson P, McKenna W, Bristow M, et al. Report of the 1995 World Health Organization/International Society and Federation of Cardiology Task Force on the Definition and Classification of cardiomyopathies. Circulation. 1996;93(5):841–2.
23. Elliott P, Andersson B, Arbustini E, et al. Classification of the cardiomyopathies: a position statement from the European Society Of Cardiology Working Group on Myocardial and Pericardial Diseases. Eur Heart J. 2008;29(2):270–6.
24. World Health Organization. Http://www.Who.Int/mediacentre/factsheets/fs317/en/index.Html.
25. Scanlon PJ, Faxon DP, Audet AM, et al. ACC/AHA guidelines for coronary angiography: executive summary and recommendations. A report of the American College of Cardiology/American Heart Association Task Force on Practice Guidelines (Committee on Coronary Angiography) developed in collaboration with the Society for Cardiac Angiography and Interventions. Circulation. 1999;99(17):2345–57.
26. Douglas PS, Khandheria B, Stainback RF, et al. ACCF/ASE/ACEP/AHA/ASNC/SCAI/SCCT/SCMR 2008 appropriateness criteria for stress echocardiography: a report of the American College of Cardiology Foundation Appropriateness Criteria Task Force, American Society of Echocardiography, American College of Emergency Physicians, American Heart Association, American Society of Nuclear Cardiology, Society for Cardiovascular Angiography and Interventions, Society of Cardiovascular Computed Tomography, and Society for Cardiovascular Magnetic Resonance endorsed by the Heart Rhythm Society and the Society of Critical Care Medicine. J Am Coll Cardiol. 2008;51(11):1127–47.
27. Hendel RC, Berman DS, Di Carli MF, et al. ACCF/ASNC/ACR/AHA/ASE/SCCT/SCMR/SNM 2009 Appropriate Use Criteria for Cardiac Radionuclide Imaging: A Report of the American College of Cardiology Foundation Appropriate Use Criteria Task Force, the American Society of Nuclear Cardiology, the American College of Radiology, the American Heart Association, the American Society of Echocardiography, the Society of Cardiovascular Computed Tomography, the Society for Cardiovascular Magnetic Resonance, and the Society of Nuclear Medicine. J Am Coll Cardiol. 2009;53(23):2201–29.
28. Cheong BY, Muthupillai R, Wilson JM, et al. Prognostic significance of delayed-enhancement magnetic resonance imaging: survival of 857 patients with and without left ventricular dysfunction. Circulation. 2009;120(21):2069–76.
29. Jahnke C, Nagel E, Gebker R, et al. Prognostic value of cardiac magnetic resonance stress tests: adenosine stress perfusion and dobutamine stress wall motion imaging. Circulation. 2007;115(13):1769–76.
30. Ingkanisorn WP, Kwong RY, Bohme NS, et al. Prognosis of negative adenosine stress magnetic resonance in patients presenting to an emergency department with chest pain. J Am Coll Cardiol. 2006;47(7):1427–32.
31. Manning WJ, Atkinson DJ, Grossman W, Paulin S, Edelman RR. First-pass nuclear magnetic resonance imaging studies using gadolinium-DTPA in patients with coronary artery disease. J Am Coll Cardiol. 1991;18(4):959–65.
32. Klocke FJ, Baird MG, Lorell BH, et al. ACC/AHA/ASNC guidelines for the clinical use of cardiac radionuclide imaging—executive summary: a report of the American College of Cardiology/American Heart Association Task Force on Practice Guidelines (ACC/AHA/ASNC Committee to Revise the 1995 Guidelines for the Clinical Use of Cardiac Radionuclide Imaging). Circulation. 2003;108(11):1404–18.
33. Lee DC, Simonetti OP, Harris KR, et al. Magnetic resonance versus radionuclide pharmacological stress perfusion imaging for flow-limiting stenoses of varying severity. Circulation. 2004;110(1):58–65.
34. Klem I, Heitner JF, Shah DJ, et al. Improved detection of coronary artery disease by stress perfusion cardiovascular magnetic resonance with the use of delayed enhancement infarction imaging. J Am Coll Cardiol. 2006;47(8):1630–8.
35. Nesto RW, Kowalchuk GJ. The ischemic cascade: temporal sequence of hemodynamic, electrocardiographic and symptomatic expressions of ischemia. Am J Cardiol. 1987;59(7):23C–30.
36. Al Jaroudi W, Iskandrian AE. Regadenoson: a new myocardial stress agent. J Am Coll Cardiol. 2009;54(13):1123–30.
37. Cheong BY, Muthupillai R. Nephrogenic systemic fibrosis: a concise review for cardiologists. Tex Heart Inst J. 2010;37(5):508–15.
38. Wilke NM, Jerosch-Herold M, Zenovich A, Stillman AE. Magnetic resonance first-pass myocardial perfusion imaging: clinical validation and future applications. J Magn Reson Imaging. 1999;10(5):676–85.

39. Wolff SD, Schwitter J, Coulden R, et al. Myocardial first-pass perfusion magnetic resonance imaging: a multicenter dose-ranging study. Circulation. 2004;110(6):732–7.
40. Schwitter J, Wacker CM, van Rossum AC, et al. MR-IMPACT: comparison of perfusion-cardiac magnetic resonance with single-photon emission computed tomography for the detection of coronary artery disease in a multicentre, multivendor, randomized trial. Eur Heart J. 2008;29(4):480–9.
41. Schwitter J, Wacker CM, Wilke N, et al. MR-IMPACT II: Magnetic Resonance Imaging for Myocardial Perfusion Assessment in Coronary artery disease Trial: perfusion-cardiac magnetic resonance vs. single-photon emission computed tomography for the detection of coronary artery disease: a comparative multicentre, multivendor trial. Eur Heart J. 2013;34(10):775–81.
42. Donahue KM, Weisskoff RM, Burstein D. Water diffusion and exchange as they influence contrast enhancement. J Magn Reson Imaging. 1997;7(1):102–10.
43. Jerosch-Herold M, Muehling O. Stress perfusion magnetic resonance imaging of the heart. Top Magn Reson Imaging. 2008;19(1):33–42.
44. Schwitter J. Myocardial perfusion imaging by cardiac magnetic resonance. J Nucl Cardiol. 2006;13(6):841–54.
45. Wang Y, Moin K, Akinboboye O, Reichek N. Myocardial first pass perfusion: steady-state free precession versus spoiled gradient echo and segmented echo planar imaging. Magn Reson Med. 2005;54(5):1123–9.
46. Cheng AS, Pegg TJ, Karamitsos TD, et al. Cardiovascular magnetic resonance perfusion imaging at 3-tesla for the detection of coronary artery disease: a comparison with 1.5-tesla. J Am Coll Cardiol. 2007;49(25):2440–9.
47. Manka R, Vitanis V, Boesiger P, et al. Clinical feasibility of accelerated, high spatial resolution myocardial perfusion imaging. JACC Cardiovasc Imaging. 2010;3(7):710–7.
48. Motwani M, Maredia N, Fairbairn TA, et al. High-resolution versus standard-resolution cardiovascular MR myocardial perfusion imaging for the detection of coronary artery disease. Circ Cardiovasc Imaging. 2012;5(3):306–13.
49. Hamon M, Fau G, Nee G, Ehtisham J, Morello R. Meta-analysis of the diagnostic performance of stress perfusion cardiovascular magnetic resonance for detection of coronary artery disease. J Cardiovasc Magn Reson. 2010;12(1):29.
50. Greenwood JP, Maredia N, Younger JF, et al. Cardiovascular magnetic resonance and single-photon emission computed tomography for diagnosis of coronary heart disease (CE-MARC): a prospective trial. Lancet. 2012;379(9814):453–60.
51. Nagel E, Klein C, Paetsch I, et al. Magnetic resonance perfusion measurements for the noninvasive detection of coronary artery disease. Circulation. 2003;108(4):432–7.
52. Klocke FJ, Simonetti OP, Judd RM, et al. Limits of detection of regional differences in vasodilated flow in viable myocardium by first-pass magnetic resonance perfusion imaging. Circulation. 2001;104(20):2412–6.
53. Sourbron S. Technical aspects of MR perfusion. Eur J Radiol. 2010;76(3):304–13.
54. Christian TF, Aletras AH, Arai AE. Estimation of absolute myocardial blood flow during first-pass MR perfusion imaging using a dual-bolus injection technique: comparison to single-bolus injection method. J Magn Reson Imaging. 2008;27(6):1271–7.
55. Pack NA, DiBella EV, Rust TC, et al. Estimating myocardial perfusion from dynamic contrast-enhanced CMR with a model-independent deconvolution method. J Cardiovasc Magn Reson. 2008;10:52.
56. Effects of enalapril on mortality in severe congestive heart failure. Results of the Cooperative North Scandinavian Enalapril Survival Study (CONSENSUS). The CONSENSUS Trial Study Group. N Engl J Med. 1987;316(23):1429–35.
57. Effect of enalapril on survival in patients with reduced left ventricular ejection fractions and congestive heart failure. The SOLVD Investigators. N Engl J Med. 1991;325(5):293–302.
58. Allman KC, Shaw LJ, Hachamovitch R, Udelson JE. Myocardial viability testing and impact of revascularization on prognosis in patients with coronary artery disease and left ventricular dysfunction: a meta-analysis. J Am Coll Cardiol. 2002;39(7):1151–8.
59. Bax JJ, Poldermans D, Elhendy A, et al. Improvement of left ventricular ejection fraction, heart failure symptoms and prognosis after revascularization in patients with chronic coronary artery disease and viable myocardium detected by dobutamine stress echocardiography. J Am Coll Cardiol. 1999;34(1):163–9.
60. Gerber BL, Rousseau MF, Ahn SA, et al. Prognostic value of myocardial viability by delayed-enhanced magnetic resonance in patients with coronary artery disease and low ejection fraction: impact of revascularization therapy. J Am Coll Cardiol. 2012;59(9):825–35.
61. Schinkel AF, Bax JJ, Poldermans D, et al. Hibernating myocardium: diagnosis and patient outcomes. Curr Probl Cardiol. 2007;32(7):375–410.
62. Carluccio E, Biagioli P, Alunni G, et al. Patients with hibernating myocardium show altered left ventricular volumes and shape, which revert after revascularization: evidence that dyssynergy might directly induce cardiac remodeling. J Am Coll Cardiol. 2006;47(5):969–77.
63. Rahimtoola SH, Dilsizian V, Kramer CM, Marwick TH, Vanoverschelde JL. Chronic ischemic left ventricular dysfunction: from pathophysiology to imaging and its integration into clinical practice. JACC Cardiovasc Imaging. 2008;1(4):536–55.
64. Mahrholdt H, Wagner A, Judd RM, Sechtem U, Kim RJ. Delayed enhancement cardiovascular magnetic resonance assessment of non-ischaemic cardiomyopathies. Eur Heart J. 2005;26(15):1461–74.
65. Simonetti OP, Kim RJ, Fieno DS, et al. An improved MR imaging technique for the visualization of myocardial infarction. Radiology. 2001;218(1):215–23.
66. Kim RJ, Fieno DS, Parrish TB, et al. Relationship of MRI delayed contrast enhancement to irreversible injury, infarct age, and contractile function. Circulation. 1999;100(19):1992–2002.
67. Kim RJ, Wu E, Rafael A, et al. The use of contrast-enhanced magnetic resonance imaging to identify reversible myocardial dysfunction. N Engl J Med. 2000;343(20):1445–53.
68. Schvartzman PR, Srichai MB, Grimm RA, et al. Nonstress delayed-enhancement magnetic resonance imaging of the myocardium predicts improvement of function after revascularization for chronic ischemic heart disease with left ventricular dysfunction. Am Heart J. 2003;146(3):535–41.
69. Selvanayagam JB, Kardos A, Francis JM, et al. Value of delayed-enhancement cardiovascular magnetic resonance imaging in predicting myocardial viability after surgical revascularization. Circulation. 2004;110(12):1535–41.
70. Kellman P, Arai AE, McVeigh ER, Aletras AH. Phase-sensitive inversion recovery for detecting myocardial infarction using gadolinium-delayed hyperenhancement. Magn Reson Med. 2002;47(2):372–83.
71. Rizzello V, Schinkel AF, Bax JJ, et al. Individual prediction of functional recovery after coronary revascularization in patients with ischemic cardiomyopathy: the scar-to-biphasic model. Am J Cardiol. 2003;91(12):1406–9.
72. Schinkel AF, Poldermans D, Rizzello V, et al. Why do patients with ischemic cardiomyopathy and a substantial amount of viable myocardium not always recover in function after revascularization? J Thorac Cardiovasc Surg. 2004;127(2):385–90.
73. Rahimtoola SH, La Canna G, Ferrari R. Hibernating myocardium: another piece of the puzzle falls into place. J Am Coll Cardiol. 2006;47(5):978–80.
74. Glaveckaite S, Valeviciene N, Palionis D, et al. Value of scar imaging and inotropic reserve combination for the prediction of

segmental and global left ventricular functional recovery after revascularisation. J Cardiovasc Magn Reson. 2011;13:35.
75. Wellnhofer E, Olariu A, Klein C, et al. Magnetic resonance low-dose dobutamine test is superior to SCAR quantification for the prediction of functional recovery. Circulation. 2004; 109(18):2172–4.
76. Jaffe R, Dick A, Strauss BH. Prevention and treatment of microvascular obstruction-related myocardial injury and coronary no-reflow following percutaneous coronary intervention: a systematic approach. JACC Cardiovasc Interv. 2010;3(7):695–704.
77. de Waha S, Desch S, Eitel I, et al. Impact of early vs. late microvascular obstruction assessed by magnetic resonance imaging on long-term outcome after ST-elevation myocardial infarction: a comparison with traditional prognostic markers. Eur Heart J. 2010;31(21):2660–8.
78. Mather AN, Lockie T, Nagel E, et al. Appearance of microvascular obstruction on high resolution first-pass perfusion, early and late gadolinium enhancement CMR in patients with acute myocardial infarction. J Cardiovasc Magn Reson. 2009;11:33.
79. Hombach V, Grebe O, Merkle N, et al. Sequelae of acute myocardial infarction regarding cardiac structure and function and their prognostic significance as assessed by magnetic resonance imaging. Eur Heart J. 2005;26(6):549–57.
80. Cochet AA, Lorgis L, Lalande A, et al. Major prognostic impact of persistent microvascular obstruction as assessed by contrast-enhanced cardiac magnetic resonance in reperfused acute myocardial infarction. Eur Radiol. 2009;19(9):2117–26.
81. Yan AT, Gibson CM, Larose E, et al. Characterization of microvascular dysfunction after acute myocardial infarction by cardiovascular magnetic resonance first-pass perfusion and late gadolinium enhancement imaging. J Cardiovasc Magn Reson. 2006;8(6):831–7.
82. Lund GK, Stork A, Saeed M, et al. Acute myocardial infarction: evaluation with first-pass enhancement and delayed enhancement MR imaging compared with 201Tl SPECT imaging. Radiology. 2004;232(1):49–57.
83. Raff GL, O'Neill WW, Gentry RE, et al. Microvascular obstruction and myocardial function after acute myocardial infarction: assessment by using contrast-enhanced cine MR imaging. Radiology. 2006;240(2):529–36.
84. Wu KC, Zerhouni EA, Judd RM, et al. Prognostic significance of microvascular obstruction by magnetic resonance imaging in patients with acute myocardial infarction. Circulation. 1998;97(8):765–72.
85. Kwong RY, Chan AK, Brown KA, et al. Impact of unrecognized myocardial scar detected by cardiac magnetic resonance imaging on event-free survival in patients presenting with signs or symptoms of coronary artery disease. Circulation. 2006;113(23):2733–43.
86. Klem I, Shah DJ, White RD, et al. Prognostic value of routine cardiac magnetic resonance assessment of left ventricular ejection fraction and myocardial damage: an international, multicenter study. Circ Cardiovasc Imaging. 2011;4(6):610–9.
87. Bello D, Fieno DS, Kim RJ, et al. Infarct morphology identifies patients with substrate for sustained ventricular tachycardia. J Am Coll Cardiol. 2005;45(7):1104–8.
88. de Bakker JM, van Capelle FJ, Janse MJ, et al. Reentry as a cause of ventricular tachycardia in patients with chronic ischemic heart disease: electrophysiologic and anatomic correlation. Circulation. 1988;77(3):589–606.
89. Klem I, Weinsaft JW, Bahnson TD, et al. Assessment of myocardial scarring improves risk stratification in patients evaluated for cardiac defibrillator implantation. J Am Coll Cardiol. 2012;60(5):408–20.
90. Scott PA, Morgan JM, Carroll N, et al. The extent of left ventricular scar quantified by late gadolinium enhancement MRI is associated with spontaneous ventricular arrhythmias in patients with coronary artery disease and implantable cardioverter-defibrillators. Circ Arrhythm Electrophysiol. 2011;4(3):324–30.
91. Lowe JE, Reimer KA, Jennings RB. Experimental infarct size as a function of the amount of myocardium at risk. Am J Pathol. 1978;90(2):363–79.
92. Friedrich MG, Sechtem U, Schulz-Menger J, et al. Cardiovascular magnetic resonance in myocarditis: a JACC White Paper. J Am Coll Cardiol. 2009;53(17):1475–87.
93. Eitel I, Desch S, Fuernau G, et al. Prognostic significance and determinants of myocardial salvage assessed by cardiovascular magnetic resonance in acute reperfused myocardial infarction. J Am Coll Cardiol. 2010;55(22):2470–9.
94. Ugander M, Bagi PS, Oki AJ, et al. Myocardial edema as detected by pre-contrast T1 and T2 CMR delineates area at risk associated with acute myocardial infarction. JACC Cardiovasc Imaging. 2012;5(6):596–603.
95. Abdel-Aty H, Cocker M, Meek C, Tyberg JV, Friedrich MG. Edema as a very early marker for acute myocardial ischemia: a cardiovascular magnetic resonance study. J Am Coll Cardiol. 2009;53(14):1194–201.
96. Friedrich MG, Abdel-Aty H, Taylor A, et al. The salvaged area at risk in reperfused acute myocardial infarction as visualized by cardiovascular magnetic resonance. J Am Coll Cardiol. 2008;51(16):1581–7.
97. Raman SV, Simonetti OP, Winner 3rd MW, et al. Cardiac magnetic resonance with edema imaging identifies myocardium at risk and predicts worse outcome in patients with non-ST-segment elevation acute coronary syndrome. J Am Coll Cardiol. 2010;55(22):2480–8.
98. Larose E, Rodes-Cabau J, Pibarot P, et al. Predicting late myocardial recovery and outcomes in the early hours of ST-segment elevation myocardial infarction traditional measures compared with microvascular obstruction, salvaged myocardium, and necrosis characteristics by cardiovascular magnetic resonance. J Am Coll Cardiol. 2010;55(22):2459–69.
99. Eitel I, Desch S, de Waha S, et al. Long-term prognostic value of myocardial salvage assessed by cardiovascular magnetic resonance in acute reperfused myocardial infarction. Heart. 2011;97(24):2038–45.
100. Masci PG, Ganame J, Strata E, et al. Myocardial salvage by CMR correlates with LV remodeling and early ST-segment resolution in acute myocardial infarction. JACC Cardiovasc Imaging. 2010;3(1):45–51.
101. Wince WB, Kim RJ. Molecular imaging: T2-weighted CMR of the area at risk—a risky business? Nature reviews. Cardiology. 2010;7(10):547–9.
102. Aletras AH, Kellman P, Derbyshire JA, Arai AE. ACUT2E TSE-SSFP: a hybrid method for T2-weighted imaging of edema in the heart. Magn Reson Med. 2008;59(2):229–35.
103. Kellman P, Aletras AH, Mancini C, McVeigh ER, Arai AE. T2-prepared SSFP improves diagnostic confidence in edema imaging in acute myocardial infarction compared to turbo spin echo. Magn Reson Med. 2007;57(5):891–7.
104. Giri S, Chung YC, Merchant A, et al. T2 quantification for improved detection of myocardial edema. J Cardiovasc Magn Reson. 2009;11:56.
105. Kellman P, Hernando D, Shah S, et al. Multiecho dixon fat and water separation method for detecting fibrofatty infiltration in the myocardium. Magn Reson Med. 2009;61(1):215–21.
106. Dixon WT. Simple proton spectroscopic imaging. Radiology. 1984;153(1):189–94.
107. Bley TA, Wieben O, Francois CJ, Brittain JH, Reeder SB. Fat and water magnetic resonance imaging. J Magn Reson Imaging. 2010;31(1):4–18.
108. Rossi MA. Pathologic fibrosis and connective tissue matrix in left ventricular hypertrophy due to chronic arterial hypertension in humans. J Hypertens. 1998;16(7):1031–41.
109. Conrad CH, Brooks WW, Hayes JA, et al. Myocardial fibrosis and stiffness with hypertrophy and heart failure in the spontaneously hypertensive rat. Circulation. 1995;91(1):161–70.

110. Frank JS, Langer GA. The myocardial interstitium: its structure and its role in ionic exchange. J Cell Biol. 1974;60(3):586–601.
111. Maceira AM, Joshi J, Prasad SK, et al. Cardiovascular magnetic resonance in cardiac amyloidosis. Circulation. 2005;111(2): 186–93.
112. White SK, Sado DM, Flett AS, Moon JC. Characterising the myocardial interstitial space: the clinical relevance of non-invasive imaging. Heart. 2012;98(10):773–9.
113. Ugander M, Oki AJ, Hsu LY, et al. Extracellular volume imaging by magnetic resonance imaging provides insights into overt and sub-clinical myocardial pathology. Eur Heart J. 2012;33(10):1268–78.
114. Garcia-Dorado D, Andres-Villarreal M, Ruiz-Meana M, Inserte J, Barba I. Myocardial edema: a translational view. J Mol Cell Cardiol. 2012;52(5):931–9.
115. Desai KV, Laine GA, Stewart RH, et al. Mechanics of the left ventricular myocardial interstitium: effects of acute and chronic myocardial edema. Am J Physiol Heart Circ Physiol. 2008; 294(6):H2428–34.
116. Anderson LJ, Holden S, Davis B, et al. Cardiovascular T2-star (T2*) magnetic resonance for the early diagnosis of myocardial iron overload. Eur Heart J. 2001;22(23):2171–9.
117. Anderson LJ. Assessment of iron overload with T2* magnetic resonance imaging. Prog Cardiovasc Dis. 2011;54(3):287–94.
118. He T, Gatehouse PD, Smith GC, et al. Myocardial T2* measurements in iron-overloaded thalassemia: an in vivo study to investigate optimal methods of quantification. Magn Reson Med. 2008;60(5):1082–9.
119. He T, Gatehouse PD, Kirk P, et al. Black-blood T2* technique for myocardial iron measurement in thalassemia. J Magn Reson Imaging. 2007;25(6):1205–9.
120. Carpenter JP, He T, Kirk P, et al. On T2* magnetic resonance and cardiac iron. Circulation. 2011;123(14):1519–28.
121. Magnani JW, Dec GW. Myocarditis: current trends in diagnosis and treatment. Circulation. 2006;113(6):876–90.
122. Fuster V, Gersh BJ, Giuliani ER, et al. The natural history of idiopathic dilated cardiomyopathy. Am J Cardiol. 1981;47(3):525–31.
123. Calabrese F, Basso C, Carturan E, Valente M, Thiene G. Arrhythmogenic right ventricular cardiomyopathy/dysplasia: is there a role for viruses? Cardiovasc Pathol. 2006;15(1):11–7.
124. Abdel-Aty H, Boye P, Zagrosek A, et al. Diagnostic performance of cardiovascular magnetic resonance in patients with suspected acute myocarditis: comparison of different approaches. J Am Coll Cardiol. 2005;45(11):1815–22.
125. Stensaeth KH, Hoffmann P, Fossum E, et al. Cardiac magnetic resonance visualizes acute and chronic myocardial injuries in myocarditis. Int J Cardiovasc Imaging. 2012;28(2):327–35.
126. Mahrholdt H, Goedecke C, Wagner A, et al. Cardiovascular magnetic resonance assessment of human myocarditis: a comparison to histology and molecular pathology. Circulation. 2004;109(10):1250–8.
127. Kellman P, Wilson JR, Xue H, et al. Extracellular volume fraction mapping in the myocardium, part 2: initial clinical experience. J Cardiovasc Magn Reson. 2012;14:64.
128. Mahrholdt H, Wagner A, Deluigi CC, et al. Presentation, patterns of myocardial damage, and clinical course of viral myocarditis. Circulation. 2006;114(15):1581–90.
129. Basso C, Corrado D, Marcus FI, Nava A, Thiene G. Arrhythmogenic right ventricular cardiomyopathy. Lancet. 2009;373(9671):1289–300.
130. Marcus FI, McKenna WJ, Sherrill D, et al. Diagnosis of arrhythmogenic right ventricular cardiomyopathy/dysplasia: proposed modification of the task force criteria. Circulation. 2010;121(13):1533–41.
131. McKenna WJ, Thiene G, Nava A, et al. Diagnosis of arrhythmogenic right ventricular dysplasia/cardiomyopathy. Task Force of the Working Group Myocardial and Pericardial Disease of the European Society of Cardiology and of the Scientific Council on Cardiomyopathies of the International Society and Federation of Cardiology. Br Heart J. 1994;71(3):215–8.
132. Tansey DK, Aly Z, Sheppard MN. Fat in the right ventricle of the normal heart. Histopathology. 2005;46(1):98–104.
133. Castillo E, Tandri H, Rodriguez ER, et al. Arrhythmogenic right ventricular dysplasia: ex vivo and in vivo fat detection with black-blood MR imaging. Radiology. 2004;232(1):38–48.
134. Marcus FI, Fontaine GH, Guiraudon G, et al. Right ventricular dysplasia: a report of 24 adult cases. Circulation. 1982;65(2):384–98.
135. Kayser HW, van der Wall EE, Sivananthan MU, et al. Diagnosis of arrhythmogenic right ventricular dysplasia: a review. Radiographics. 2002;22(3):639–48; discussion 649–50.
136. Dalal D, Tandri H, Judge DP, et al. Morphologic variants of familial arrhythmogenic right ventricular dysplasia/cardiomyopathy a genetics-magnetic resonance imaging correlation study. J Am Coll Cardiol. 2009;53(15):1289–99.
137. Tandri H, Saranathan M, Rodriguez ER, et al. Noninvasive detection of myocardial fibrosis in arrhythmogenic right ventricular cardiomyopathy using delayed-enhancement magnetic resonance imaging. J Am Coll Cardiol. 2005;45(1):98–103.
138. Grosse-Wortmann L, Macgowan CK, Vidarsson L, Yoo SJ. Late gadolinium enhancement of the right ventricular myocardium: is it really different from the left ? J Cardiovasc Magn Reson. 2008;10:20.
139. Maron BJ. Hypertrophic cardiomyopathy: a systematic review. JAMA. 2002;287(10):1308–20.
140. Gersh BJ, Maron BJ, Bonow RO, et al. 2011 ACCF/AHA guideline for the diagnosis and treatment of hypertrophic cardiomyopathy: a report of the American College of Cardiology Foundation/American Heart Association Task Force on Practice Guidelines. Developed in collaboration with the American Association for Thoracic Surgery, American Society of Echocardiography, American Society of Nuclear Cardiology, Heart Failure Society of America, Heart Rhythm Society, Society for Cardiovascular Angiography and Interventions, and Society of Thoracic Surgeons. J Am Coll Cardiol. 2011;58(25):e212–60.
141. Rickers C, Wilke NM, Jerosch-Herold M, et al. Utility of cardiac magnetic resonance imaging in the diagnosis of hypertrophic cardiomyopathy. Circulation. 2005;112(6):855–61.
142. Maron MS, Maron BJ, Harrigan C, et al. Hypertrophic cardiomyopathy phenotype revisited after 50 years with cardiovascular magnetic resonance. J Am Coll Cardiol. 2009;54(3) :220–8.
143. Chun EJ, Choi SI, Jin KN, et al. Hypertrophic cardiomyopathy: assessment with MR imaging and multidetector CT. Radiographics. 2010;30(5):1309–28.
144. Wilson JM, Villareal RP, Hariharan R, et al. Magnetic resonance imaging of myocardial fibrosis in hypertrophic cardiomyopathy. Tex Heart Inst J. 2002;29(3):176–80.
145. Moon JC, McKenna WJ, McCrohon JA, et al. Toward clinical risk assessment in hypertrophic cardiomyopathy with gadolinium cardiovascular magnetic resonance. J Am Coll Cardiol. 2003;41(9):1561–7.
146. Teraoka K, Hirano M, Ookubo H, et al. Delayed contrast enhancement of MRI in hypertrophic cardiomyopathy. Magn Reson Imaging. 2004;22(2):155–61.
147. Kim RJ, Judd RM. Gadolinium-enhanced magnetic resonance imaging in hypertrophic cardiomyopathy: in vivo imaging of the pathologic substrate for premature cardiac death? J Am Coll Cardiol. 2003;41(9):1568–72.
148. Choudhury L, Mahrholdt H, Wagner A, et al. Myocardial scarring in asymptomatic or mildly symptomatic patients with hypertrophic cardiomyopathy. J Am Coll Cardiol. 2002;40(12): 2156–64.
149. O'Hanlon R, Grasso A, Roughton M, et al. Prognostic significance of myocardial fibrosis in hypertrophic cardiomyopathy. J Am Coll Cardiol. 2010;56(11):867–74.

150. Cannan CR, Reeder GS, Bailey KR, Melton 3rd LJ, Gersh BJ. Natural history of hypertrophic cardiomyopathy. A population-based study, 1976 through 1990. Circulation. 1995;92(9):2488–95.
151. Bruder O, Wagner A, Jensen CJ, et al. Myocardial scar visualized by cardiovascular magnetic resonance imaging predicts major adverse events in patients with hypertrophic cardiomyopathy. J Am Coll Cardiol. 2010;56(11):875–87.
152. Adabag AS, Maron BJ, Appelbaum E, et al. Occurrence and frequency of arrhythmias in hypertrophic cardiomyopathy in relation to delayed enhancement on cardiovascular magnetic resonance. J Am Coll Cardiol. 2008;51(14):1369–74.
153. Rubinshtein R, Glockner JF, Ommen SR, et al. Characteristics and clinical significance of late gadolinium enhancement by contrast-enhanced magnetic resonance imaging in patients with hypertrophic cardiomyopathy. Circ Heart Fail. 2010;3(1):51–8.
154. Todiere G, Aquaro GD, Piaggi P, et al. Progression of myocardial fibrosis assessed with cardiac magnetic resonance in hypertrophic cardiomyopathy. J Am Coll Cardiol. 2012;60(10):922–9.
155. ten Cate FJ, Soliman OI, Michels M, et al. Long-term outcome of alcohol septal ablation in patients with obstructive hypertrophic cardiomyopathy: a word of caution. Circ Heart Fail. 2010;3(3):362–9.
156. Sorajja P, Ommen SR, Holmes DR, et al. Survival after alcohol septal ablation for obstructive hypertrophic cardiomyopathy. Circulation. 2012;126(20):2374–80.
157. Sharma OP, Maheshwari A, Thaker K. Myocardial sarcoidosis. Chest. 1993;103(1):253–8.
158. Silverman KJ, Hutchins GM, Bulkley BH. Cardiac sarcoid: a clinicopathologic study of 84 unselected patients with systemic sarcoidosis. Circulation. 1978;58(6):1204–11.
159. Perry A, Vuitch F. Causes of death in patients with sarcoidosis. A morphologic study of 38 autopsies with clinicopathologic correlations. Arch Pathol Lab Med. 1995;119(2):167–72.
160. Gideon NM, Mannino DM. Sarcoidosis mortality in the United States 1979-1991: an analysis of multiple-cause mortality data. Am J Med. 1996;100(4):423–7.
161. Roberts WC, McAllister Jr HA, Ferrans VJ. Sarcoidosis of the heart. A clinicopathologic study of 35 necropsy patients (group 1) and review of 78 previously described necropsy patients (group 11). Am J Med. 1977;63(1):86–108.
162. Vignaux O. Cardiac sarcoidosis: spectrum of MRI features. AJR Am J Roentgenol. 2005;184(1):249–54.
163. Cheong BY, Muthupillai R, Nemeth M, et al. The utility of delayed-enhancement magnetic resonance imaging for identifying nonischemic myocardial fibrosis in asymptomatic patients with biopsy-proven systemic sarcoidosis. Sarcoidosis Vasc Diffuse Lung Dis. 2009;26(1):39–46.
164. Ohira H, Tsujino I, Ishimaru S, et al. Myocardial imaging with 18F-fluoro-2-deoxyglucose positron emission tomography and magnetic resonance imaging in sarcoidosis. Eur J Nucl Med Mol Imaging. 2008;35(5):933–41.
165. Smedema JP, Snoep G, van Kroonenburgh MP, et al. Evaluation of the accuracy of gadolinium-enhanced cardiovascular magnetic resonance in the diagnosis of cardiac sarcoidosis. J Am Coll Cardiol. 2005;45(10):1683–90.
166. Tadamura E, Yamamuro M, Kubo S, et al. Effectiveness of delayed enhanced MRI for identification of cardiac sarcoidosis: comparison with radionuclide imaging. AJR Am J Roentgenol. 2005;185(1):110–5.
167. Patel MR, Cawley PJ, Heitner JF, et al. Detection of myocardial damage in patients with sarcoidosis. Circulation. 2009;120(20):1969–77.
168. Jenni R, Oechslin E, Schneider J, Attenhofer Jost C, Kaufmann PA. Echocardiographic and pathoanatomical characteristics of isolated left ventricular non-compaction: a step towards classification as a distinct cardiomyopathy. Heart. 2001;86(6):666–71.
169. Paterick TE, Umland MM, Jan MF, et al. Left ventricular noncompaction: a 25-year odyssey. J Am Soc Echocardiogr. 2012;25(4):363–75.
170. Freedom RM, Yoo SJ, Perrin D, et al. The morphological spectrum of ventricular noncompaction. Cardiol Young. 2005;15(4):345–64.
171. Sedmera D, Pexieder T, Vuillemin M, Thompson RP, Anderson RH. Developmental patterning of the myocardium. Anat Rec. 2000;258(4):319–37.
172. Stollberger C, Finsterer J. Left ventricular hypertrabeculation/noncompaction. J Am Soc Echocardiogr. 2004;17(1):91–100.
173. Maron BJ, Towbin JA, Thiene G, et al. Contemporary definitions and classification of the cardiomyopathies: an American Heart Association Scientific Statement from the Council on Clinical Cardiology, Heart Failure and Transplantation Committee; Quality of Care and Outcomes Research and Functional Genomics and Translational Biology Interdisciplinary Working Groups; and Council on Epidemiology and Prevention. Circulation. 2006;113(14):1807–16.
174. Stahli BE, Gebhard C, Biaggi P, et al. Left ventricular non-compaction: prevalence in congenital heart disease. Int J Cardiol. 2013;167:2477–81.
175. Petersen SE, Selvanayagam JB, Wiesmann F, et al. Left ventricular non-compaction: insights from cardiovascular magnetic resonance imaging. J Am Coll Cardiol. 2005;46(1):101–5.
176. Jacquier A, Thuny F, Jop B, et al. Measurement of trabeculated left ventricular mass using cardiac magnetic resonance imaging in the diagnosis of left ventricular non-compaction. Eur Heart J. 2010;31(9):1098–104.
177. Grothoff M, Pachowsky M, Hoffmann J, et al. Value of cardiovascular MR in diagnosing left ventricular non-compaction cardiomyopathy and in discriminating between other cardiomyopathies. Eur Radiol. 2012;22(12):2699–709.
178. Chin TK, Perloff JK, Williams RG, Jue K, Mohrmann R. Isolated noncompaction of left ventricular myocardium. A study of eight cases. Circulation. 1990;82(2):507–13.
179. Frischknecht BS, Attenhofer Jost CH, Oechslin EN, et al. Validation of noncompaction criteria in dilated cardiomyopathy, and valvular and hypertensive heart disease. J Am Soc Echocardiogr. 2005;18(8):865–72.
180. Stollberger C, Finsterer J, Blazek G. Left ventricular hypertrabeculation/noncompaction and association with additional cardiac abnormalities and neuromuscular disorders. Am J Cardiol. 2002;90(8):899–902.
181. Oechslin EN, Attenhofer Jost CH, Rojas JR, Kaufmann PA, Jenni R. Long-term follow-up of 34 adults with isolated left ventricular noncompaction: a distinct cardiomyopathy with poor prognosis. J Am Coll Cardiol. 2000;36(2):493–500.
182. Alhabshan F, Smallhorn JF, Golding F, et al. Extent of myocardial non-compaction: comparison between MRI and echocardiographic evaluation. Pediatr Radiol. 2005;35(11):1147–51.
183. Dawson DK, Maceira AM, Raj VJ, et al. Regional thicknesses and thickening of compacted and trabeculated myocardial layers of the normal left ventricle studied by cardiovascular magnetic resonance. Circ Cardiovasc Imaging. 2011;4(2):139–46.
184. Pujadas S, Bordes R, Bayes-Genis A. Ventricular non-compaction cardiomyopathy: CMR and pathology findings. Heart. 2005;91(5):582.
185. Alsaileek AA, Syed I, Seward JB, Julsrud P. Myocardial fibrosis of left ventricle: magnetic resonance imaging in noncompaction. J Magn Reson Imaging. 2008;27(3):621–4.
186. Ivan D, Flamm SD, Abrams J, et al. Isolated ventricular non-compaction in adults with idiopathic cardiomyopathy: cardiac magnetic resonance and pathologic characterization of the anomaly. J Heart Lung Transplant. 2005;24(6):781–6.
187. Dodd JD, Holmvang G, Hoffmann U, et al. Quantification of left ventricular noncompaction and trabecular delayed hyperenhance-

ment with cardiac MRI: correlation with clinical severity. AJR Am J Roentgenol. 2007;189(4):974–80.
188. Dursun M, Agayev A, Nisli K, et al. MR imaging features of ventricular noncompaction: emphasis on distribution and pattern of fibrosis. Eur J Radiol. 2010;74(1):147–51.
189. Nucifora G, Aquaro GD, Pingitore A, Masci PG, Lombardi M. Myocardial fibrosis in isolated left ventricular non-compaction and its relation to disease severity. Eur J Heart Fail. 2011;13(2):170–6.
190. Chaowu Y, Li L, Shihua Z. Histopathological features of delayed enhancement cardiovascular magnetic resonance in isolated left ventricular noncompaction. J Am Coll Cardiol. 2011;58(3):311–2.
191. Jenni R, Wyss CA, Oechslin EN, Kaufmann PA. Isolated ventricular noncompaction is associated with coronary microcirculatory dysfunction. J Am Coll Cardiol. 2002;39(3):450–4.
192. Junga G, Kneifel S, Von Smekal A, Steinert H, Bauersfeld U. Myocardial ischaemia in children with isolated ventricular non-compaction. Eur Heart J. 1999;20(12):910–6.
193. Kohli SK, Pantazis AA, Shah JS, et al. Diagnosis of left-ventricular non-compaction in patients with left-ventricular systolic dysfunction: time for a reappraisal of diagnostic criteria? Eur Heart J. 2008;29(1):89–95.
194. Kawel N, Nacif M, Arai AE, et al. Trabeculated (noncompacted) and compact myocardium in adults: the multi-ethnic study of atherosclerosis. Circ Cardiovasc Imaging. 2012;5(3):357–66.
195. Falk RH. Diagnosis and management of the cardiac amyloidoses. Circulation. 2005;112(13):2047–60.
196. Rahman JE, Helou EF, Gelzer-Bell R, et al. Noninvasive diagnosis of biopsy-proven cardiac amyloidosis. J Am Coll Cardiol. 2004;43(3):410–5.
197. Fattori R, Rocchi G, Celletti F, et al. Contribution of magnetic resonance imaging in the differential diagnosis of cardiac amyloidosis and symmetric hypertrophic cardiomyopathy. Am Heart J. 1998;136(5):824–30.
198. Syed IS, Glockner JF, Feng D, et al. Role of cardiac magnetic resonance imaging in the detection of cardiac amyloidosis. JACC Cardiovasc Imaging. 2010;3(2):155–64.
199. Vogelsberg H, Mahrholdt H, Deluigi CC, et al. Cardiovascular magnetic resonance in clinically suspected cardiac amyloidosis: noninvasive imaging compared to endomyocardial biopsy. J Am Coll Cardiol. 2008;51(10):1022–30.
200. Krombach GA, Hahn C, Tomars M, et al. Cardiac amyloidosis: MR imaging findings and T1 quantification, comparison with control subjects. J Magn Reson Imaging. 2007;25(6):1283–7.
201. Van den Driesen RI, Slaughter RE, Strugnell WE. MR findings in cardiac amyloidosis. AJR Am J Roentgenol. 2006; 186(6):1682–5.
202. Kieninger B, Eriksson M, Kandolf R, et al. Amyloid in endomyocardial biopsies. Virchows Arch. 2010;456(5):523–32.
203. Austin BA, Tang WH, Rodriguez ER, et al. Delayed hyperenhancement magnetic resonance imaging provides incremental diagnostic and prognostic utility in suspected cardiac amyloidosis. JACC Cardiovasc Imaging. 2009;2(12):1369–77.
204. Mongeon FP, Jerosch-Herold M, Coelho-Filho OR, et al. Quantification of extracellular matrix expansion by CMR in infiltrative heart disease. JACC Cardiovasc Imaging. 2012;5(9):897–907.
205. Hosch W, Bock M, Libicher M, et al. MR-relaxometry of myocardial tissue: significant elevation of T1 and T2 relaxation times in cardiac amyloidosis. Invest Radiol. 2007;42(9):636–42.
206. Ruberg FL, Appelbaum E, Davidoff R, et al. Diagnostic and prognostic utility of cardiovascular magnetic resonance imaging in light-chain cardiac amyloidosis. Am J Cardiol. 2009;103(4):544–9.
207. Migrino RQ, Christenson R, Szabo A, et al. Prognostic implication of late gadolinium enhancement on cardiac MRI in light chain (AL) amyloidosis on long term follow up. BMC Med Phys. 2009;9:5.
208. Maceira AM, Prasad SK, Hawkins PN, Roughton M, Pennell DJ. Cardiovascular magnetic resonance and prognosis in cardiac amyloidosis. J Cardiovasc Magn Reson. 2008;10:54.
209. Hurst RT, Prasad A, Askew 3rd JW, Sengupta PP, Tajik AJ. Takotsubo cardiomyopathy: a unique cardiomyopathy with variable ventricular morphology. JACC Cardiovasc Imaging. 2010;3(6):641–9.
210. Koulouris S, Pastromas S, Sakellariou D, et al. Takotsubo cardiomyopathy: the "broken heart" syndrome. Hellenic J Cardiol. 2010;51(5):451–7.
211. Milinis K, Fisher M. Takotsubo cardiomyopathy: pathophysiology and treatment. Postgrad Med J. 2012;88(1043):530–8.
212. Kawai S, Suzuki H, Yamaguchi H, et al. Ampulla cardiomyopathy ('Takotusbo' cardiomyopathy)—reversible left ventricular dysfunction: with ST segment elevation. Jpn Circ J. 2000;64(2):156–9.
213. Singh NK, Rumman S, Mikell FL, Nallamothu N, Rangaswamy C. Stress cardiomyopathy: clinical and ventriculographic characteristics in 107 North American subjects. Int J Cardiol. 2010;141(3):297–303.
214. Haghi D, Athanasiadis A, Papavassiliu T, et al. Right ventricular involvement in Takotsubo cardiomyopathy. Eur Heart J. 2006;27(20):2433–9.
215. Korlakunta H, Butkevich A, Muthupillai R, Cheong BY. Biventricular takotsubo cardiomyopathy: cardiac magnetic resonance imaging as useful diagnostic tool. Tex Heart Inst J. 2011;38(1):88–9.
216. Elesber AA, Prasad A, Bybee KA, et al. Transient cardiac apical ballooning syndrome: prevalence and clinical implications of right ventricular involvement. J Am Coll Cardiol. 2006;47(5):1082–3.
217. Eitel I, von Knobelsdorff-Brenkenhoff F, Bernhardt P, et al. Clinical characteristics and cardiovascular magnetic resonance findings in stress (takotsubo) cardiomyopathy. JAMA. 2011;306(3):277–86.
218. Fernandez-Perez GC, Aguilar-Arjona JA, de la Fuente GT, et al. Takotsubo cardiomyopathy: assessment with cardiac MRI. AJR Am J Roentgenol. 2010;195(2):W139–45.
219. Otsuka Y, Noguchi T, Goto Y, Nonogi H, Yamada N. Hyperintensity on T2-weighted magnetic resonance imaging in Takotsubo cardiomyopathy. Int J Cardiol. 2008;130(1):113–6.
220. Neil C, Nguyen TH, Kucia A, et al. Slowly resolving global myocardial inflammation/oedema in Tako-Tsubo cardiomyopathy: evidence from T2-weighted cardiac MRI. Heart. 2012; 98(17):1278–84.
221. Abdel-Aty H, Cocker M, Friedrich MG. Myocardial edema is a feature of Tako-Tsubo cardiomyopathy and is related to the severity of systolic dysfunction: insights from T2-weighted cardiovascular magnetic resonance. Int J Cardiol. 2009;132(2):291–3.
222. Rolf A, Nef HM, Mollmann H, et al. Immunohistological basis of the late gadolinium enhancement phenomenon in tako-tsubo cardiomyopathy. Eur Heart J. 2009;30(13):1635–42.
223. Sharkey SW, Lesser JR, Zenovich AG, et al. Acute and reversible cardiomyopathy provoked by stress in women from the United States. Circulation. 2005;111(4):472–9.
224. Mitchell JH, Hadden TB, Wilson JM, et al. Clinical features and usefulness of cardiac magnetic resonance imaging in assessing myocardial viability and prognosis in Takotsubo cardiomyopathy (transient left ventricular apical ballooning syndrome). Am J Cardiol. 2007;100(2):296–301.
225. Nef HM, Mollmann H, Kostin S, et al. Tako-Tsubo cardiomyopathy: intraindividual structural analysis in the acute phase and after functional recovery. Eur Heart J. 2007;28(20):2456–64.
226. Rassi Jr A, Rassi A, Rassi SG. Predictors of mortality in chronic Chagas disease: a systematic review of observational studies. Circulation. 2007;115(9):1101–8.
227. Biolo A, Ribeiro AL, Clausell N. Chagas cardiomyopathy—where do we stand after a hundred years? Prog Cardiovasc Dis. 2010;52(4):300–16.

228. Nunes MC, Barbosa MM, Ribeiro AL, Colosimo EA, Rocha MO. Left atrial volume provides independent prognostic value in patients with Chagas cardiomyopathy. J Am Soc Echocardiogr. 2009;22(1):82–8.
229. Rassi Jr A, Rassi A, Little WC, et al. Development and validation of a risk score for predicting death in Chagas' heart disease. N Engl J Med. 2006;355(8):799–808.
230. Regueiro A, Garcia-Alvarez A, Sitges M, et al. Myocardial involvement in Chagas disease: insights from cardiac magnetic resonance. Int J Cardiol. 2013;165:107–12.
231. Rochitte CE, Oliveira PF, Andrade JM, et al. Myocardial delayed enhancement by magnetic resonance imaging in patients with Chagas' disease: a marker of disease severity. J Am Coll Cardiol. 2005;46(8):1553–8.
232. de Mello RP, Szarf G, Schvartzman PR, et al. Delayed enhancement cardiac magnetic resonance imaging can identify the risk for ventricular tachycardia in chronic Chagas' heart disease. Arq Bras Cardiol. 2012;98(5):421–30.
233. Rochitte CE, Nacif MS, de Oliveira Junior AC, et al. Cardiac magnetic resonance in Chagas' disease. Artif Organs. 2007;31(4):259–67.
234. Hoffmann B. Fabry disease: recent advances in pathology, diagnosis, treatment and monitoring. Orphanet J Rare Dis. 2009;4:21.
235. Nagueh SF. Fabry disease. Heart. 2003;89(8):819–20.
236. De Cobelli F, Esposito A, Belloni E, et al. Delayed-enhanced cardiac MRI for differentiation of Fabry's disease from symmetric hypertrophic cardiomyopathy. AJR Am J Roentgenol. 2009;192(3):W97–102.
237. Moon JC, Sachdev B, Elkington AG, et al. Gadolinium enhanced cardiovascular magnetic resonance in Anderson-Fabry disease. Evidence for a disease specific abnormality of the myocardial interstitium. Eur Heart J. 2003;24(23):2151–5.
238. Imbriaco M, Spinelli L, Cuocolo A, et al. MRI characterization of myocardial tissue in patients with Fabry's disease. AJR Am J Roentgenol. 2007;188(3):850–3.
239. Imbriaco M, Pisani A, Spinelli L, et al. Effects of enzyme-replacement therapy in patients with Anderson-Fabry disease: a prospective long-term cardiac magnetic resonance imaging study. Heart. 2009;95(13):1103–7.
240. Messalli G, Imbriaco M, Avitabile G, et al. Role of cardiac MRI in evaluating patients with Anderson-Fabry disease: assessing cardiac effects of long-term enzyme replacement therapy. Radiol Med. 2012;117(1):19–28.
241. Liu P, Olivieri N. Iron overload cardiomyopathies: new insights into an old disease. Cardiovasc Drugs Ther. 1994;8(1):101–10.
242. Qaseem A, Aronson M, Fitterman N, et al. Screening for hereditary hemochromatosis: a clinical practice guideline from the American College of Physicians. Ann Intern Med. 2005;143(7):517–21.
243. Tanner MA, Galanello R, Dessi C, et al. Combined chelation therapy in thalassemia major for the treatment of severe myocardial siderosis with left ventricular dysfunction. J Cardiovasc Magn Reson. 2008;10:12.
244. Wood JC. History and current impact of cardiac magnetic resonance imaging on the management of iron overload. Circulation. 2009;120(20):1937–9.
245. Kremastinos DT, Farmakis D. Iron overload cardiomyopathy in clinical practice. Circulation. 2011;124(20):2253–63.
246. Gujja P, Rosing DR, Tripodi DJ, Shizukuda Y. Iron overload cardiomyopathy: better understanding of an increasing disorder. J Am Coll Cardiol. 2010;56(13):1001–12.
247. Modell B, Khan M, Darlison M, et al. Improved survival of thalassaemia major in the UK and relation to T2* cardiovascular magnetic resonance. J Cardiovasc Magn Reson. 2008;10:42.
248. Wood JC, Otto-Duessel M, Aguilar M, et al. Cardiac iron determines cardiac T2*, T2, and T1 in the gerbil model of iron cardiomyopathy. Circulation. 2005;112(4):535–43.
249. Kirk P, Roughton M, Porter JB, et al. Cardiac T2* magnetic resonance for prediction of cardiac complications in thalassemia major. Circulation. 2009;120(20):1961–8.
250. Roger VL, Go AS, Lloyd-Jones DM, et al. Heart disease and stroke statistics–2012 update: a report from the American Heart Association. Circulation. 2012;125(1):e2–220.
251. Bashore TM, Balter S, Barac A, et al. 2012 American College of Cardiology Foundation/Society for Cardiovascular Angiography and Interventions expert consensus document on cardiac catheterization laboratory standards update. A report of the American College of Cardiology Foundation Task Force on Expert Consensus documents. J Am Coll Cardiol. 2012;59(24):2221–305.
252. Patel MR, Peterson ED, Dai D, et al. Low diagnostic yield of elective coronary angiography. N Engl J Med. 2010; 362(10):886–95.
253. Mowatt G, Cook JA, Hillis GS, et al. 64-Slice computed tomography angiography in the diagnosis and assessment of coronary artery disease: systematic review and meta-analysis. Heart. 2008;94(11):1386–93.
254. Paulin S, von Schulthess GK, Fossel E, Krayenbuehl HP. MR imaging of the aortic root and proximal coronary arteries. AJR Am J Roentgenol. 1987;148(4):665–70.
255. Wielopolski PA, Manning WJ, Edelman RR. Single breath-hold volumetric imaging of the heart using magnetization-prepared 3-dimensional segmented echo planar imaging. J Magn Reson Imaging. 1995;5(4):403–9.
256. Bashore TM, Bates ER, Berger PB, et al. American College of Cardiology/Society for Cardiac Angiography and Interventions clinical expert consensus document on cardiac catheterization laboratory standards. A report of the American College of Cardiology Task Force on Clinical Expert Consensus Documents. J Am Coll Cardiol. 2001;37(8):2170–214.
257. Flamm SD, Muthupillai R. Coronary artery magnetic resonance angiography. J Magn Reson Imaging. 2004;19(6):686–709.
258. Huber ME, Kozerke S, Pruessmann KP, Smink J, Boesiger P. Sensitivity-encoded coronary MRA at 3T. Magn Reson Med. 2004;52(2):221–7.
259. Nagata M, Kato S, Kitagawa K, et al. Diagnostic accuracy of 1.5-T unenhanced whole-heart coronary MR angiography performed with 32-channel cardiac coils: initial single-center experience. Radiology. 2011;259(2):384–92.
260. Yang Q, Li K, Liu X, et al. 3.0T whole-heart coronary magnetic resonance angiography performed with 32-channel cardiac coils: a single-center experience. Circ Cardiovasc Imaging. 2012;5(5):573–9.
261. Wang Y, Vidan E, Bergman GW. Cardiac motion of coronary arteries: variability in the rest period and implications for coronary MR angiography. Radiology. 1999;213(3):751–8.
262. Wielopolski PA, van Geuns RJ, de Feyter PJ, Oudkerk M. Breath-hold coronary MR angiography with volume-targeted imaging. Radiology. 1998;209(1):209–19.
263. Ehman RL, Felmlee JP. Adaptive technique for high-definition MR imaging of moving structures. Radiology. 1989;173(1):255–63.
264. Wang Y, Riederer SJ, Ehman RL. Respiratory motion of the heart: kinematics and the implications for the spatial resolution in coronary imaging. Magn Reson Med. 1995;33(5):713–9.
265. Kato S, Kitagawa K, Ishida N, et al. Assessment of coronary artery disease using magnetic resonance coronary angiography: a national multicenter trial. J Am Coll Cardiol. 2010;56(12):983–91.
266. Weber OM, Martin AJ, Higgins CB. Whole-heart steady-state free precession coronary artery magnetic resonance angiography. Magn Reson Med. 2003;50(6):1223–8.
267. Sakuma H, Ichikawa Y, Chino S, et al. Detection of coronary artery stenosis with whole-heart coronary magnetic resonance angiography. J Am Coll Cardiol. 2006;48(10):1946–50.
268. Yang Q, Li K, Liu X, et al. Contrast-enhanced whole-heart coronary magnetic resonance angiography at 3.0-T: a compara-

tive study with X-ray angiography in a single center. J Am Coll Cardiol. 2009;54(1):69–76.
269. Wieben O, Francois C, Reeder SB. Cardiac MRI of ischemic heart disease at 3T: potential and challenges. Eur J Radiol. 2008;65(1):15–28.
270. Brittain JH, Hu BS, Wright GA, et al. Coronary angiography with magnetization-prepared T2 contrast. Magn Reson Med. 1995;33(5):689–96.
271. Kim WY, Danias PG, Stuber M, et al. Coronary magnetic resonance angiography for the detection of coronary stenoses. N Engl J Med. 2001;345(26):1863–9.
272. Nagel E. Magnetic resonance coronary angiography: the condemned live longer. J Am Coll Cardiol. 2010;56(12): 992–4.
273. Arbab-Zadeh A, Miller JM, Rochitte CE, et al. Diagnostic accuracy of computed tomography coronary angiography according to pre-test probability of coronary artery disease and severity of coronary arterial calcification. The CORE-64 (Coronary Artery Evaluation Using 64-Row Multidetector Computed Tomography Angiography) International Multicenter Study. J Am Coll Cardiol. 2012;59(4):379–87.
274. Miller JM, Rochitte CE, Dewey M, et al. Diagnostic performance of coronary angiography by 64-row CT. N Engl J Med. 2008;359(22):2324–36.
275. Taylor AJ, Cerqueira M, Hodgson JM, et al. ACCF/SCCT/ACR/AHA/ASE/ASNC/NASCI/SCAI/SCMR 2010 appropriate use criteria for cardiac computed tomography. A report of the American College of Cardiology Foundation Appropriate Use Criteria Task Force, the Society of Cardiovascular Computed Tomography, the American College of Radiology, the American Heart Association, the American Society of Echocardiography, the American Society of Nuclear Cardiology, the North American Society for Cardiovascular Imaging, the Society for Cardiovascular Angiography and Interventions, and the Society for Cardiovascular Magnetic Resonance. J Am Coll Cardiol. 2010;56(22):1864–94.
276. Liu X, Zhao X, Huang J, et al. Comparison of 3D free-breathing coronary MR angiography and 64-MDCT angiography for detection of coronary stenosis in patients with high calcium scores. AJR Am J Roentgenol. 2007;189(6):1326–32.
277. Bluemke DA, Achenbach S, Budoff M, et al. Noninvasive coronary artery imaging: magnetic resonance angiography and multidetector computed tomography angiography: a scientific statement from the American Heart Association Committee on Cardiovascular Imaging and Intervention of the Council on Cardiovascular Radiology and Intervention, and the Councils on Clinical Cardiology and Cardiovascular Disease in the Young. Circulation. 2008;118(5):586–606.
278. Newburger JW, Takahashi M, Gerber MA, et al. Diagnosis, treatment, and long-term management of Kawasaki disease: a statement for health professionals from the Committee on Rheumatic Fever, Endocarditis, and Kawasaki Disease, Council on Cardiovascular Disease in the Young. Pediatrics. 2004;114(6):1708–33.
279. Shulman ST, Rowley AH. Advances in Kawasaki disease. Eur J Pediatr. 2004;163(6):285–91.
280. Greil GF, Stuber M, Botnar RM, et al. Coronary magnetic resonance angiography in adolescents and young adults with kawasaki disease. Circulation. 2002;105(8):908–11.
281. Angelini P, Monge J. Newer concepts regarding adults with coronary artery aneurysms: are they all Kawasaki? Does it make a difference? Circulation. 2012;125(25):3076–8.
282. Yamanaka O, Hobbs RE. Coronary artery anomalies in 126,595 patients undergoing coronary arteriography. Cathet Cardiovasc Diagn. 1990;21(1):28–40.
283. Angelini P, Shah NR, Uribe CE, et al. Novel MRI-based screening protocol to identify adolescents at high risk of sudden cardiac death (abstract). J Am Coll Cardiol. 2013;61(10S):E1621.
284. Machado C, Bhasin S, Soulen RL. Confirmation of anomalous origin of the right coronary artery from the left sinus of Valsalva with magnetic resonance imaging. Chest. 1993;104(4):1284–6.
285. McConnell MV, Ganz P, Selwyn AP, et al. Identification of anomalous coronary arteries and their anatomic course by magnetic resonance coronary angiography. Circulation. 1995;92(11): 3158–62.
286. Post JC, van Rossum AC, Bronzwaer JG, et al. Magnetic resonance angiography of anomalous coronary arteries. A new gold standard for delineating the proximal course? Circulation. 1995;92(11):3163–71.
287. Angelini P. Coronary artery anomalies: an entity in search of an identity. Circulation. 2007;115(10):1296–305.
288. Angelini P, Villason S, Chan AV, Diez JG. Normal and anomalous coronary arteries in humans. In: Angelini P, editor. Coronary artery anomalies. Philadelphia: Lippincott Williams & Wilkins; 1999. p. 27–150.
289. Angelini P, Flamm SD. Newer concepts for imaging anomalous aortic origin of the coronary arteries in adults. Catheter Cardiovasc Interv. 2007;69(7):942–54.
290. Angelini P, Monge J. Coronary artery anomalies. In: Morsucci M, editor. Grossman's cardiac catheterization, angiography, and intervention. 8th ed. Riverwoods: Lippincott Williams & Wilkins; 2013.
291. Angelini P, Monge JU, Forstall P, et al. Anomalous right coronary artery from the left sinus of Valsalva: pathophysiological mechanisms studied by intravascular ultrasound, clinical presentations and response to stent angioplasty (abstract). J Am Coll Cardiol. 2013;61:E18.
292. Angelini P, Cheong B. Left coronary artery from the right coronary sinus: what can CT angiography tell us? J Cardiovasc Comput Tomogr. 2010;4(4):255–7.
293. Mohlenkamp S, Hort W, Ge J, Erbel R. Update on myocardial bridging. Circulation. 2002;106(20):2616–22.
294. Prati F, Regar E, Mintz GS, et al. Expert review document on methodology, terminology, and clinical applications of optical coherence tomography: physical principles, methodology of image acquisition, and clinical application for assessment of coronary arteries and atherosclerosis. Eur Heart J. 2010;31(4): 401–15.
295. Tearney GJ, Regar E, Akasaka T, et al. Consensus standards for acquisition, measurement, and reporting of intravascular optical coherence tomography studies: a report from the International Working Group for Intravascular Optical Coherence Tomography Standardization and Validation. J Am Coll Cardiol. 2012;59(12):1058–72.
296. Cowles RA, Berdon WE. Bland-White-Garland syndrome of anomalous left coronary artery arising from the pulmonary artery (ALCAPA): a historical review. Pediatr Radiol. 2007;37(9):890–5.
297. Douard H, Barat JL, Laurent F, et al. Magnetic resonance imaging of an anomalous origin of the left coronary artery from the pulmonary artery. Eur Heart J. 1988;9(12):1356–60.
298. Komocsi A, Simor T, Toth L, et al. Magnetic resonance studies in management of adult cases with Bland-White-Garland syndrome. Int J Cardiol. 2007;123(1):e8–11.
299. Molinari G, Balbi M, Bertero G, et al. Magnetic resonance imaging in Bland-White-Garland syndrome. Am Heart J. 1995;129(5):1040–2.
300. Pena E, Nguyen ET, Merchant N, Dennie G. ALCAPA syndrome: not just a pediatric disease. Radiographics. 2009;29(2): 553–65.
301. Yau JM, Singh R, Halpern EJ, Fischman D. Anomalous origin of the left coronary artery from the pulmonary artery in adults: a comprehensive review of 151 adult cases and a new diagnosis in a 53-year-old woman. Clin Cardiol. 2011;34(4):204–10.
302. Lee DC, Johnson NP. Quantification of absolute myocardial blood flow by magnetic resonance perfusion imaging. JACC Cardiovasc Imaging. 2009;2:761–70.